

DAMAGE CHARACTERIZATION IN COMPOSITE LAMINATES WITH HOLES

A THESIS SUBMITTED TO
THE GRADUATE SCHOOL OF NATURAL AND APPLIED SCIENCES
OF
MIDDLE EAST TECHNICAL UNIVERSITY



BY

OZAN ERARTSIN

IN PARTIAL FULFILLMENT OF THE REQUIREMENTS
FOR
THE DEGREE OF MASTER OF SCIENCE
IN
MECHANICAL ENGINEERING

FEBRUARY 2016

Approval of the thesis:

DAMAGE CHARACTERIZATION IN COMPOSITE LAMINATES WITH HOLES

submitted by **OZAN ERARTSIN** in partial fulfillment of the requirements for the degree of **Master of Science in Mechanical Engineering Department, Middle East Technical University** by,

Prof. Dr. Gülbin Dural Ünver
Dean, Graduate School of **Natural and Applied Sciences**

Prof. Dr. Tuna Balkan
Head of Department, **Mechanical Engineering**

Prof. Dr. Kemal Levend Parnas
Supervisor, **Mechanical Engineering Dept., METU**

Examining Committee Members:

Prof. Dr. R. Orhan Yıldırım
Mechanical Engineering Dept., METU


Prof. Dr. Kemal Levend Parnas
Mechanical Engineering Dept., METU

Prof. Dr. Fevzi Suat Kadioğlu
Mechanical Engineering Dept., METU

Asst. Prof. Dr. Hüsnü Dal
Mechanical Engineering Dept., METU

Asst. Prof. Dr. Melis Hunt
Mechanical Engineering Dept., TED University

Date: 02.02.2016



I hereby declare that all information in this document has been obtained and presented in accordance with academic rules and ethical conduct. I also declare that, as required by these rules and conduct, I have fully cited and referenced all material and results that are not original to this work.

Name, Last name : Ozan Erartsın

Signature :

ABSTRACT

DAMAGE CHARACTERIZATION IN COMPOSITE LAMINATES WITH HOLES

Erartsm, Ozan

M.Sc., Department of Mechanical Engineering

Supervisor: Prof. Dr. Kemal Levend Parnas

February 2016, 122 pages

The main objective of this study is to conduct progressive failure analysis (PFA) of quasi-isotropic open-hole tension coupons that exhibit different failure patterns, namely brittle, pull-out, and delamination failure. Effect of delamination, in-situ strengths and degradation trend on failure patterns and loads are also investigated. Explicit finite element method is used for the study. Intra-laminar regions in the finite element model were modeled with 3-D continuum shell elements and inter-laminar regions were modeled with 3-D interface elements with bilinear traction-separation formulation of Cohesive Zone Method (CZM). Hashin's failure criterion is used along with linear gradual damage evolution for intra-laminar regions. Results are compared with the open-hole tension tests that are conducted and taken from the literature. The results show that the model developed here gives satisfactory results in modeling the damage progression in open-hole tension laminates where three different failure patterns are involved. It is also observed that the delamination plays an important role for the damage progression in open-hole tension laminates; thus, neglecting it may result in inaccurate prediction of damage patterns and overestimated ultimate loads.

Keywords: Open-hole Laminates, Delamination, Cohesive Zone Method, Progressive Failure

ÖZ

DELİKLİ KOMPOZİT LEVHALARDA HASAR KARAKTERİZASYONU

Erartsm, Ozan

Yüksek Lisans, Makina Mühendisliği Bölümü

Tez Yöneticisi: Prof. Dr. Kemal Levend Parnas

Şubat 2016, 122 sayfa

Bu çalışmanın amacı, gevrek, sıyrılma, ve delaminasyon hasarına maruz kalan yarı-izotropik delikli kompozit levhaların kademeli hasar analizini gerçekleştirmektir. Çalışmada delaminasyonun, yerinde (in-situ) dayanımların ve hasar ilerlemesi şeklinin hasar ilerlemesine, son hasar durumuna ve levhanın taşıdığı nihai yüke etkisi de incelenmiştir. Çalışmada eksplisit sonlu eleman analizi yöntemi kullanılmıştır. Tabaka içi bölgeler üç boyutlu sürekli ortam elemanları, tabaka arası bölgeler ise kohesiv elemanlar (yapışkan ara elemanlar) ile modellenmiştir. Tabaka içi bölgeler için Hashin hasar başlangıcı kriteri ve doğrusal kademeli hasar ilerlemesi modeli kullanılmıştır. Sonlu eleman analizinin sonuçları, yürütülen ve literatürden bulunan delikli levha çekme deneylerinin sonuçları ile karşılaştırılmıştır. Karşılaştırma sonucunda geliştirilen sonlu eleman analizi modelinin bahsedilen farklı hasar çeşitlerini başarı ile simüle ettiği gözlenmiştir. Delaminasyon ihmal edildiğinde levhanın maruz kaldığı hasar tipinin yanlış tahmin edilebildiği ve nihai yükte artış olabildiği gözlenmiştir.

Anahtar Kelimeler: Delikli Kompozit Levhalar, Delaminasyon, Yapışkan Ara Eleman Yöntemi, Kademeli Hasar



For a better world

ACKNOWLEDGEMENTS

First of all, I would like to express my gratitude to my advisor Prof. Dr. Levend Parnas for his contributions throughout my undergraduate and graduate studies. It is my advisor who made me interested in composites in my undergraduate education, encouraging me to study composites in my graduate education.

I am grateful to my colleague Bilal Atar for sharing his experimental work with me. I benefited a lot from the experiment reports he wrote for the material characterization tests.

I am also grateful to Servet Şehirli, Hasan Devrez, and Önder Şahin for their help with the experimental part of the study.

The last but not the least, I would like to express my sincere thanks to my dear friends and colleagues. Serhat Bilyaz has been so generous to share his experience and knowledge about thesis writing and has supported me continuously. My roommate Erdem Dursunkaya has always listened to me patiently when I needed help and guided me in the critical decisions I needed to make. I offer my special thanks also to Gizem Şencan, Eylül Şimşek, Berke Harmancı, Serdar Hiçdurmaz, Onur Özkan and Mine Kaya for their invaluable support, encouragement and companionship.

TABLE OF CONTENTS

ABSTRACT	v
ÖZ	vi
ACKNOWLEDGEMENTS	viii
TABLE OF CONTENTS	ix
LIST OF TABLES	xii
LIST OF FIGURES	xiii
NOMENCLATURE	xvii
CHAPTERS	1
1- INTRODUCTION	1
1.1. Composite Laminates with Holes	1
1.2. Damage in Laminated Composites	3
1.3. Damage in Laminated Composites with Holes	6
1.4. Damage Characterization	7
1.4.1. Intra-ply Damage	8
1.4.2. Inter-ply Damage	9
1.5. Motivation	13
1.6. Scope of Thesis	13
1.7. Outline	13
2- LITERATURE SURVEY	15
2.1. Intralaminar Failure Criteria	15
2.2. Tests and Analyses	23
2.3. Conclusions from the Literature Survey	31
3- THEORY	33

3.1.	Failure in Composites	33
3.2.	Cohesive Zone Model	39
4-	BENCHMARK TESTS	51
4.1.	Introduction	51
4.2.	Benchmark Coupons	51
4.2.1.	Coupon Exhibiting Brittle Failure	53
4.2.2.	Coupon Exhibiting Delamination Failure	54
4.2.3.	Coupon Exhibiting Pull-out Failure	56
5-	FINITE ELEMENT ANALYSIS	59
5.1.	Finite Element Method	59
5.2.	Description of the Model	61
5.2.1.	Elements used in analyses	68
5.2.2.	Material Properties	70
5.2.3.	Cohesive Layer Parameters	73
5.2.4.	In-plane parameters	76
5.2.5.	Additional Measures	81
6-	RESULTS	83
6.1.	Laminate 1 (Laminate Exhibiting Brittle Failure)	84
6.1.1.	Analysis with Cohesive Layers	84
6.1.2.	Analysis without Cohesive Layers	88
6.2.	Laminate 2 (Laminate Exhibiting Delamination Failure)	89
6.2.1.	Analysis with Cohesive Layers	89
6.2.2.	Analysis without Cohesive Layers	95
6.3.	Laminate 3 (Laminate Exhibiting Pull-out Failure)	96
6.3.1.	Analysis with Cohesive Layers	96
6.3.2.	Analysis without Cohesive Layers	105

SUMMARY, DISCUSSION AND FUTURE WORK	107
7.1. Summary	107
7.2. Discussion	108
7.3. Future Work	110
REFERENCES	113
APPENDIX: EFFECT OF MESH SIZE ON THE ULTIMATE LOAD	119



LIST OF TABLES

TABLES

Table 4-1 Benchmark coupons where the coupons exhibiting brittle and delamination failure are taken from [12] and the laminate exhibiting pull-out failure is tested in scope of the thesis	53
Table 5-1 Lamina level coupon tests and properties measured	70
Table 5-2 Material properties [13,63,64].....	71
Table 5-3 In-situ strengths	73
Table 5-4 Cohesive layer parameters	75
Table 5-5 Experimental failure energies.....	76
Table 5-6 Failure energies for instantaneous degradation.....	78
Table 6-1 Comparison of the ultimate loads for Laminate 1	88
Table 6-2 Comparison of the ultimate loads for Laminate 2	94
Table 6-3 Cases for FEA of Laminate 3 with in-situ strengths	96
Table 6-4 Comparison of the ultimate loads for Laminate 3	104

LIST OF FIGURES

FIGURES

Figure 1-1 Filled-hole tension laminates after failure [7]	2
Figure 1-2 Open-hole tension laminate after failure	3
Figure 1-3 Inter-ply and intra-ply regions in a sub-laminate with lay-up $[-45/0/45/90]$	4
Figure 1-4 Laminate with extensive delamination failure [12]	5
Figure 1-5 Laminate with fiber and matrix failure in tension.....	5
Figure 1-6 Damage characterization in laminated composites	7
Figure 1-7 Stress vs strain graph in composite laminae for different degradation models where σ_{ijr} denotes residual stress at the lamina after damage [19]	9
Figure 1-8 Crack propagation modes: Mode I, Mode II and Mode III from left to right [21]	9
Figure 1-9 Crack closure method with closed and extended crack configurations [24].....	11
Figure 1-10 Cohesive layer comprised of interface elements in DCB test modeling [27].....	12
Figure 2-1 Comparison of failure envelopes predicted by experimental data for glass/epoxy lamina subjected to in-plane shear and transverse normal stresses [28]	19
Figure 2-2 Comparison of failure envelopes predicted by experimental data for glass/epoxy lamina subjected to biaxial normal stresses in directions parallel (σ_x) and perpendicular (σ_y) to the fibers [28].	20
Figure 2-3 Comparison between the predicted and measured final failure stresses for $[0^\circ/\pm 45^\circ/90^\circ]$ carbon/epoxy laminates subjected to biaxial loads [28].....	20
Figure 2-4 Failure envelopes and WWFE test data for unidirectional composite E-Glass/LY556 under combined transverse normal and in-plane shear stresses [40]	22
Figure 2-5 Compressive strength as a function of ply orientation for AS4-3502 $[\pm\theta]_s$ laminates (α stands for angle of fracture plane) [40]	23

Figure 2-6 Three different failure mechanisms observed depending on scaling regime and specimen dimensions [12]	24
Figure 2-7 Effect of thickness on open hole tensile strengths [41]	25
Figure 2-8 Location of potential strip lines (lines with different orientation angles belong to different plies) [8]	25
Figure 2-9 Crack path in [45/90/-45/0] _{4S} laminate [42]	27
Figure 2-10 Zigzag approximation of the linear softening law (a) and corresponding stiffness degradation (b).....	30
Figure 3-1 Unidirectional lamina [51]	33
Figure 3-2 Linear damage evolution (adapted from [51])	36
Figure 3-3 Change of damage variable with equivalent displacement [51]	37
Figure 3-4 Craze zone at the crack tip in polymers (Adapted from [52])	39
Figure 3-5 Fiber bridging in DCB test of a unidirectional composite laminate [54]	40
Figure 3-6 Micro crack coalescence in Mode-II delamination experiment [52] ...	40
Figure 3-7 Bilinear and linear-exponential traction-separation response in normal crack opening mode (Adapted from [51])	41
Figure 3-8 Development of numerical cohesive zone (L_{cz} denotes the length of cohesive zone) [27]	44
Figure 3-9 Curve fit to critical energy release rate vs. mode mixture data [59]	46
Figure 3-10 Critical energy release rate vs. mode mixture for S2 glass/epoxy	47
Figure 3-11 Mixed-mode response of cohesive elements [51]	48
Figure 4-1 Coupon geometry (Adapted from [61])	52
Figure 4-2 (a) Fracture surface of the laminate (b) Load-displacement curve of the laminate [13]	54
Figure 4-3 Load-displacement curve of the laminate exhibiting delamination failure	55
Figure 4-4 (top) X-ray image after the first load drop (bottom) picture of the free edge with dye penetrant applied after the first load drop (Adapted from [12])	56
Figure 4-5 Orientation of the light, specimen, and camera for open-hole tension test of the laminate exhibiting pull-out failure	57

Figure 4-6 Damage state at (a) 67% (b) 90% (c) 98% (d) 99.7% of the ultimate load.....	58
Figure 4-7 (left) Typical load-displacement curve (right) laminate after failure ...	58
Figure 5-1 Isometric view of the laminate 3	62
Figure 5-2 Mesh pattern around the hole	63
Figure 5-3 Boundary conditions at $x = 0$	63
Figure 5-4 Kinetic and strain energy change with time for laminate 3	64
Figure 5-5 Change of Poisson's ratio with fiber angle for a lamina made of IM7/8552.....	66
Figure 5-6 Change of extension-shear coupling coefficient with fiber angle for a lamina made of IM7/8552.....	66
Figure 5-7 Through-the-thickness discretization of the laminates (orange colored layers represent cohesive layers).....	67
Figure 5-8 8-node continuum shell element [51].....	69
Figure 5-9 Integration points in the thickness direction of the laminate without ply-blocking (cohesive layer is not shown)	69
Figure 5-10 Cohesive zone length (Adapted from [66]).....	74
Figure 5-11 Failure energies in fiber tension failure mode.....	77
Figure 5-12 Laminae loaded in longitudinal and transverse tension	79
Figure 5-13 Equivalent stress vs. equivalent strain for a S2 glass/epoxy lamina in transverse tension.....	79
Figure 5-14 Equivalent stress vs. equivalent strain for a S2 glass/epoxy lamina in longitudinal tension.....	80
Figure 5-15 Effect of hourglass control on matrix damage	82
Figure 6-1 Color code for damage evolution parameters	84
Figure 6-2 Load-displacement curve from FEA of laminate 1 with instantaneous degradation.....	85
Figure 6-3 Damage at laminate 1 after failure (gradual degradation).....	86
Figure 6-4 Load-displacement curve from FEA of laminate 1 with gradual degradation.....	87

Figure 6-5 Load-displacement curve from FEA of laminate 1 with and without cohesive layers (instantaneous degradation)	88
Figure 6-6 Load-displacement curve from FEA of the laminate 2 by FEA	89
Figure 6-7 (Top) Matrix tension damage at 90% ultimate load (Bottom) X-ray image at 80% ultimate load [12].....	91
Figure 6-8 Damage at point b ($F = 22.6 \text{ kN}, U = 0.41 \text{ mm}$)	92
Figure 6-9 Damage at point c ($F = 18.6 \text{ kN}, U = 0.44 \text{ mm}$).....	92
Figure 6-10 Damage at point d ($F = 21.5 \text{ kN}, U = 0.5 \text{ mm}$)	93
Figure 6-11 Longitudinal normal stress (σ_{11}) distribution in 0° plies at point e .	93
Figure 6-12 Damage at point e ($F = 19.0 \text{ kN}, U = 0.52 \text{ mm}$)	94
Figure 6-13 Load-displacement curve from FEA of laminate 2 with and without cohesive layers (in-situ model with gradual degradation)	95
Figure 6-14 Load-displacement curves obtained with different degradation trends for laminate 3	97
Figure 6-15 Load – displacement curve from FEA of laminate 3	98
Figure 6-16 Damage at point a ($F = 42.4 \text{ kN}, U = 2.2 \text{ mm}$).....	100
Figure 6-17 Damage at point b ($F = 48 \text{ kN}, U = 2.9 \text{ mm}$).....	102
Figure 6-18 Damage at point c ($F = 46 \text{ kN}, U = 3.52 \text{ mm}$).....	103
Figure 6-19 Load-displacement curve from FEA of laminate 3 with and without cohesive layers	105

NOMENCLATURE

Abbreviations

ASTM	American Society for Testing and Materials
BK	Benzeggah Kenane
CZM	Cohesive Zone Method
DCB	Double Cantilever Beam
ENF	End Notched Fracture
FEA	Finite Element Analysis
FEM	Finite Element Model
MMB	Mixed Mode Bending
OHC	Open-Hole Compression
OHT	Open-Hole Tension
PFA	Progressive Failure Analysis
VCCT	Virtual Crack Closure Technique
WWFE	World Wide Failure Exercise

Symbols (Greek)

α	Power Law exponent
α^*	Coefficient controlling the effect of shear on fiber tensile failure
δ_m	Mixed mode separation
δ_m^0	Mixed mode separation at damage initiation
δ_m^{max}	Maximum mixed mode separation during the loading history
δ_m^f	Mixed mode separation at total failure
δ_{eq}^0	Equivalent displacement at damage initiation

δ_{eq}^f	Equivalent displacement at point of complete damage
δ_n^0	Normal separation at damage initiation
δ_s^0	Separation in the first shear direction at damage initiation
δ_t^0	Separation in the second shear direction at damage initiation
δ_n^f	Normal separation at total failure
δ_s^f	Separation in the first shear direction at total failure
δ_t^f	Separation in the second shear direction at total failure
ε_{11}	Longitudinal normal strain in a lamina
ε_{22}	Transverse normal strain in a lamina
ε_{12}	In-plane shear strain in a lamina
η	BK Law exponent
η	Viscosity parameter of damage stabilization
η'	Internal friction parameter
θ	Fiber orientation angle of lamina with respect to loading axis
ν_{12}	Poisson's ratio of a lamina
σ_{eq}^0	Equivalent stress at damage initiation
σ_{11}	Longitudinal normal stress in a lamina
σ_x	Normal stress in lamina in loading direction
σ_{22}	Transverse normal stress in a lamina
σ_y	Normal stress in lamina in direction perpendicular to loading
τ_{12}	In-plane shear stress in principal coordinates
τ_{xy}	In-plane shear stress in loading coordinates

Symbols (Latin)

C	Undamaged stiffness matrix of material point
C_d	Damaged lamina stiffness matrix of material point
d	Hole diameter
d_f	Fiber damage variable
d_f^t	Fiber tension damage variable
d_f^c	Fiber compression damage variable
d_m	Matrix damage variable
d_m^t	Matrix tension damage variable
d_m^c	Matrix compression damage variable
d_s	Shear damage variable
E_{11}	Longitudinal Young's modulus of a lamina
E_{22}	Transverse Young's modulus of a lamina
E_x	Young's modulus in x direction
E_y	Young's modulus in y direction
G_{12}	Shear modulus of lamina
G_{Ic}	Critical mode-I strain energy release rate
G_{IIc}	Critical mode-II strain energy release rate
G_{IIIc}	Critical mode-III strain energy release rate
G_{fc}	Failure energy in longitudinal compression
G_{ft}	Failure energy in longitudinal tension
G_{mc}	Failure energy in transverse compression
G_{mt}	Failure energy in transverse tension
I	Internal forces at a node
K_n	Interface stiffness in normal direction

K_s	Interface stiffness in the first shear direction
K_t	Interface stiffness in the second shear direction
l	Laminate length
l_{cz}	Cohesive zone length
l_e	Element side length
L_c	Characteristic element length
M	Nodal mass matrix
m_x, m_y	Extension-shear coupling coefficients
P	Load applied
S^L	Longitudinal shear strength
S_L^{is}	In-situ longitudinal shear strength of a lamina
S^T	Transverse shear strength
t	Laminate thickness
t_n^0	Normal interface strength
t_s^0	Interface strength in the first shear direction
t_t^0	Interface strength in the second shear direction
u, \dot{u}, \ddot{u}	Nodal displacement, velocity, acceleration
U	Displacement
X^C	Tensile strength in transverse direction
X^T	Tensile strength in longitudinal direction
Y^C	Compressive strength in transverse direction
Y^T	Tensile strength in transverse direction
Y_T^{is}	In-situ transverse tensile strength of a lamina
w	Laminate width

Superscripts and Subscripts

ft	Fiber (longitudinal) tension
fc	Fiber (longitudinal) compression
is	In-situ
mt	Matrix (transverse) tension
mc	Matrix (transverse) compression
1, 2, 3	Longitudinal, transverse, thickness direction in a lamina
n, s, t	Normal direction, first shear direction, second shear direction



CHAPTER 1

INTRODUCTION

In the first part of this chapter, applications of composite laminates with holes are demonstrated, putting emphasis on open-hole tension and compression laminates. Next, different approaches for failure analysis are discussed. Damage characterization in open-hole laminates is introduced considering two types of damage, in-plane and delamination damage. Lastly, motivation, scope and outline of the thesis are presented.

1.1. Composite Laminates with Holes

Fiber reinforced composite laminated structures are extensively used in advanced engineering applications such as aircrafts, wind turbines, automobiles and marine vessels thanks to their advantages over traditional materials like steel and aluminum. Some of their advantages over traditional materials are higher strength to weight and stiffness to weight ratios, better resistance to corrosion and fatigue, and possibility to obtain desired mechanical properties by elastic tailoring. Use of composite materials in the aforementioned applications facilitates considerable energy savings thanks to high weight reductions.

Due to practical concerns, cutouts and holes ought to be created in composite laminates. For instance, cutouts in wing spars and cover panels of commercial transport airplane wings and military fighter wings are provided to form ports for mechanical and electrical systems, damage inspection, and fuel lines [1]. Holes are needed for joining purposes, as well. In aircraft industry, the drilling of the composite part is carried out for the purpose of joining using rivets and bolts [2]. In addition, it is also common to conduct tensile or compressive tests of

specimens with a carefully drilled hole to simulate unintentional natural defects that occur during composite fabrication and service life [3].

As a renowned authority on such matters, ASTM developed several standard test methods to determine the strength of composite laminates with holes in tension and compression. ASTM developed both open-hole [4,5] and filled-hole tension [6] and compression test standards considering different loads arising in different applications. This approach arises from the observation that tensile and compressive response of a composite laminate structure assembled with fasteners (bolts or rivets) that fill the hole and thus can transmit load across the hole is different from the response of a laminate containing hole loaded away from the hole [3]. Examples of filled-hole and open-hole tension laminates are provided in Figure 1-1 and Figure 1-2.



Figure 1-1 Filled-hole tension laminates after failure [7]



Figure 1-2 Open-hole tension laminate after failure

Although expensive, these tests are still needed to qualify a new aerospace system. Authorities would opt to waive much testing if the analysis and prediction of failure was more reliable. Waiving the testes would result in lower cost, more reliable composite structures and encourage more widespread usage of the composite materials across the industry [8]. Therefore, recent practice for composite researchers is focusing on virtual testing of composites. Virtual testing is defined as the capability to provide by simulation prediction of real physical behavior. Virtual testing is expected to provide not only structural strength but also progressive material damage up to failure [9]. The key to having more reliable virtual tests is ability to characterize composite damage better.

1.2. Damage in Laminated Composites

Early approaches in failure prediction in composite laminates were based on first ply failure. First ply failure approach assumes that laminate fails if any ply in the

laminate fails. This approach is very conservative for many laminates as laminates may bear far higher loads after first ply failure. Thus, keeping track of damage until ultimate laminate failure when all the plies fail has become a more practical approach. This approach is called “progressive failure analysis (PFA)”.

Damage characterization for progressive failure analysis should take into account different damage mechanisms corresponding to different regions of the laminate. Fiber-rich intra-ply region may experience failure due to tensile fiber fracture, local fiber kinking and buckling, matrix cracking, matrix polymer degradation due to environmental effects such as temperature, radiation and moisture [10]. Resin-rich inter-ply region; however, experiences a unique form of damage called “delamination”, which is simply the separation of adjacent plies from each other. Laminated composites with holes require special attention since the hole causes stress concentration that triggers in-plane damage around it and free surfaces of the hole are subject to high interlaminar stresses causing delamination [11]. Figure 1-3 shows inter-ply and intra-ply regions in a laminate and Figure 1-4 and Figure 1-5 illustrate several damage types observed in laminates loaded in tension.

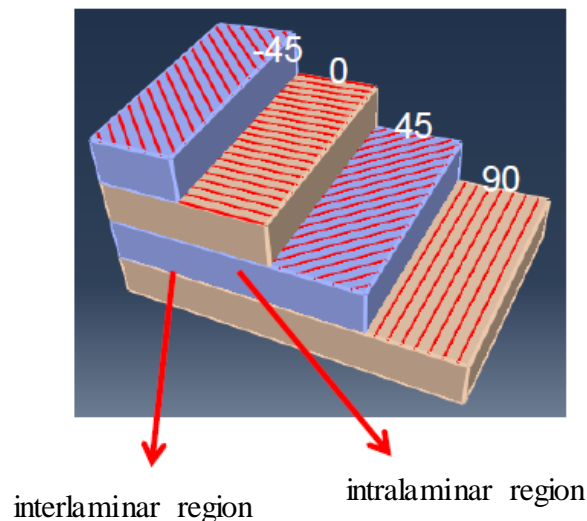


Figure 1-3 Inter-ply and intra-ply regions in a sub-laminate with lay-up [-45/0/45/90]

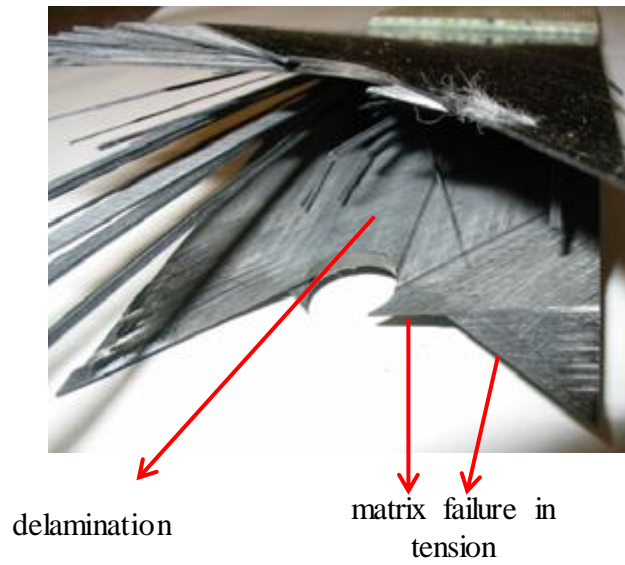


Figure 1-4 Laminate with extensive delamination failure [12]

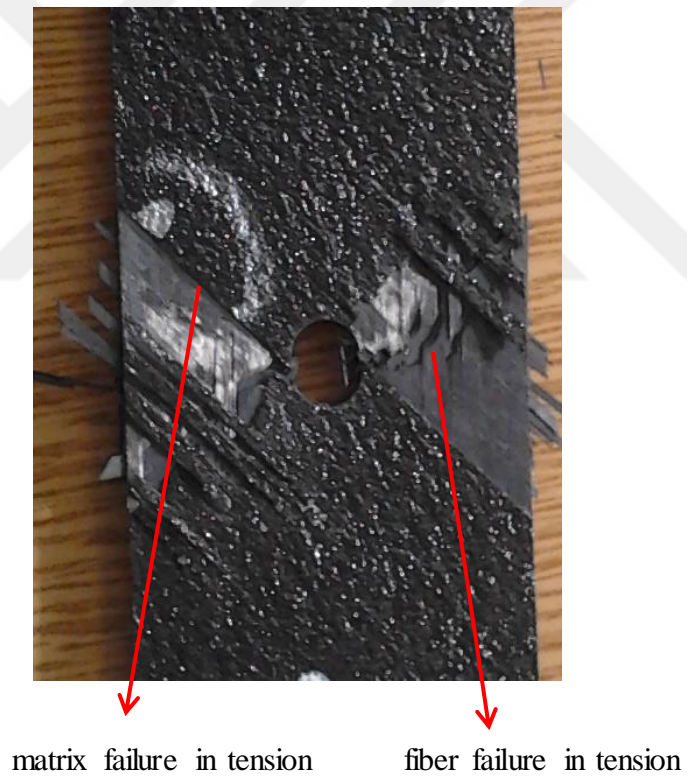


Figure 1-5 Laminate with fiber and matrix failure in tension

Intralaminar damage is due to the stresses in the plane of the ply while delamination is an out-of-plane failure stemming from interlaminar stresses.

Delamination failure is a common type of failure in laminated composites due to relatively weak resin-rich region between adjacent laminae. Interlaminar stresses developing due to mismatch of Poisson's ratio (ν_{xy}) and extension-shear coupling coefficients (m_x and m_y) in adjacent plies are the primary reasons for delamination failure [11]. In multidirectional laminates, laminae would deform freely if they were not bonded to each other. For instance, application of a load in x direction would result in different transverse normal strain in y direction due to different Poisson's ratios of the laminas. Similarly, the same load would cause laminas to have different shear strains because their extension-shear coupling coefficients are different due to different fiber angles. Since the laminas are bonded to each other in multidirectional laminates, adjacent laminas will be constrained to have identical shear strains and transverse normal strains, which would cause interlaminar stresses to develop. Geometric discontinuities, poor manufacturing process and curved sections are the other sources of delamination.

1.3. Damage in Laminated Composites with Holes

Having introduced types of intralaminar and interlaminar damage, damage patterns in laminated composites with holes will be discussed now. "Damage pattern" in this case is used to describe the manner a laminate fails. It is important to consider common damage patterns in laminated composites with holes because finite element models developed are verified on their ability to simulate these damage patterns. Although these damage patterns will be explained in detail in the upcoming chapters, a brief discussion will suffice now. Quasi-isotropic lay-up is extensively used for open-hole tension and compression laminates; therefore, the discussion will be based on damage patterns of quasi-isotropic open-hole tension laminates. Green et al. [13] observed that there are three main damage patterns associated with open-hole tension (OHT) laminates. These damage patterns are named in the study as "brittle", "pull-out", and "delamination" failure. In the brittle failure, all plies except 90° plies fail in fiber tension mode as shown in Figure 2-9. Fracture surface is smooth and parallel to side surfaces at short edges. Pull-out failure is characterized by fiber tension failure only in 0° plies, matrix tension failure in all other plies and moderate delamination at interfaces. A picture

of a laminate failed in pull-out damage pattern is shown in Figure 1-5. Lastly, delamination failure exhibits extensive delamination at interfaces and matrix tension failure at off-axis plies. In 0° plies, longitudinal splits form tangent to hole. Figure 1-4 shows a laminate exhibiting delamination damage pattern. Damage patterns in open-hole compression laminates are similar to their counterparts for open-hole tension laminates, although slight differences exist.

1.4. Damage Characterization

Damage characterization means detecting the correct type of damage and making necessary changes in the finite element model to simulate the effect of the damage during the loading history of the laminate. As shown in Figure 1-6, there are two stages of damage for intra-ply and inter-ply (delamination) damage characterization: damage initiation and damage evolution. The damage initiation, in other words, is the detection of damage, that is determining whether or not stresses at a material point satisfy the failure criteria. The damage evolution, on the other hand, is the process at which the material stiffness matrix is degraded as a result of the damage.

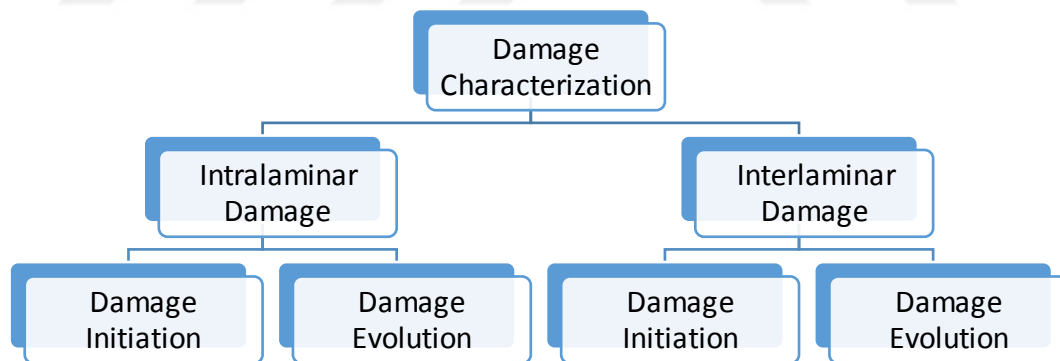


Figure 1-6 Damage characterization in laminated composites

In the progressive failure, load is incrementally applied, and stresses and strains at each load increment are determined. Then, damage initiation check is made with the available intra- and/or inter-laminar stresses. If the failure criterion used is satisfied for either a lamina (intralaminar region) or an interface (interlaminar

region), material properties of the corresponding region is degraded and load is re-distributed over the laminate. Stresses and strains at every material point is re-calculated with degraded material properties and failure is re-checked at the same load increment. If failure is detected, material properties are degraded again, else load is increased incrementally and the same procedure is applied again. Several block diagrams of different procedures to summarize the progressive failure process are available in literature [14,15].

1.4.1. Intra-ply Damage

Intra-ply damage detection is one of the most critical issues in PFA. The main problem for damage initiation criteria is that most failure criteria yield dependable results under certain loading conditions or for certain types of laminates. Thus, a great effort has been made by researchers to develop global damage initiation criteria that is valid for different cases. Several World Wide Failure Exercises have been organized to promote development and validation of failure criteria for different loading cases and laminates [16,17]. In this study, an extensive literature survey has been conducted about intra-ply damage initiation criteria in order to select a suitable criterion.

For intra-ply damage evolution, two methods are commonly used. These methods are instantaneous degradation and gradual degradation. In instantaneous degradation model, stiffness of the lamina is degraded instantaneously to a percentage of the original stiffness. Different residual values can be defined for each failure mechanism. It has been shown that instantaneous degradation model causes mesh-dependent results and severe convergence difficulties in implicit FEM [18]. In gradual damage evolution, accumulation of damage is represented by one or two damage parameters that affect stiffness matrix or the stress tensor of the lamina. Evolution of this parameter is usually linear or exponential as shown in Figure 1-7 [19]. Gradual damage evolution can be related to failure energy so that degradation is based on more phenomenological parameters that can be determined by experiments [20].

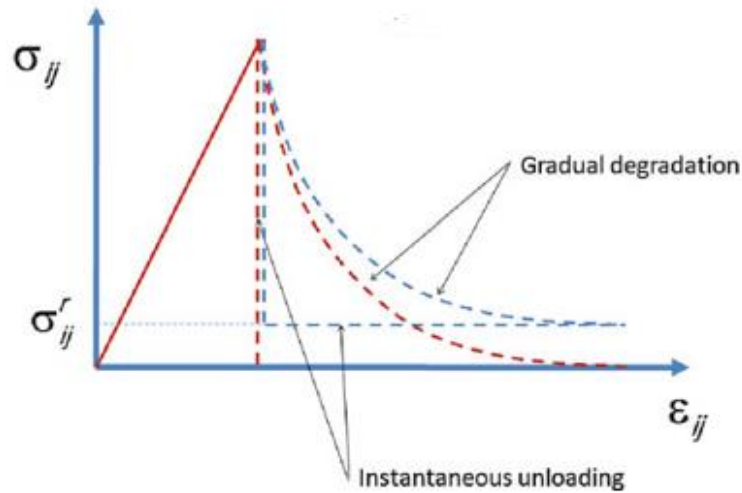


Figure 1-7 Stress vs strain graph in composite laminae for different degradation models where σ_{ij}^r denotes residual stress at the lamina after damage [19]

1.4.2. Inter-ply Damage

In a general loading, delamination is related to tractions associated with three different fracture modes that are Mode I, Mode II and Mode III modes, which can be described as crack opening mode, crack shearing mode and crack tearing mode, respectively, as shown in Figure 1-8.

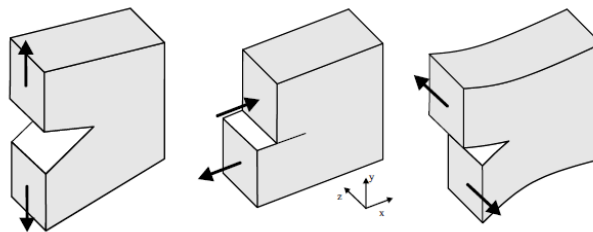
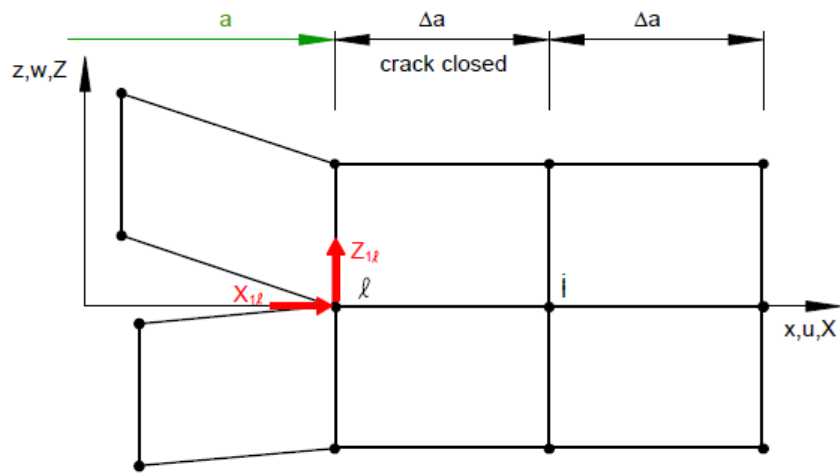


Figure 1-8 Crack propagation modes: Mode I, Mode II and Mode III from left to right [21]

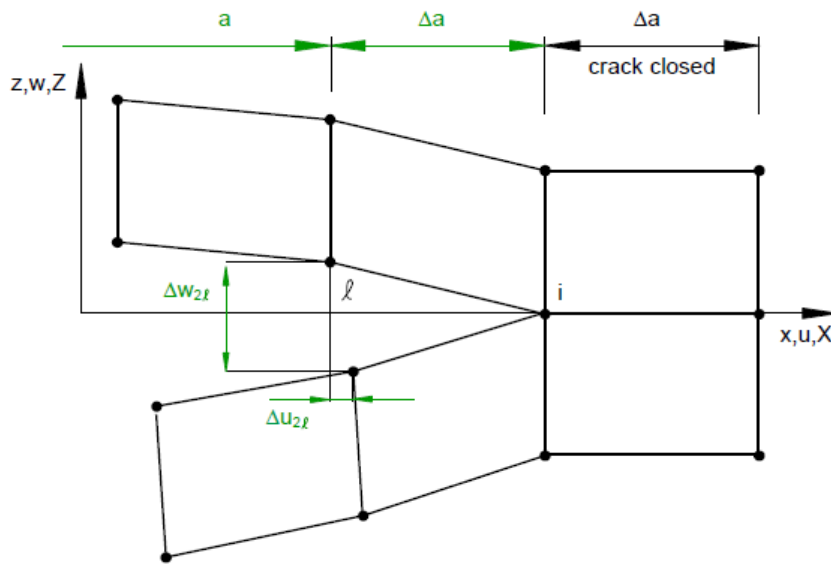
There are several methods available for numerical interlaminar damage characterization. These methods are based either on fracture mechanics or cohesive damage models [22]. Fracture mechanics based approaches such as Virtual Crack Closure Technique (VCCT), J-integral method and virtual crack extension method are able to predict the growth of a preexisting crack by

assuming a singular stress field at crack tip. These methods state that crack grows when combination of strain energy release rates in the three crack propagation modes exceed critical energy release rate, which is a property of the interface. Each method has a different way of calculating strain energy release rate. The most widely used method of the fracture mechanics based methods is VCCT. VCCT is based on linear elastic fracture mechanics and neglects the energy dissipated by formation of plastic zone ahead of the crack tip. VCCT assumes that energy released when a crack of length a extends to length $a + \Delta a$ is equal to the work needed to close the crack of length $a + \Delta a$ to a . In a finite element model, the energy released is computed from the nodal forces and displacements [23] as illustrated in Figure 1-9.





(a). First Step - Crack closed



(b). Second Step - Crack extended

Figure 1-9 Crack closure method with closed and extended crack configurations [24]

In delamination analysis of real composite structures, VCCT has some limitations such as the need for an existing crack to predict crack propagation and assumption that a crack grows in a self-similar fashion, i.e., the crack front maintains the same shape as the crack propagates [25].

Cohesive damage models, specifically Cohesive Zone Method (CZM), are traction-separation based approach with a mixed-mode loading modeling capability that accounts for effect of the aforementioned fracture modes. While energy release rate for a given crack growth path is calculated in fracture

mechanics based approaches, critical energy release rate determined by experiments is input for CZM to determine crack growth. Contrary to fracture mechanics based methods, Cohesive Zone Method (CZM) can predict both initiation and evolution of delamination crack and existence of a preliminary crack is not necessary for CZM to predict crack growth, which is one of the major advantages of CZM over VCCT. Moreover, having modeled DCB test both with CZM and VCCT, Gözlüklü [26] claims that VCCT requires finer meshes although both methods are mesh dependent.

In this study, CZM will be utilized in order to model delamination. In CZM, traction in the interface is degraded to zero gradually as the displacement between the interfaces increases. For finite element modeling, cohesive elements are placed at interfaces with high potential of delamination. Figure 1-10 shows a double cantilever beam test simulation, where cohesive layer is placed along the crack.

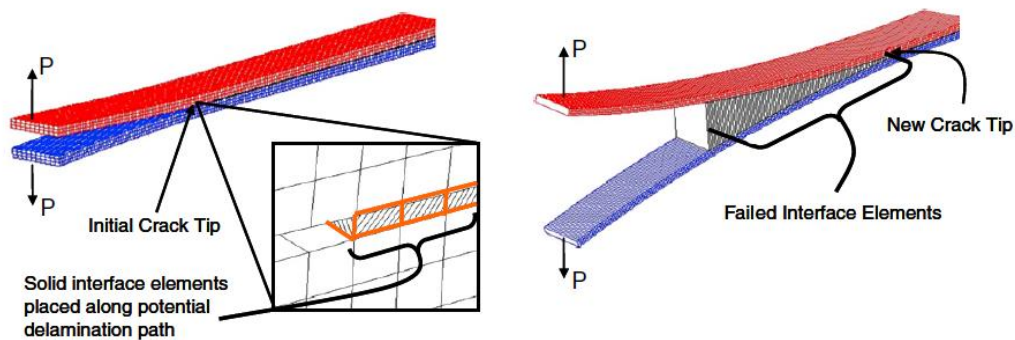


Figure 1-10 Cohesive layer comprised of interface elements in DCB test modeling [27]

In laminated composites, cohesive layers are placed between adjacent composite layers. This approach is compatible with the nature of laminated composites since delaminations in laminated composites are constrained to propagate in its own plane because the toughness of the interface is relatively low in comparison to that of the adjoining material [22].

Damage initiation criteria and damage evolution laws for CZM are discussed in detail in Chapter 3.

1.5. Motivation

Damage characterization of laminated composites with holes constitutes many challenges since they exhibit different types of damage called intralaminar and interlaminar damage that interact with each other. Therefore, initiation and evolution of one type of damage may trigger the other type of damage easily. Thus, ignoring or wrong modeling one of the damage types may lead to inaccurate simulation of damage. Correct modeling of the damage requires applying appropriate intralaminar and interlaminar damage initiation and evolution criteria and determining parameter required for the simulation appropriately. The motivation behind this study is to develop a finite element model that is capable of visualizing the damage throughout the loading history of the laminates with holes.

1.6. Scope of Thesis

In this study, a finite element modeling methodology will be suggested to model progressive failure of open-hole tension laminates to track the damage from the beginning to the end of loading. Several laminates exhibiting brittle, pull-out, and delamination damage will be modeled in order to test the model's applicability to different damage patterns common for OHT laminates. The cases will be chosen from the literature [13] and open-hole tension tests conducted at Mechanical Engineering Department of METU in scope of the SANTEZ project called "Design Methodology for Thick Composite Laminates". Cohesive Zone Method (CZM) will be implemented in order to model delamination. Effect of delamination on prediction of ultimate load and damage progression is also studied. With the experience gained from open-hole tension laminates, suggestions will be made for damage characterization of open-hole compression laminates throughout the text where appropriate.

1.7. Outline

This chapter introduces the damage in laminated composites with holes and basic concepts about damage characterization in them.

Chapter 2 is devoted to the literature survey about intralaminar failure criteria and studies including tests and finite element analyses of laminated composites with holes.

Chapter 3 includes theoretical background for intralaminar and interlaminar composite failure. Intralaminar and interlaminar damage initiation and evolution criteria utilized in the study are discussed. Constitutive response of CZM is explained in this chapter.

Chapter 4 is devoted to the benchmark tests (experiments) that will be used to verify finite element method developed. Tension tests of three benchmark coupons are introduced in this chapter. Tensile test of one of the coupons is conducted in the scope of the study. Tests of other two coupons are obtained from the literature.

Chapter 5 discusses the finite element method utilized and details of the finite element model developed for the three coupons. Determination of parameters input to FEA software (Abaqus®) for the simulation of intralaminar and interlaminar damage is explained in this chapter.

In Chapter 6, results of the FEA are provided and compared to experimental results. Effect of delamination on damage progression in the three different laminates is discussed.

In Chapter 7, the study is summarized first. Then, discussions and future studies are provided putting emphasis on the discussion of methods proposed to improve the model developed.

CHAPTER 2

LITERATURE SURVEY

This chapter is divided into three parts. In the first part, a chronological development of mode-dependent failure criteria and popular failure criteria utilized for intralaminar damage characterization in open-hole composite laminates are discussed. In “Tests and Analyses” section, firstly benchmark tests that are commonly utilized for validation of progressive failure analyses of open-hole laminates are summarized. Then, studies including finite element analysis of open-hole laminates are presented, emphasizing methodologies used in the studies. Finally, conclusions from the literature survey will be summarized to mention critical points that might be beneficial in constructing finite element model for this study.

2.1. Intralaminar Failure Criteria

The onset of intralaminar damage can be checked by the intralaminar damage initiation criteria. Intralaminar damage initiation criteria are mathematical relations used to determine whether a structure will fail or not under given stresses or strains when the structure is subjected to uniaxial, biaxial or multi-axial loadings. Most of the failure criteria check the failure utilizing stresses in each lamina. In this type of failure criteria, lamina stresses are inserted in failure relations to check if they exceed certain limits defined for the lamina strength. The lamina level failure criteria are discussed in detail in the following sections. Although not so common, few failure criteria decompose lamina stresses into fiber and matrix stresses and insert them in the failure relation to check strength limits determined by fiber strength or matrix strength. This type of failure criterion is called constituent based one. In this approach, mechanical properties of laminae are predicted by utilizing experimental data on fiber and matrix

properties. On the other hand, in lamina level criteria, lamina properties are determined by tests conducted on the lamina itself. In World Wide Failure Exercise-I (WWFE-I) [28], research participants of the program using constituent based criteria were not able to obtain accurate laminate strength [28].

Failure criteria can be classified into two categories based on the failure mode which can be expressed as the nature of damage forming in different types such as fiber tensile, fiber compressive, matrix tensile and matrix compressive failure [29]. If a failure criterion considers the failure mode to check failure by applying different sub-criterion for each mode, it is called as the mode-dependent failure criterion. Otherwise, when the same failure relation is used for all kinds of loading, it is called as the mode-independent failure criterion.

One of the most commonly used mode-independent failure criteria is Tsai-Wu criterion [30] given by Eq. (2-1) for plane stress state.

$$F_1\sigma_1 + F_2\sigma_2 + F_{11}\sigma_1^2 + F_{22}\sigma_2^2 + F_{66}\sigma_6^2 + F_{12}\sigma_1\sigma_2 = 1 \quad (2-1)$$

The cross-reference terms, F_{ij} , in Eq. (2-1) denote the coefficients formed by combinations of uniaxial tensile strength in longitudinal and transverse directions, uniaxial compressive strength in longitudinal and transverse directions and shear strength of the lamina where subscript 1 is associated with longitudinal (fiber) direction, 2 with transverse direction, and 6 with in-plane shear. σ_1 , σ_2 , and σ_6 represent longitudinal stress, transverse stress, and shear stress in the lamina, respectively.

The concept of mode dependent failure criterion was first suggested by Hashin [31]. In 1973, based on experimental observations, Hashin came up with two different failure criteria, one related to fiber failure and the other to matrix failure. The criteria assumed a quadratic interaction between the tractions acting on the plane of failure. Later, in 1980, he introduced fiber and matrix failure criteria [32] that distinguish between tension and compression failure. Given the difficulty in obtaining the plane of fracture for the matrix compression mode, Hashin used a

quadratic interaction between stress invariants [33]. Analytical descriptions of the failure modes are shown in Eq. (2-2) – (2-5) for plane stress state:

Fiber tensile mode ($\sigma_{11} \geq 0$):

$$\left(\frac{\sigma_{11}}{X^T}\right)^2 + \left(\frac{\tau_{12}}{S^L}\right)^2 = 1 \quad (2-2)$$

Fiber compressive mode ($\sigma_{11} < 0$):

$$\left(\frac{\sigma_{11}}{X^C}\right)^2 = 1 \quad (2-3)$$

Matrix tensile mode ($\sigma_{22} \geq 0$):

$$\left(\frac{\sigma_{22}}{Y^T}\right)^2 + \left(\frac{\tau_{12}}{S^L}\right)^2 = 1 \quad (2-4)$$

Matrix compressive mode ($\sigma_{22} < 0$):

$$\left(\frac{\sigma_{22}}{2S^T}\right)^2 + \left(\frac{\tau_{12}}{S^L}\right)^2 + \left[\left(\frac{Y^C}{2S^T}\right)^2 - 1\right] \frac{\sigma_{22}}{Y^C} = 1 \quad (2-5)$$

X^T : Tensile strength in longitudinal direction

X^C : Compressive strength in longitudinal direction

Y^T : Tensile strength in transverse direction

Y^C : Compressive strength in transverse direction

S^L : Longitudinal shear strength

S^T : Transverse shear strength

σ_{ij} : Elements of lamina stress tensor, 11:longitudinal direction, 22:transverse direction 12: shear

Hashin's failure criterion for plane stress is available in Abaqus®, which is a popular FEA software for composite damage researchers, and it can be used with 3-D continuum shell and 2-D conventional shell elements.

Pioneer of mode-dependent failure criterion concept, Hashin has inspired many researchers since the introduction of his failure criterion. However, Hashin's failure criterion performed poorly in predicting damage under transverse

compressive loads and in-plane shear. For instance, moderate transverse compressive stresses increase actual shear strength (different from shear strength measured by lamina coupon tests) of the plies and in-plane shear stresses reduce actual longitudinal compressive strength of the plies, which are not captured by Hashin's criterion [33].

Sun et al. [34] replaced denominator in Eq. (2-4) with $(S^L - \eta' \sigma_{22})$ where η' is internal friction parameter determined experimentally and compressive σ_{22} is negative by convention. Note that as transverse compression increases, actual shear strength $(S^L - \eta' \sigma_{22})$ decreases.

Puck and Schürmann [35] have suggested a failure criterion that accounts for fiber kinking by decreasing the longitudinal compressive strength under in-plane shear. Unlike Hashin and Sun, they predicted plane of fracture under combined transverse normal and in-plane shear loads and decomposed transverse normal and in-plane shear stresses into longitudinal shear, transverse shear and normal stresses acting on the fracture plane. Instead of directly relating increase of compressive transverse stresses to increase of shear strength, Puck and Schürmann assumed that normal stress acting on the fracture plane affects actual shear strength of the plies. Although work of Puck and Schürmann has been a great breakthrough in composite damage prediction, their semi-empirical method requires several non-physical material parameters that may be hard to obtain without considerable experience with a particular material and their method did not consider in-situ effect, which may underestimate strength of thin plies located between plies with different angles [33,35].

Motivated by the fact that there is a lack of faith in the failure criteria in use, World Wide Failure Exercise-I was organized by a group of researchers from the UK. Aim of WWFE-I was to provide researchers and engineers with reliable failure prediction methods, give them confidence to use them and to establish the current level of maturity of theories for predicting the failure response of fibre reinforced plastic laminates [36]. Six different laminate types including unidirectional, angle ply, cross ply, quasi-isotropic laminates were combined with

various loading conditions to generate a total of fourteen test cases. Nineteen failure criteria was evaluated under those test cases [37].

Approaches ranked most highly by the aforementioned exercise are the theories of Zinoviev, Bogetti, Puck and Cuntze. Theories of Puck and Cuntze had the highest number of accurate predictions (i.e. within $\pm 10\%$ of the experimental data) and captured more general features of the experimental results and laminate behavior than the other theories. Cuntze's approach is similar to Puck's approach considering some aspects; however, it suggests that there is interaction between failure modes due to probabilistic effects.

Examining Figure 2-1 and Figure 2-2, it can be seen that Puck failure criterion predicted transverse normal stress vs. in-plane shear stress ($\sigma_y - \tau_{xy}$) failure envelope for a lamina better than the other criteria; however, it was a little unconservative in predicting tensional longitudinal normal stress vs. transverse compressive stress quadrant of ($\sigma_x - \sigma_y$) failure envelope. Thus, WWFE-I organizers recommended Tsai and Puck criteria to be used together for lamina-level failure prediction [28].

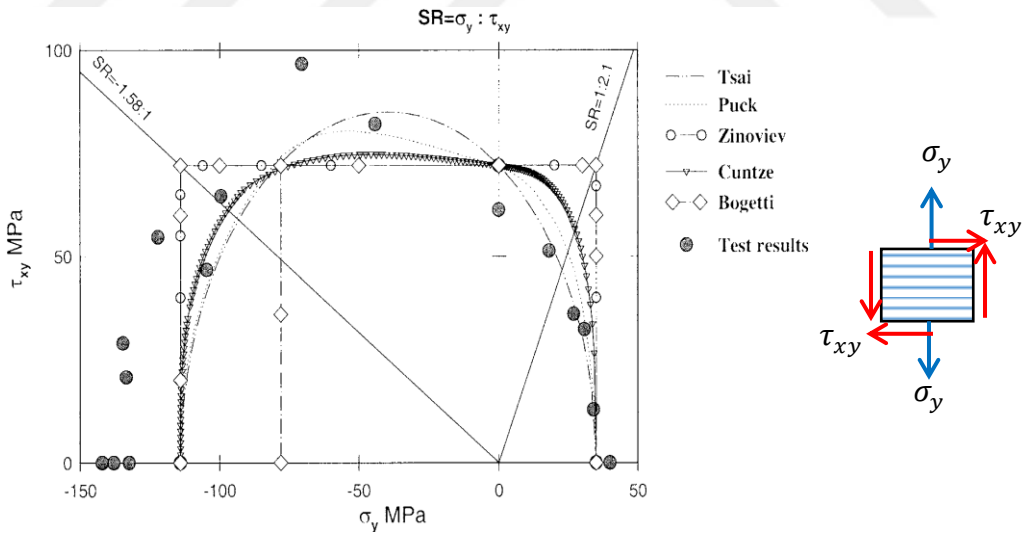


Figure 2-1 Comparison of failure envelopes predicted by experimental data for glass/epoxy lamina subjected to in-plane shear and transverse normal stresses [28]

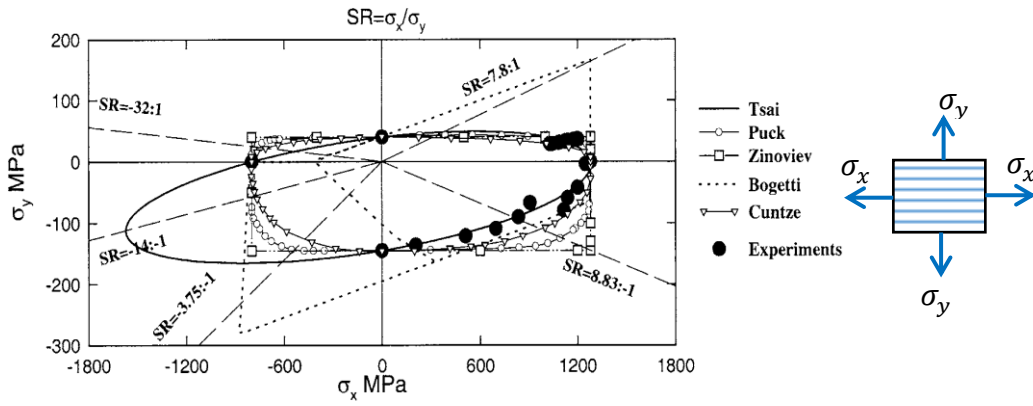


Figure 2-2 Comparison of failure envelopes predicted by experimental data for glass/epoxy lamina subjected to biaxial normal stresses in directions parallel (σ_x) and perpendicular (σ_y) to the fibers [28].

When quasi-isotropic laminate is tested bi-axially, however, Puck criterion provided a better prediction for the failure envelope compared to Tsai criterion under bi-axial compression as seen in Figure 2-3.

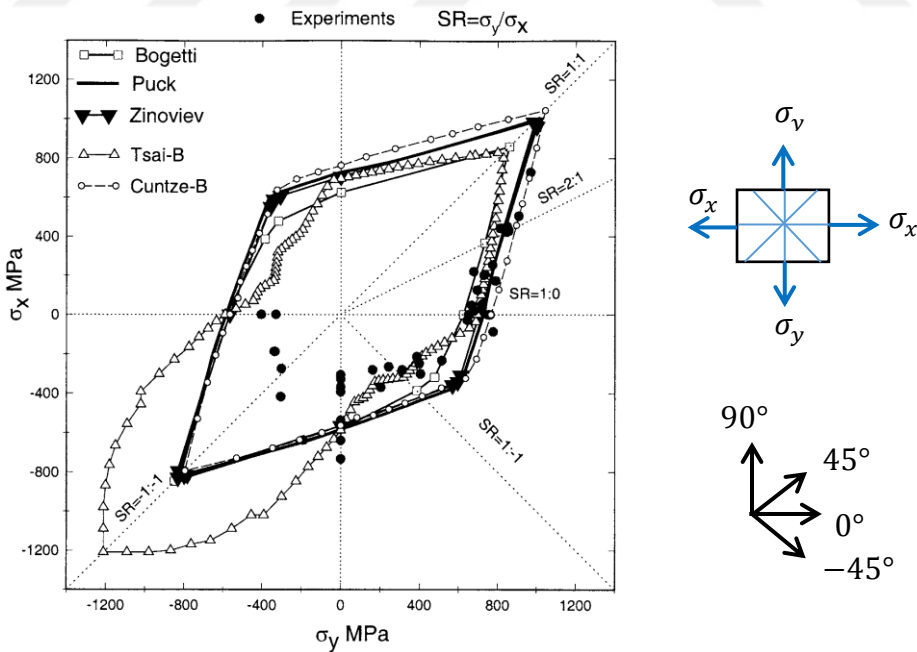


Figure 2-3 Comparison between the predicted and measured final failure stresses for $[0^\circ/\pm 45^\circ/90^\circ]$ carbon/epoxy laminates subjected to biaxial loads [28]

None of the failure theories was able to predict with great accuracy the failure envelope for biaxial loading of multidirectional quasi-isotropic laminates, especially when both stresses are compressive. Soden et al. [28] recommended Puck and Cuntze's theories for prediction of final failure strength of composite laminates. Moreover, none of the theories were able to capture large non-linear deformations of laminates seen at high strains.

All in all, one should bear in mind that most of the failure criteria are suitable for a particular loading and laminate type; thus, attention needs to be paid to before making use of failure criteria. It should also be noted that 3-D failure criteria and stress systems, delamination initiation and propagation were not addressed by WWFE-I.

Eight of the failure theories studied in WWFE-I were revised to account for failure under 3-D stress state and to solve their deficiencies. For instance, Puck's failure criterion [35] were modified not only for accounting for 3-D stress state but also for the in-situ strengths of unidirectional plies. As a result of the evaluation, it was seen that no two models gave identical predictions for any of 12 test cases, which does not render the theories useless. Nevertheless, many theories agreed that the application of compressive through-thickness stress leads to an increase in the shear strength of a UD lamina and in the through-thickness shear strength of the multi-directional laminates [38].

One more failure exercise, WWFE-III was performed in order to deal with matrix cracks due to thermal and mechanical loads, delamination, ply constraint and stacking sequence effects, loading and unloading phenomena and failure due to the hole size effect. Although results of the theories varied extensively from each other, this exercise helped advanced topics regarding composite failure to be discussed [39].

Inspired by the concepts developed by Hashin and Puck, Davila et al. [33] developed a new phenomenological failure criterion called Larc03. Larc03 is an in-plane failure criterion which is advantageous over Puck criterion in some aspects. For instance, both Larc03 and Puck criteria make use of fracture plane concept. While fracture plane angle in combined transverse compression and in-

plane shear is obtained by experimental observations in Puck criterion, Larc03 criterion is able to calculate it analytically. Moreover, Larc03 criterion takes into account in-situ strength by proposing an analytical method to calculate in-situ strength of the plies analytically and utilizing them in matrix tension failure criterion. Failure of thin and thick plies are dealt with separately. In the case of fiber compression failure, only fiber kinking was considered. Stating that fiber kinking is a result of shear deformation, stresses in the fiber misalignment frame were inserted in matrix failure criterion to check for fiber kinking failure. Later, Larc03 criterion was modified to account for 3-D stress state and non-linear behavior of shear stress-strain characteristics of a lamina and new criterion was named as Larc04 [40]. Also modified were friction terms in matrix failure, which resulted in good agreement with experimental data in combined transverse compression and in-plane shear of a lamina as in Figure 2-4. Larc04 criterion was verified by cross ply laminate compression tests for various ply angles and showed excellent agreement with experimental data as seen in Figure 2-5, whereas Hashin's criterion performed poorly in predicting compressive strengths of angle-ply laminates at high angles since it did not consider increase in shear strength due to transverse compression. Developers of Larc04 stated that the criterion is accurate for carbon fiber laminates; however, a more general model would be needed to account for fiber buckling and fiber failure itself besides fiber kinking.

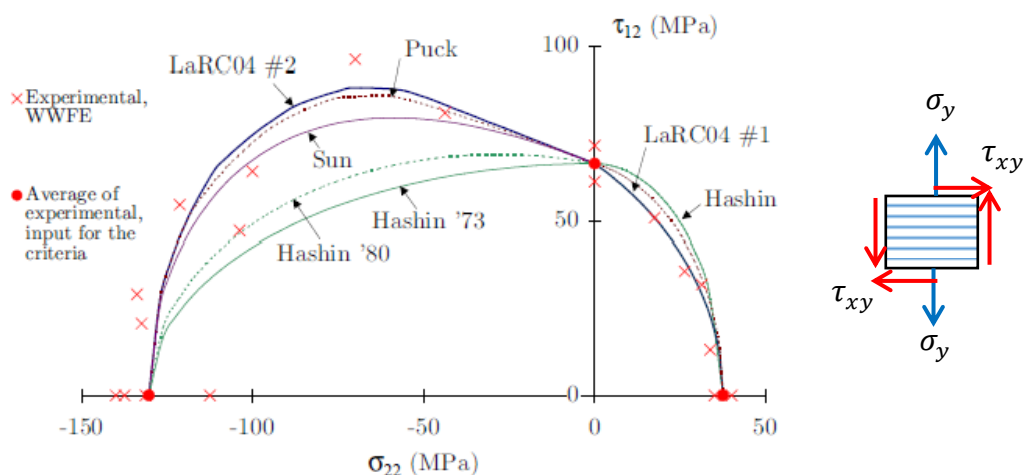


Figure 2-4 Failure envelopes and WWFE test data for unidirectional composite E-Glass/LY556 under combined transverse normal and in-plane shear stresses [40]

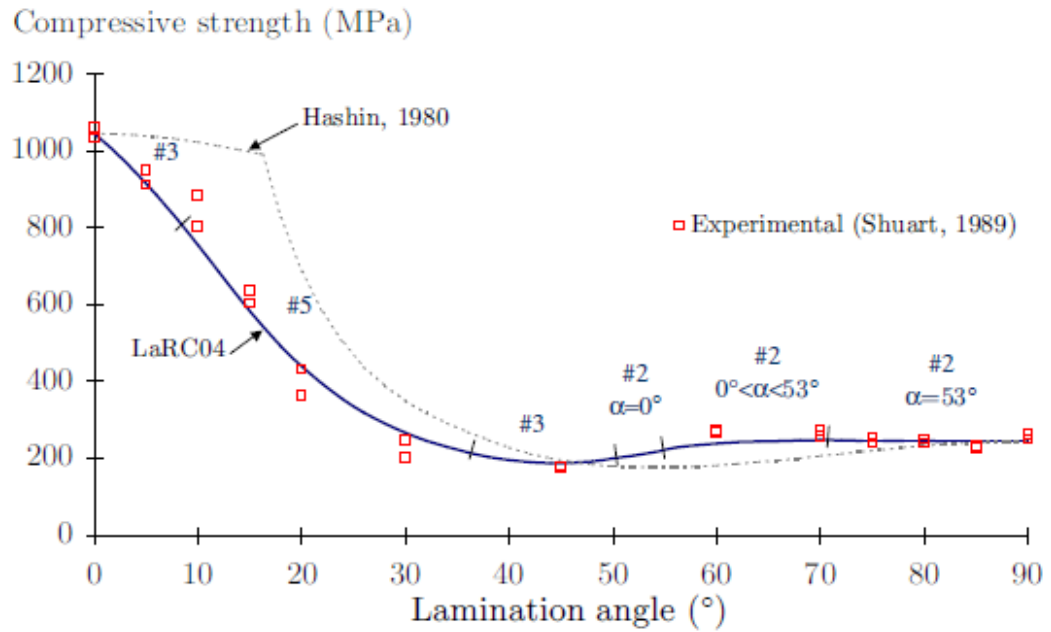


Figure 2-5 Compressive strength as a function of ply orientation for AS4-3502 $[\pm\theta]_s$ laminates (α stands for angle of fracture plane) [40]

2.2. Tests and Analyses

Before elaborating on open-hole laminate FEA in the literature, it will be useful to describe in detail common failure patterns in quasi-isotropic open-hole composite laminates with the help of extensive experimental work carried out by Green et al. [13]. Green et al. [13] investigated scaling effects in quasi-isotropic carbon/epoxy open hole tension laminates with lay-up $[45_m/90_m/-45_m/0_m]_{ns}$ where m and n represent the number of plies or sublaminates stacked together, respectively, and they are used to control the thickness of the laminate. Changing the laminate thickness by changing m is called as ply scaling, while changing the laminate thickness by changing n is named as sublaminate scaling. Laminate width-to-hole diameter and laminate length-to-hole diameter ratios were kept constant during the experiments while four different hole diameters and laminate thicknesses were utilized. Figure 2-6 depicts the three distinct failure patterns observed in the experiments; namely, brittle, pull-out and delamination failure patterns.

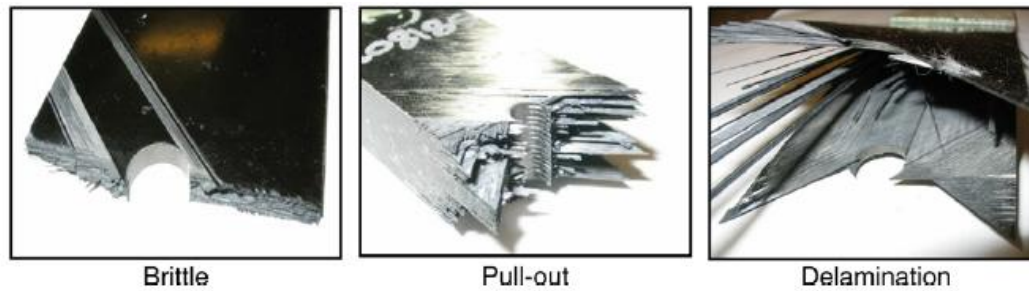


Figure 2-6 Three different failure mechanisms observed depending on scaling regime and specimen dimensions [12]

Brittle failure is highly fiber-dominated and very little delamination is observed. It is observed in brittle failure that fibers fracture in all plies creating a smooth fracture surface. In pull-out failure pattern, only 0° plies experienced fiber failure while others failed by splitting (matrix failure) of the ply and delamination between layers resulting in after-fracture state as shown in Figure 2-1. Last type of failure pattern, delamination failure is dominated by delamination at $-45/0$ interface covering a large area along with splitting of the off-axis plies. Consequently, as seen in Figure 2-7, when the in-plane dimensions of the laminate is kept constant, if the thickness of the laminate is increased by sublaminates blocking failure stresses decrease slightly in the beginning, then remain almost constant. If the thickness is increased by ply-blocking; however, possibility of delamination failure increases significantly, leading to high decrease in failure stress.

Hallett et al. [12], in a joint research with Green et al.[13], developed a finite element model in which cohesive elements were used between the layers and in the plies to simulate delamination and intralaminar splitting. Intralaminar splitting was simulated by inserting cohesive elements to lines of potential strips in the plies as shown in Figure 2-8. No fiber failure criterion was used in the analysis. Rather, fiber failure was checked by post-processing using a Weibull volumetric statistical strength theory-based fiber failure criterion. FEA strength results were in good agreement with the experiments [13] for most of the specimens but FEA was unable to predict whether a laminate failed by pull-out or brittle failure since

there was no fiber failure criterion that affected stress re-distribution in the analysis.

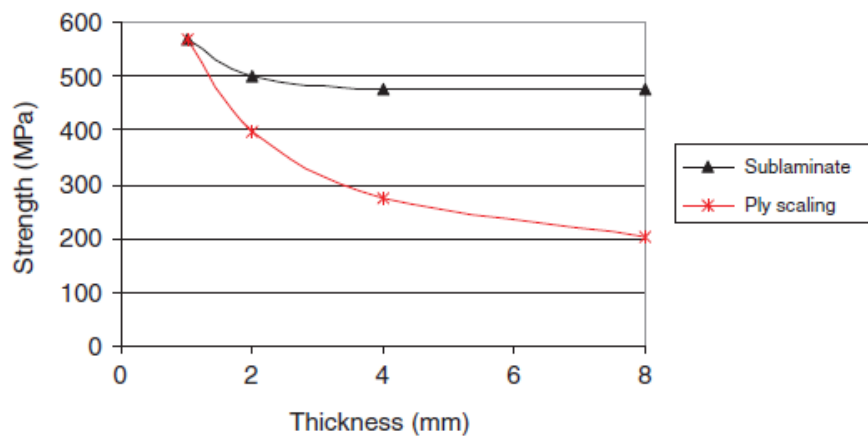


Figure 2-7 Effect of thickness on open hole tensile strengths [41]

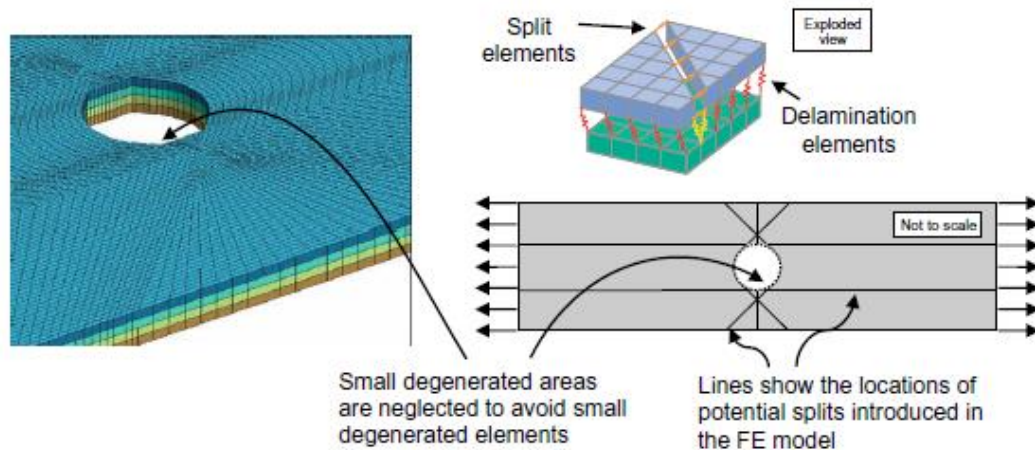


Figure 2-8 Location of potential strip lines (lines with different orientation angles belong to different plies) [8]

Another joint research based on the previous two works [12,13] is the work of Wisnom et al. [41]. Wisnom et al. [41] investigated failure patterns of open hole compression laminates and effects of scaling on open hole compression strength of the laminates, comparing the results with the results of open hole tension tests. It was observed that open-hole compression specimens exhibit similar failure patterns to open-hole tension specimens. Main mode of failures observed are brittle, push-out and delamination failure that are quite similar to their counterparts observed in open-hole tension tests. Kink-band approach is utilized in order to predict fiber micro-buckling in fiber compression along with cohesive

elements both in intra-ply and inter-ply regions as in [12]. It was concluded that even though compression specimens has lower strength compared to tension specimens, they performed better when the notched strength-to-unnotched strength ratio is considered. Although the strength predicted by FEA and measured in the experiments were close to each other, it is a disadvantage for the failure criterion used not to include the effect of transverse compressive stresses on shear strength of the plies.

Satyanarayana et al. [42] developed finite element models for open hole tension laminates with stacking sequences $[45/90/-45/0]_S$, $[45_2/90_2/-45_2/0_2]_S$, $[45_4/90_4/-45_4/0_4]_S$ and $[45/90/-45/0]_{4S}$ and compared analyses' results with the results from Green et al. [13]'s study. Their model was constructed in Abaqus® Explicit using a VUMAT subroutine. 3-D continuum shell elements were used for intralaminar regions, while 3-D cohesive elements were implemented in the interfaces that had plies with different orientations. Damage initiation criterion was based on Hashin-Rotem's failure initiation criterion and an instantaneous damage evolution model where stiffness of failed material points are degraded to zero instantaneously. The failure criterion used differs from Abaqus®'s built-in failure criterion by degrading matrix stresses as well in the case of fiber failure. In-situ transverse tensile strength and shear strength of the plies are considered. In-situ strength takes into account the increase in transverse tensile and shear strengths when 90° plies are constrained by plies with different angles. It was observed that $[45/90/-45/0]_S$, $[45_2/90_2/-45_2/0_2]_S$, $[45_4/90_4/-45_4/0_4]_S$ and $[45/90/-45/0]_{4S}$ laminates showed brittle, pull-out and delamination and brittle failure patterns, respectively, agreeing with the experimental results [6]. For instance, in the analysis of $[45/90/-45/0]_{4S}$ laminate a clean fracture surface was obtained as shown in Figure 2-9.

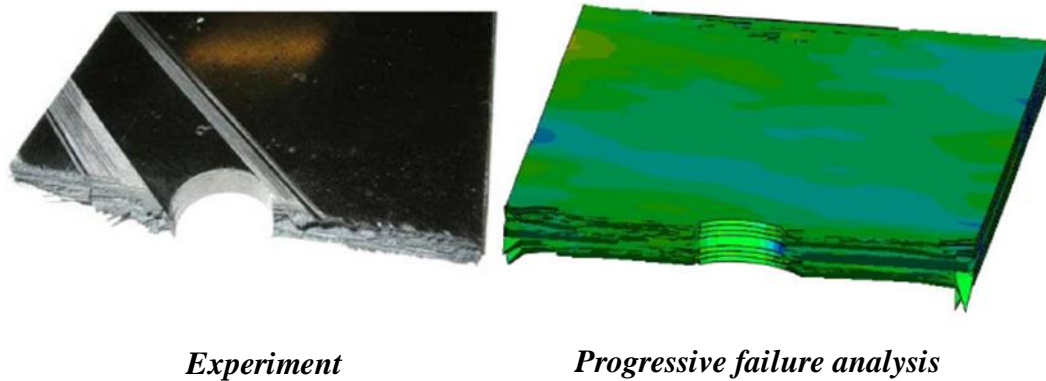


Figure 2-9 Crack path in $[45/90/-45/0]_{4S}$ laminate [42]

An important breakthrough in composite laminate damage characterization was achieved by Camanho et al. [43]. They stated that instantaneous degradation yields mesh dependent results since finite element discretization is not taken into account. Motivated by this problem, they proposed a damage degradation model whereby stiffness matrix of the laminate is degraded based on an energy criterion. This energy criterion was then related to fracture energy of the plies, which not only allowed use of measurable material properties to characterize damage but also got over mesh dependency problem. Investigating the effect of mesh dependence on damage progression on a simple geometry, Lapczyk and Hurtado [44] also confirmed that the method suggested by Camanho et al. [43] alleviates mesh dependence problem significantly, but not completely for more general cases. Failure energies for matrix based failure modes were obtained by double cantilever beam (DCB) and end notched fracture (ENF) tests, fiber dominated longitudinal fracture energies were obtained by compact tension and compact compression tests as suggested by Pinho et al. [45]. Camanho et al. [43] investigated size effects in sublaminates scaled open hole tension laminates by utilizing Larc04 intra-ply failure criterion involving in-situ strengths; however, they did not implement cohesive elements between layers stating that delamination is not the prevalent damage mechanism in sublaminates scaled laminates. Another advantage of this model was that the model would be used to predict damage behavior of the laminate under compressive loading as well, since

Larc04 criterion involves many improvements in fiber and matrix compressive failure mode over other commonly used failure criteria.

Song et al. [46] utilized energy based stiffness degradation suggested by Camanho et al. [43] and stated that continuum damage mechanics based intralaminar damage models used together with interlaminar cohesive layer model cannot predict laminate failure sequence when the two failure mechanisms are coupled to each other i.e. when laminate shows high delamination behavior. They proved by compact tension analyses that crack in a ply tend to propagate in preferred element directions: parallel to element side or diagonally. Therefore, in their FEM, they utilized mesh aligned with fiber orientation for each layer and tied different layers with tie constraints. 3-D continuum shell elements were used for intra-ply regions, while 3-D cohesive elements were utilized for inter-ply regions. Hashin's failure criteria for intra-ply damage, quadratic delamination initiation criterion and BK Law for mode-mix were utilized in the FEA conducted by Abaqus® Explicit. They also compared aligned mesh with radial mesh that is one of the most common mesh patterns to analyze open-hole laminates. Consequently, when compared with experiments, OHT analyses of graphite/epoxy laminate with aligned mesh performed better than the analyses with radial mesh, which is very common in OHT analyses. According to results of the analyses, even though predicted failure patterns matched experimental data, predicted failure loads were lower compared to tests when the dominant failure type was pull-out, and higher when dominant failure type was delamination. This discrepancy was attributed to late prediction of delamination damage in the interfaces; which was thought to be resulting from the late prediction of matrix failure.

Another study based on Camanho et al. [43]'s achievements was conducted by Nikishkov et al. [47]. In the study, damage progression in a quasi-isotropic carbon/epoxy laminate was investigated by utilizing 3-D solid elements and cohesive elements. Strength of materials based Hashin's matrix failure criterion and fracture mechanics based matrix failure criterion proposed by Davila et al. [40] was implemented in FEM for comparison. Shear non-linearity effect was included in matrix failure criterion since it was claimed based on experimental evidence that composite laminates exhibit nonlinear shear stress – shear strain

relation before first crack initiation. It was observed that standard structural mesh was not able to predict accurate damage progression and predict ultimate failure loads; thus, fiber-oriented mesh was applied for each separate ply as in [46]. Damage progression obtained by the finite element analyses were compared with test data obtained by X-ray imaging and Digital Image Correlation and it was concluded that Hashin's matrix criterion was unsuccessful at ultimate crack prediction, while fracture mechanics based approach resulted in close agreement with experimental findings. The authors did not discuss, however, about the implementation of fiber failure criteria.

Ridha et al. [48] studied damage behavior of a wide range of open hole tension laminates with plies oriented at 0° , 45° , -45° and 90° . Laminates with different number of blocked 0° or 90° plies leading to different orthotropy ratios (E_x/E_y) were studied (note that orthotropy ratio of quasi-isotropic laminates is 1) and results were compared to experiments conducted by Dharmawan et al. [49]. Maximum Stress and Tsai-Wu criteria were combined to detect intra-ply failure, energy based degradation based on [43] was utilized for intralaminar and interlaminar stiffness degradation, and 3-D cohesive elements were utilized to detect delamination in Abaqus® Implicit analyses. Matrix transverse compression mode failure criterion was not included in the model since that mode was regarded as negligible in the tension test. 3-D continuum shell elements were used in the models that consider delamination, while 2-D conventional shell elements were utilized when delamination was not considered. The novelty of this study was the methods utilized to improve convergence and decrease computation time. One of the methods was to use a zigzagging degradation curve with piecewise constant stiffness as shown in Figure 2-10 so that stiffness of the material does not change continuously during damage progression, decreasing computational time considerably. The other method was to set a lower limit to time increment below which the stress is not updated by UMAT subroutine, while stiffness was still degraded, forcing stress to converge when time increment fell below the set limit. Blocking of 0° plies were considered by utilizing twice the longitudinal fracture toughness of unblocked plies in the analyses, which resulted in a good agreement of the analyses with experiments for low number of blocked 0° plies, but

underestimated laminate strength considerably for high number of blocked 0° plies. It was stated that material data obtained from [43] was utilized for transverse strength of the plies; however, no information was given about whether in-situ effect was considered for blocking 90° plies. As a result, it was observed that finite element models that do not consider delamination overestimated laminate strength, even in the case of sublaminates-scaled $[45/0/-45/90]_{3s}$ laminates.

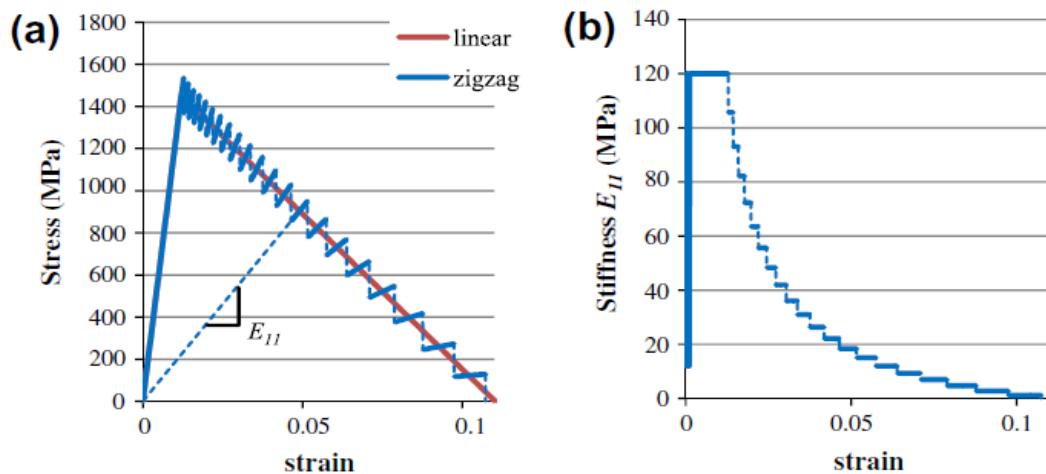


Figure 2-10 Zigzag approximation of the linear softening law (a) and corresponding stiffness degradation (b)

Although considerable progress has been achieved in simulation of damage in open hole tension laminates, modeling damage in open hole compression laminates has remained as a more complicated task due to complications such as convergence problems due to instability under compression and modeling of local buckling [50]. Su et al. [50] utilized finite element model developed by Ridha et al. [48] for open hole tension laminates and modified that model to simulate damage in open hole compression laminates by changing intra-ply failure criterion to include matrix compression failure mode. It was mentioned that aforementioned difficulties has been mitigated by applying zigzagging degradation model as in Ridha et al. [48]'s work and utilizing continuum shell elements that account for out-of-plane deformation. Micro buckling was not explicitly modeled, however. Longitudinal compressive translaminar fracture

toughness measured by compact compression tests were input in the analysis to simulate fiber kinking in fiber compression. Increase in the fracture toughness was assumed with increasing number of blocked plies of the same angle. Analyses results were compared with experimental data of Lee and Soutis [8] and high agreement was found in terms of laminate strengths and failure patterns. Bulging around the hole due to compression, which is a sign of buckling, was also captured by the analyses, on which Su et al. [50] commented that explicit modeling of buckling might not be necessary since their model was already able to capture it.

2.3. Conclusions from the Literature Survey

Some points from the literature survey and conclusions derived that might be useful in this study are provided below:

- Phenomenological in-plane failure criteria such as Larc and Puck provide a better understanding of the whole damage progression process compared to non-phenomenological criteria.
- Most failure criteria are valid for certain loadings and laminates; thus, a criterion suitable for the particular case should be chosen.
- Intralaminar failure criteria were improved usually to simulate better the damage under combined transverse compression and in-plane shear loadings. Thus, utilizing an improved criterion, such as Larc03/04, would yield good results especially for OHC simulation since OHC test induces high compression and shear loads. Hashin's failure criterion would suffice for OHT laminates since it provides good predictions under combined transverse tension and in-plane shear loadings.
- Whereas compression effects in OHT laminates are not prevalent, shear effects are still present. Thus, modeling OHT laminates with in-plane failure criteria that takes into account shear nonlinearity would improve simulation quality.
- There is an agreement in the literature in that in-situ strength of the plies needs to be considered. Ignoring in-situ effect might underestimate the strength of the quasi-isotropic laminates that will be studied in this thesis

since 90° plies are thin (they are not blocked with other 90° plies) and constrained by different-angle plies.

- In studies including cohesive zone modeling, cohesive layers were placed only between plies with different angles; thus, cohesive layers were not utilized between same-angle layers for the laminates with blocked plies.
- Intralaminar and interlaminar stiffness degradation trend is an important factor for numerical stability and computational performance, especially for implicit analyses. Degradation trend suggested by Ridha et al. [48], a zigzagging degradation curve with piecewise constant stiffness, can be a good option if implicit analysis is to be used.



CHAPTER 3

THEORY

3.1. Failure in Composites

Lamina level failure criteria require decomposition of laminate stresses into individual lamina stresses. Thus, it is important to take a closer look at the lamina itself. In the lamina coordinate system, as shown in Figure 3-1, 1-axis is along the fibers, 2-axis is the transverse direction that is perpendicular to fiber direction, 3-axis is along the thickness of the lamina. Laminate's global coordinate system is xyz -coordinate system. z -axis of the global coordinates and 3-axis of the lamina coordinates are coincident. The angle between 1-axis and x -axis is the ply-angle.

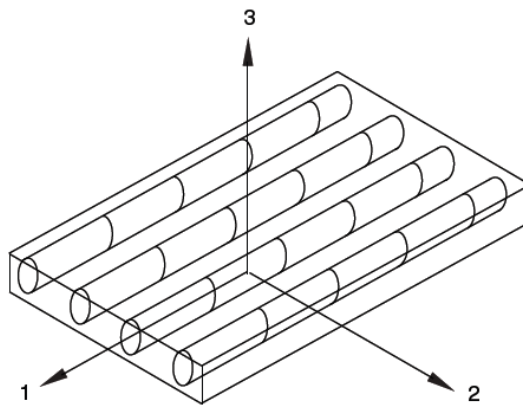


Figure 3-1 Unidirectional lamina [51]

Material behavior in Abaqus® for composites is linearly elastic up to damage initiation. Built-in composite modeling capabilities of Abaqus® therefore do not allow modeling non-linear shear behavior. Four different failure modes are considered in the built in damage initiation criterion of the software. These modes

are fiber rupture resulting due to longitudinal tension, fiber buckling and kinking due to longitudinal compression, matrix cracking due to in-plane shear and transverse tension, and matrix crushing under in-plane shear and transverse compression. These modes are abbreviated as fiber tension, fiber compression, matrix tension, and matrix compression, respectively. Fiber tension failure mode of Hashin's failure criterion [32] presented in Chapter 2 by Eq. (2-2) is a special form of built-in fiber tension failure criterion of the software. According to built-in failure criterion of the software, failure index of fiber tension failure mode is:

$$\left(\frac{\sigma_{11}}{X^T}\right)^2 + \alpha \left(\frac{\tau_{12}}{S^L}\right)^2 = 1 \quad (3-1)$$

where α is a coefficient that controls the effect of in-plane shear on failure in fiber tension mode. In this study, α is taken a "0" assuming that fiber tensile failure is due only to longitudinal tensile stresses. Criteria for other failure modes are the same in Hashin's failure criterion [32] explained in Chapter 2 and built in failure criterion of the software.

σ_{11} , σ_{22} , and τ_{12} in Eq. (3-1), Eq. (2-3) - (2-5) are components of the lamina stress tensor σ that is used to evaluate the damage initiation criteria.

After damage initiation criterion is met at a material point, stiffness matrix of the material point degrades according to the relation

$$\sigma = C_d \varepsilon \quad (3-2)$$

where C_d is the damaged stiffness matrix of the material point and ε is the strain tensor whose components are ε_{11} , ε_{22} , and ε_{12} . C_d is defined as follows :

$$C_d = \frac{1}{D} \begin{bmatrix} (1-d_f)E_1 & (1-d_f)(1-d_m)v_{21}E_1 & 0 \\ (1-d_f)(1-d_m)v_{12}E_2 & (1-d_m)E_2 & 0 \\ 0 & 0 & D(1-d_s)G_{12} \end{bmatrix} \quad (3-3)$$

$$D = 1 - (1-d_f)(1-d_m)v_{12}v_{21}$$

where d_f , d_m , and d_s in Eq. (3-3) are fiber, matrix, and shear damage variables, respectively. These damage variables are determined from the damage variables associated with the four aforementioned damage modes as follows:

$$d_f = \begin{cases} d_f^t & \text{if } \sigma_{11} \geq 0 \\ d_f^c & \text{if } \sigma_{11} < 0 \end{cases}$$

$$d_m = \begin{cases} d_m^t & \text{if } \sigma_{22} \geq 0 \\ d_m^c & \text{if } \sigma_{22} < 0 \end{cases} \quad (3-4)$$

$$d_s = 1 - (1-d_f^t)(1-d_f^c)(1-d_m^t)(1-d_m^c)$$

where d_f^t , d_f^c , d_m^t , and d_m^c are fiber tensile, fiber compression, matrix tensile, and matrix compression damage variables, respectively.

In progressive failure analysis of a displacement-controlled test, displacement is incrementally applied. For stiffness degradation, damage variables that are dependent on displacement are determined at every increment and then inserted in Eq. (3-3).

Before expressing damage variables in terms of displacements, it should be mentioned that built-in constitutive model of the software for degradation is expressed in terms of effective stress and effective displacement for each of the four failure modes. Equivalent stress at a material point decreases linearly with increasing equivalent displacement as in Figure 3-2 according to the damage evolution model.

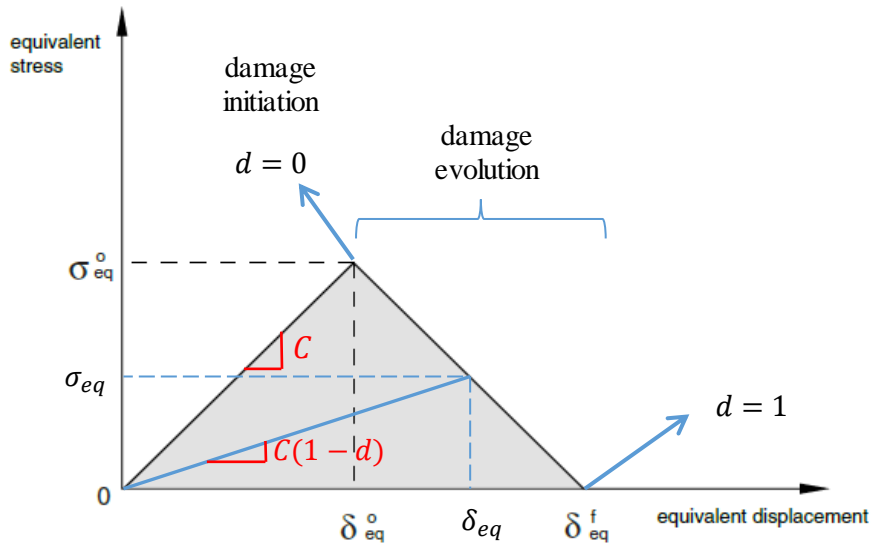


Figure 3-2 Linear damage evolution (adapted from [51])

The notation used in Figure 3-2 is as follows:

σ_{eq} : Equivalent stress at a point on the graph during damage evolution

δ_{eq} : Equivalent displacement at a point on the graph during damage evolution

σ_{eq}^0 : Equivalent stress at damage initiation

δ_{eq}^0 : Equivalent displacement at damage initiation

δ_{eq}^f : Equivalent displacement at point of complete damage

C : Undamaged stiffness of the material point

d : Damage variable

According to the linear damage evolution presented in Figure 3-2, undamaged stiffness of the material point indicated by C is constant up to the point of damage initiation. At damage initiation, damage variable d is 0, and it will gradually increase to 1 as the damage evolves and stiffness of the material point is totally degraded to zero. Taking advantage of similarity of triangles in Figure 3-2, damage variable d is determined as a function of equivalent displacement:

$$d = \frac{\delta_{eq}^f (\delta_{eq} - \delta_{eq}^0)}{\delta_{eq} (\delta_{eq}^f - \delta_{eq}^0)} \quad (3-5)$$

Change of d with equivalent displacement is shown in Figure 3-3 to illustrate better the concept of damage variable.

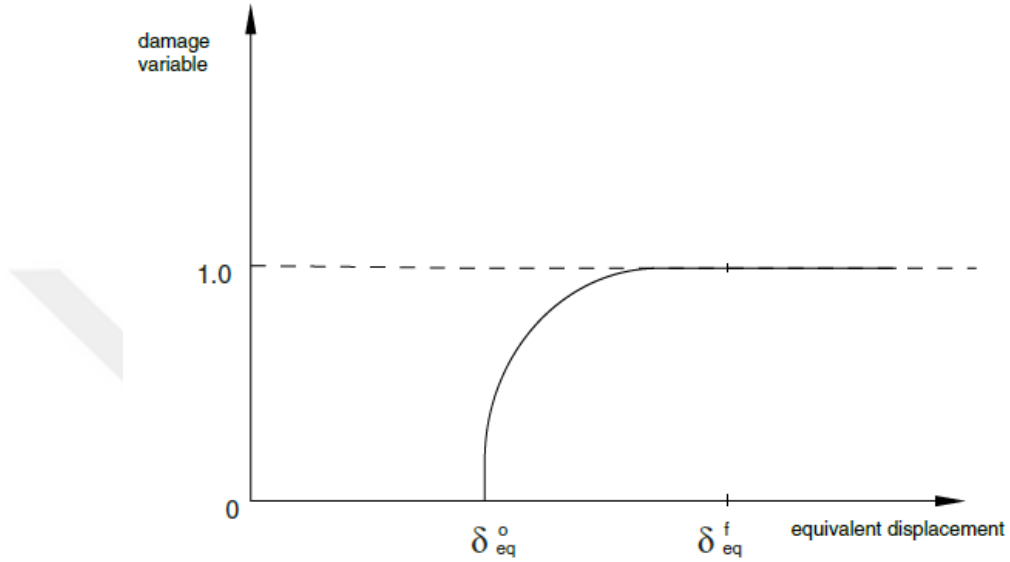


Figure 3-3 Change of damage variable with equivalent displacement [51]

Damage evolution for all failure modes are as shown in Figure 3-2; however, every failure mode has different expression for the equivalent stress and equivalent displacement as follows [51]:

Fiber tension ($\sigma_{11} \geq 0$):

$$\delta_{eq}^{ft} = L^c \sqrt{\langle \varepsilon_{11} \rangle^2 + \alpha \varepsilon_{12}^2} \quad (3-6)$$

$$\sigma_{eq}^{ft} = \frac{\langle \sigma_{11} \rangle \langle \varepsilon_{11} \rangle + \alpha \tau_{12} \varepsilon_{12}}{\delta_{eq}^{ft} / L^c} \quad (3-7)$$

Fiber compression ($\sigma_{11} < 0$):

$$\delta_{eq}^{fc} = L^c \langle -\varepsilon_{11} \rangle \quad (3-8)$$

$$\sigma_{eq}^{fc} = \frac{\langle -\sigma_{11} \rangle \langle -\varepsilon_{11} \rangle}{\delta_{eq}^{fc} / L^c} \quad (3-9)$$

Matrix tension ($\sigma_{22} \geq 0$):

$$\delta_{eq}^{mt} = L^c \sqrt{\langle \varepsilon_{22} \rangle^2 + \varepsilon_{12}^2} \quad (3-10)$$

$$\sigma_{eq}^{mt} = \frac{\langle \sigma_{22} \rangle \langle \varepsilon_{22} \rangle + \tau_{12} \varepsilon_{12}}{\delta_{eq}^{mt} / L^c} \quad (3-11)$$

Matrix compression ($\sigma_{22} < 0$):

$$\delta_{eq}^{mc} = L^c \sqrt{\langle -\varepsilon_{22} \rangle^2 + \varepsilon_{12}^2} \quad (3-12)$$

$$\sigma_{eq}^{mt} = \frac{\langle -\sigma_{22} \rangle \langle -\varepsilon_{22} \rangle + \tau_{12} \varepsilon_{12}}{\delta_{eq}^{mc} / L^c} \quad (3-13)$$

Eq. (3-6) – (3-13) depend on the equivalent length, L^c , which is a parameter related to dimensions and type of the element the material point belongs to. For a real number a , Macaulay bracket operator is defined as $\langle a \rangle = (a + |a|)/2$.

Damage evolution model of the software is based on fracture energy. For damage evolution to occur, user needs to input fracture energies dissipated in different failure modes. Fracture energy of a failure mode is equal to the area under equivalent stress vs. equivalent displacement curve of the failure mode. Once the fracture energy is input, the software calculates δ_{eq}^f of the particular failure mode to construct equivalent stress vs. equivalent displacement curve of the failure mode and the damage evolution takes place according to the graph constructed. In

this study, fracture energies are calculated assuming that total degradation takes place at an equivalent displacement that is 10% higher than the equivalent displacement at damage initiation. The details about calculation of the fracture energies are provided in Chapter 5.

3.2. Cohesive Zone Model

CZM assumes that there is a transition region between the bulk material on the crack front and the crack tip where the stresses decrease gradually to zero from a maximum value attained in the bulk material. The basis for this approach is that there are crazes, fibrils or micro cracks, depending on the kind of material and loading, that connect two surfaces of the crack. In polymers, a craze zone forms on the crack tip due to polymer fibrils connecting the surfaces of the crack as shown in Figure 3-4 [52].

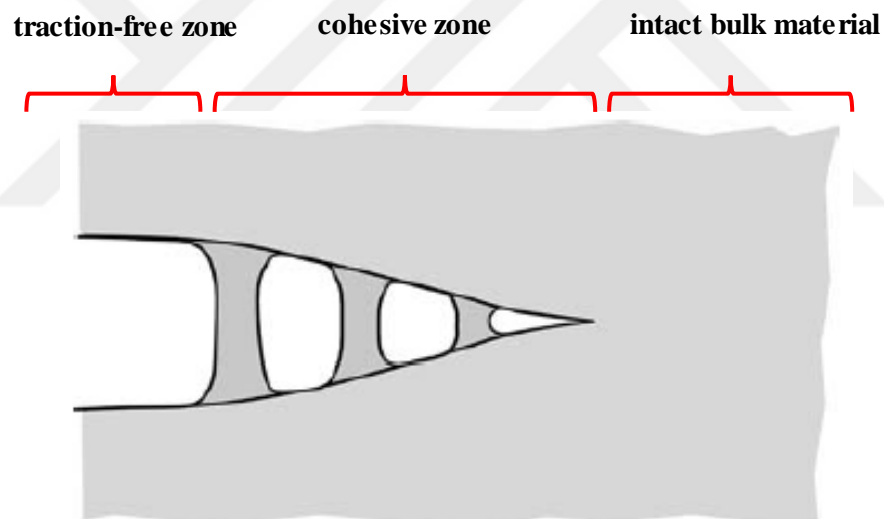


Figure 3-4 Craze zone at the crack tip in polymers (Adapted from [52])

Fibers may form a bridge between the surfaces of the crack in fiber-reinforced polymer composites. These fiber bridges form a resistance for the crack growth as they need to be broken before crack continues to propagate. Fiber bridging phenomenon is observed especially in Double Cantilever Beam (DCB) test as illustrated in Figure 3-5. Fiber bridging is sometimes considered to create a

cohesive zone obeying traction-separation law, while Sun and Jin [53] state that fiber bridging should be treated separately since its failure mechanism is different than that of a regular cohesive zone.

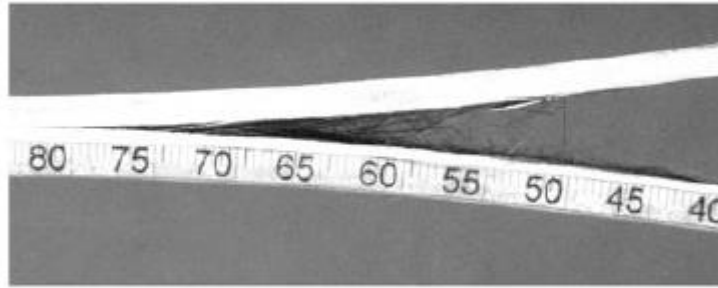


Figure 3-5 Fiber bridging in DCB test of a unidirectional composite laminate [54]

As another example of cohesive zone, formation of micro cracks at crack tip is observed when a crack in brittle matrix laminate is loaded in shear. Micro cracks coalesce and matrix material between the micro cracks vanish and bear no more stress as the traction increases as shown in Figure 3-6.

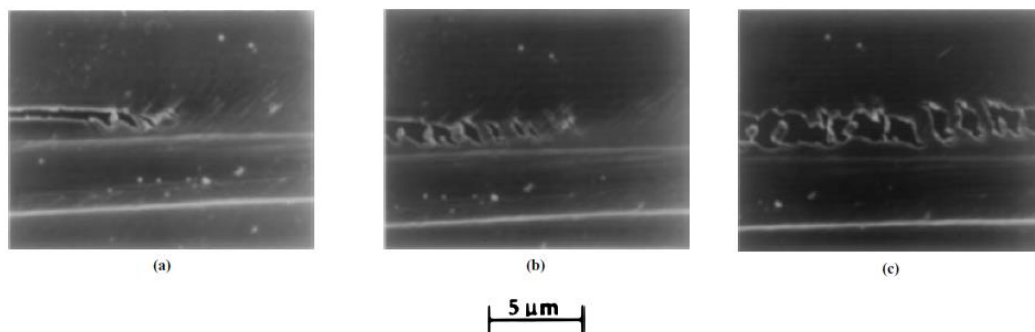


Figure 3-6 Micro crack coalescence in Mode-II delamination experiment [52]

Delamination in laminated composites is simulated by placing zero-thickness cohesive elements between the plies. Zero-thickness is a term used to mention that thickness of cohesive layer is too small compared to thickness of adjacent plies in order not to affect the stiffness of the laminate. Constitutive relation of cohesive elements includes two stages called as damage initiation and damage evolution. Up to damage initiation, traction in the material point in the cohesive region increases linearly with increasing displacement. When damage initiates, traction at

the material point starts to decrease; in other words, damage starts to evolve. Trend of damage evolution can be in many forms. Linear and exponential degradation trends as shown in Figure 3-7 are common in the literature; however, shape of the degradation curve can be adjusted to eliminate numerical instabilities as long as area under traction-separation curve is equal to fracture energy [48]. In this study, linear damage evolution will be used thanks to its simplicity. As the displacement increases further, traction at the material point totally vanishes at some displacement, which means that crack has propagated and passed by the material point. Since traction-separation up to failure is already linear, the constitutive relation is called “bilinear cohesive law” when linear damage evolution is utilized. Examples of bilinear and linear-exponential traction-separation response in mode-I loading are illustrated in Figure 3-7.

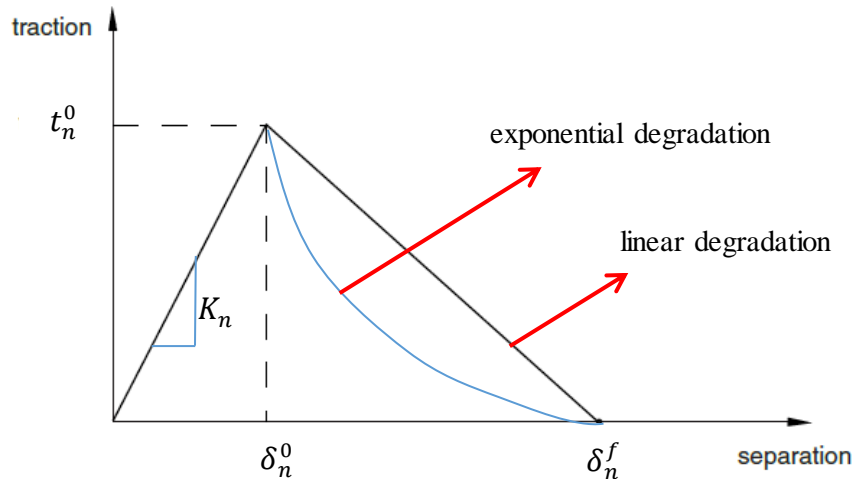


Figure 3-7 Bilinear and linear-exponential traction-separation response in normal crack opening mode (Adapted from [51])

t_n^0 , δ_s^0 , and δ_t^f denote traction at damage initiation, displacement (separation) at damage initiation, and displacement at total failure, respectively, where the subscript n stands for “normal” direction. Traction-separation behavior will be similar for the first and the second shear directions, for which the corresponding subscripts are s and t , respectively. Direction n is along the thickness of the cohesive layer, s is along the second local direction (y direction, for example, in xyz coordinate system) and t is along the third local direction. K_n is called as the

“penalty stiffness” in normal direction, which is the stiffness of the interface up to damage initiation. K_t and K_s are penalty stiffnesses in s and t directions. K_n , K_s , and K_t are selected based on material properties of laminates and adjacent ply thicknesses, the selection process will be explained in Chapter 5. t_n^0 , t_s^0 , and t_t^0 are interface properties called nominal interface strengths. In this study, t_n^0 is assumed to be equal to transverse tensile strength of the lamina. Likewise, t_s^0 and t_t^0 were assumed to be equal to corresponding nominal shear strengths. Knowing K and t^0 , δ^0 can be obtained for the three crack opening modes as follows:

$$\begin{aligned}\delta_n^0 &= \frac{t_n^0}{K_n} \\ \delta_s^0 &= \frac{t_s^0}{K_s} \\ \delta_t^0 &= \frac{t_t^0}{K_t}\end{aligned}\tag{3-14}$$

Damage initiation in CZM is a strength of materials based approach in which damage initiation can be detected by stresses (tractions) or strains at the interface. Common delamination initiation criteria for CZM are maximum stress, maximum strain, quadratic stress and quadratic strain criteria. Maximum stress and strain criteria are similar to their in-plane failure criteria correspondents; they assume failure when one of the interface stress or strain components exceeds the stress or strain allowable value, which is the interface property. However, quadratic criteria assume a quadratic interaction among stresses or strains in the interface for initiation of damage initiation [51]. Quadratic nominal stress and strain criteria are utilized more commonly in the literature compared to maximum stress/strain criteria since they take interaction of different modes into account. Therefore, quadratic stress criterion is used in this study and it can be expressed as follows:

$$\left(\frac{\langle t_n \rangle}{t_n^0}\right)^2 + \left(\frac{t_s}{t_s^0}\right)^2 + \left(\frac{t_t}{t_t^0}\right)^2 = 1\tag{3-15}$$

where terms in nominators are nominal stresses. Macaulay bracket ($\langle \rangle$) is used to indicate that compressive nominal stress does not have any effect in damage initiation.

There remains only one unknown, which is δ_n^f , in single mode bilinear response shown. In order to understand how δ_n^f is determined by the software, damage evolution in CZM should be discussed. Damage evolution in CZM is based on fracture mechanics such that fracture energy related with a crack propagation mode equals the area under the equivalent stress vs. equivalent displacement curve [51]. This equality follows from Griffith's theory of fracture [22]. This equality can be expressed as follows:

$$\begin{aligned}
 G_{Ic} &= \int_0^{\delta_n^f} t_n d\delta_n \\
 G_{IIc} &= \int_0^{\delta_s^f} t_s d\delta_s \\
 G_{IIIc} &= \int_0^{\delta_t^f} t_t d\delta_t
 \end{aligned} \tag{3-16}$$

Before ending the discussion with single-mode cohesive behavior, going through Figure 3-8 will help in clarifying the subject better. Figure 3-8 [27] illustrates crack propagation in DCB using cohesive elements along the pre-existing crack. When a load below the critical load is applied, only element 1 is damaged, although not completely. Therefore, crack does not start to propagate at this instant. However, when the load is increased to P_{crit} , element 1 is damaged totally by losing its stiffness. Thus, crack propagates a distance of length of element 1 at P_{crit} .

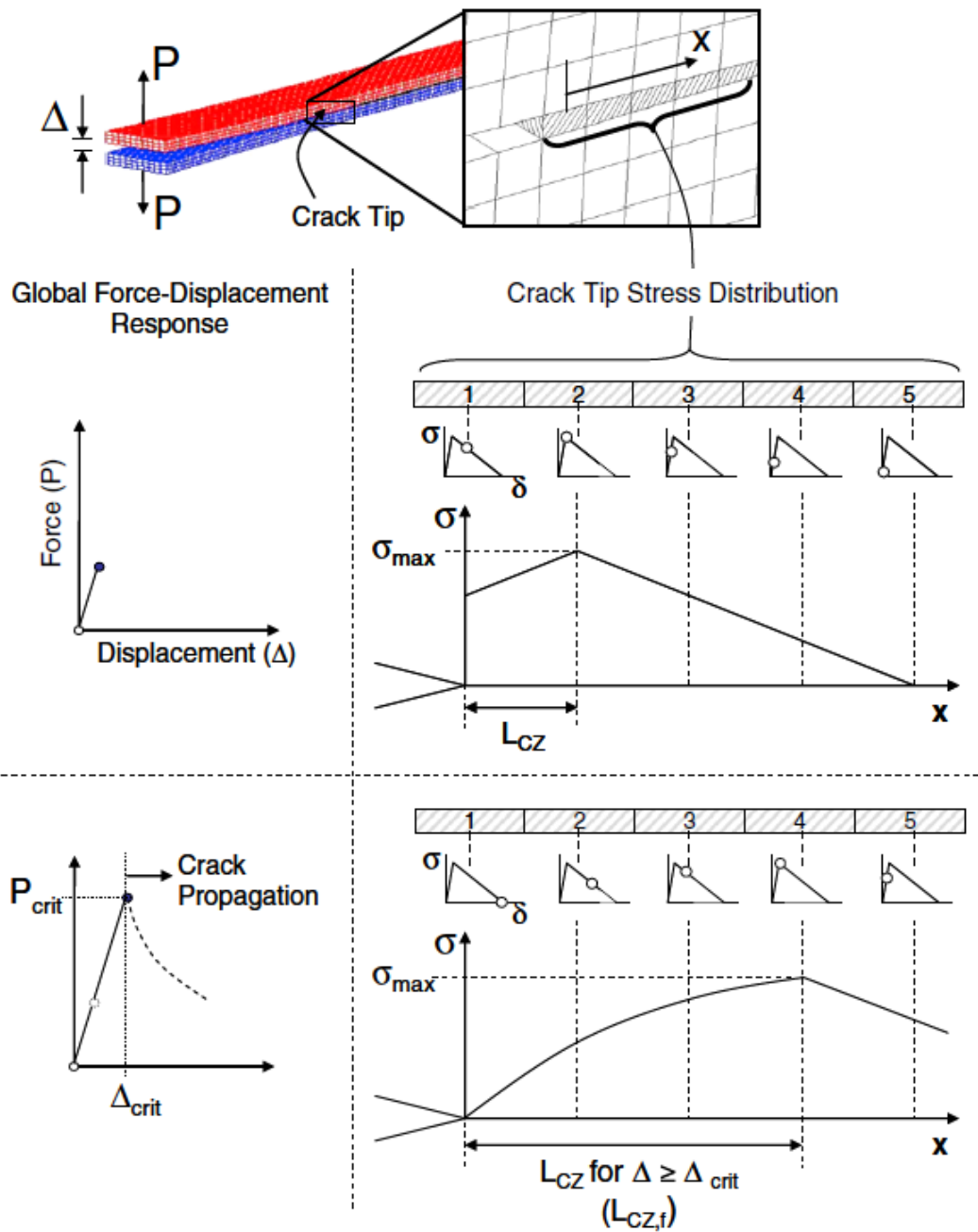


Figure 3-8 Development of numerical cohesive zone (L_{cz} denotes the length of cohesive zone) [27]

In service loading conditions, interfaces of laminates are usually subjected to mixed-mode loadings, which cause cracks to develop under mixed-mode conditions. Therefore, while determining critical fracture energy for damage evolution, mode-mixture should be taken into account. Mode mixture is

percentage of individual loading modes in total loading. Common methods utilized to establish dependence of fracture energy on the mode-mixture are Power law and Benzeggagh-Kenane (BK) criterion. Power law assumes that interaction of fracture energies of different modes is related by a power that is specific to the material system. BK fracture criterion [55] employs a similar approach and yields better results when critical energies during deformation purely along the first and second shear directions are the same [51]. Power law and BK fracture criterion are defined as follows:

Power Law:

$$\left(\frac{G_n}{G_n^c}\right)^\alpha + \left(\frac{G_s}{G_s^c}\right)^\alpha + \left(\frac{G_t}{G_t^c}\right)^\alpha = 1 \quad (3-17)$$

BK fracture criterion:

$$G_n^c + (G_s^c - G_n^c) \left(\frac{G_s}{G_T}\right)^\eta = G^c \quad (3-18)$$

where

$$\begin{aligned} G_s &= G_s + G_t \\ G_T &= G_n + G_s \end{aligned} \quad (3-19)$$

Critical fracture energies in Eq. (3-17) and (3-18) denoted by superscript c are lamina properties and determined by fracture experiments. G_n^c is determined by DCB test [56], and G_s^c is determined by End Notch Fracture (ENF) test [57]. Mode-III fracture toughness data for laminated composites is quite rare in the literature; thus, G_t^c is usually considered to be equal to G_s^c .

In the Mixed Mode Bending (MMB) test [58], a unidirectional laminate with a pre-existing crack is loaded such that both mode-I and mode-II crack propagation stresses exist at the crack. MMB test is run at different mode-mix ratios so that dependence of total critical fracture energy on mode-mixture can be obtained. Once critical total fracture energy vs. mode mixture graph is obtained by conducting MMB test at different mode-mixtures, η and α in Eq. (3-17) and (3-

18) can be determined curve-fitting. An example of curve-fitting for MMB specimens made of AS4/3501-6 is provided in Figure 3-9. It is seen that BK criterion with $\eta = 1.45$ is the best fit for the experimental data among the fit options shown.

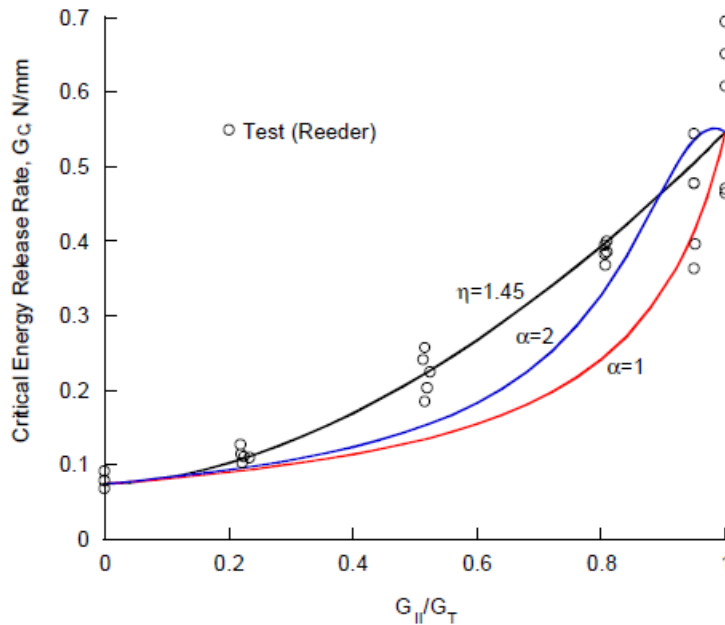


Figure 3-9 Curve fit to critical energy release rate vs. mode mixture data [59]

Although Mixed-Mode Bending (MMB) test was conducted for S2 glass/epoxy, which is one of the material systems used in the study, experimental mixed-mode fracture toughness values were not used to determine the curve-fitting parameter (the exponent η in BK criterion). In the MMB test, fracture toughness of the specimen at several mode-mixtures are measured to determine the change in fracture toughness with mode-mixture. The extremes of the mode mixture are Mode-I and Mode-II loading cases. The fracture toughness values measured at mode mixtures other than the extremes will be between the fracture toughness of Mode-I and Mode-II loading cases. Since Mode-I and Mode-II fracture toughness values for S2 glass/epoxy were close to each other, the trend of the curve determining change of fracture toughness with mode mixture was assumed to be

linear, which means setting $\eta = 1$ in BK criterion. Dependence of critical energy release rate on mode mixture for S2 glass/epoxy is shown in Figure 3-10.

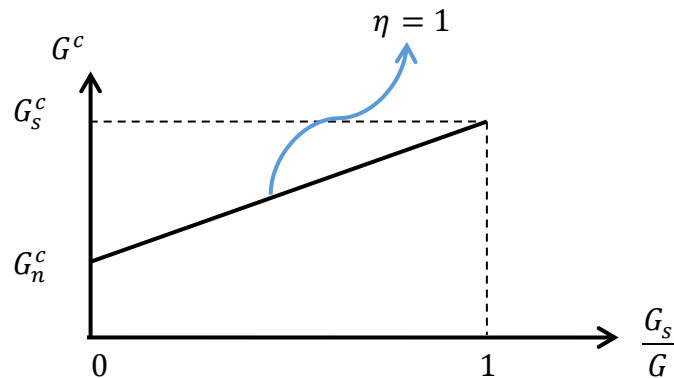


Figure 3-10 Critical energy release rate vs. mode mixture for S2 glass/epoxy

Combining shear response in s and t directions under shear mode, mixed-mode response of the cohesive elements is illustrated in Figure 3-11. Response under pure shear and normal loading is shown by triangles on the sides of the prism. Dotted curve on the top is the locus of points for which damage initiation criterion is satisfied according to quadratic nominal stress criterion. Dotted curve on the bottom represents points exposed to full damage. Each vertical triangle with corners on the locus of damage initiation, locus of full damage and the origin represents traction separation response under mixed mode conditions with different mode mixtures.

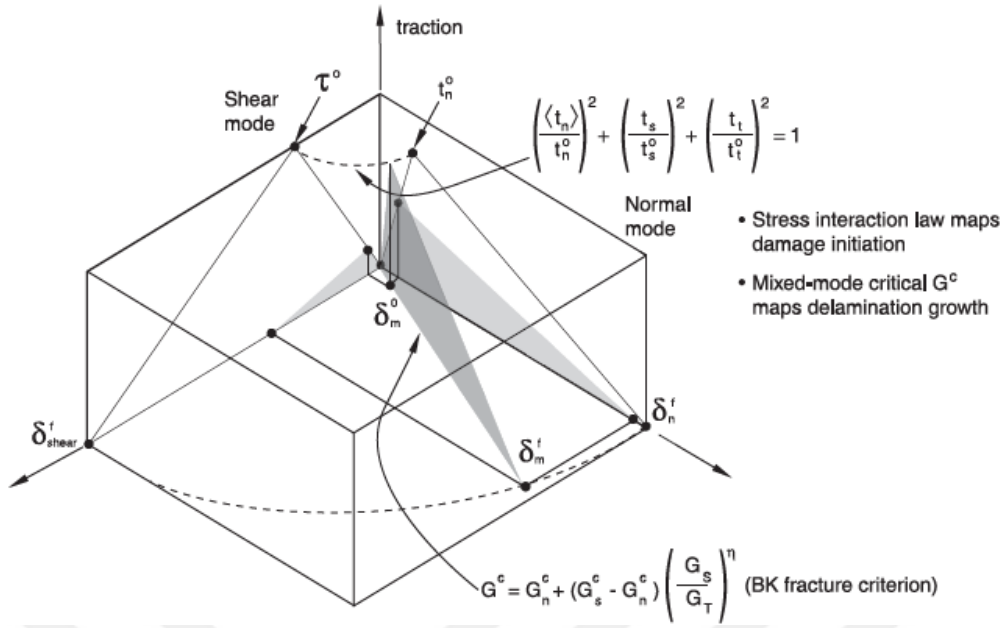


Figure 3-11 Mixed-mode response of cohesive elements [51]

Mixed mode separation (δ_m) and interface stiffness in combined shear loading (τ^0) shown in Figure 3-11 are expressed as follows:

$$\delta_m = \sqrt{\langle \delta_n \rangle^2 + \delta_s^2 + \delta_t^2} \quad (3-20)$$

$$\tau^0 = \sqrt{(t_s^0)^2 + (t_t^0)^2} \quad (3-21)$$

Linear damage evolution in CZM is governed by evolution of a damage variable D as in the case of damage evolution of intra-laminar damage. Stiffness of the interface decreases with increasing damage parameter according to the relation:

$$K_d = K(1 - D) \quad (3-22)$$

where

$$D = \frac{\delta_m^f (\delta_m^{max} - \delta_m^0)}{\delta_m^{max} (\delta_m^f - \delta_m^0)} \quad (3-23)$$

The term δ_m^{max} in Eq. (3-23) refers to the maximum effective displacement in the loading history. δ_m^0 and δ_m^f are defined as effective separations at damage initiation and total failure, respectively. Eq. (3-23) is obtained by assuming constant mode-mixture during loading history of the cohesive zone [51].

As a last note, G_n^c , G_s^c , and G_t^c obtained from DCB, ENF, and MMB tests in this study have been determined by testing unidirectional laminates, as in the standards [56] [57] [58]. However, it has been observed that fracture toughness of the interfaces where the adjacent plies are unidirectional are less than fracture toughness of the interfaces with multidirectional adjacent plies [60]. ASTM Standard for ENF Test [57] also states that the toughness values obtained by testing unidirectional laminates may not represent the actual toughness values that will be used for delamination growth. However, experimental data about fracture toughness for interfaces of multidirectional laminates are quite limited in the literature. The studies presented in Chapter 2 all utilized toughness values obtained from unidirectional laminate testing. It should be noted that using a lower fracture toughness value to simulate delamination is a conservative approach. This is because unidirectional laminates yield the lowest fracture toughness values, the area of the traction-separation curve will be low, which means that cohesive zone will experience full damage at a lower separation value.



CHAPTER 4

BENCHMARK TESTS

4.1. Introduction

A finite element methodology is suggested in Chapter 5 to characterize damage in composite laminates with holes. In order to validate this method, tension tests of three different quasi-isotropic open-hole coupons are chosen for benchmarking. Each of the coupons chosen exhibit one of the different failure patterns, namely brittle, delamination and pull-out failure as explained in the experimental study conducted by Green et al. [13]. Open-hole tension test results of coupons exhibiting brittle and delamination failure were chosen from the experimental study conducted by Green et. al [13]. The coupon exhibiting pull-out failure was tested in Mechanical Engineering Department of METU as part of the SANTEZ project “Design Methodology for Advanced Thick Composites”.

4.2. Benchmark Coupons

Top view of benchmark coupons is shown in Figure 4-1, where w , l , and d denote width, length of the gage section, and hole diameter, respectively. In-plane dimensions of the coupons are different for every specimen along with the material, lay-up and thickness (t).

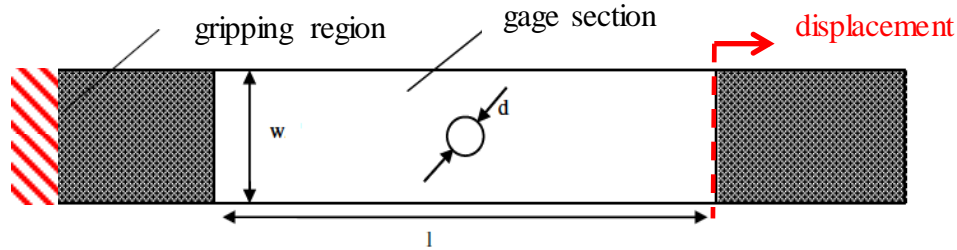


Figure 4-1 Coupon geometry (Adapted from [61])

All coupons were subjected to displacement-controlled loading along the length direction as indicated by an arrow in Figure 4-1. An extensometer was not utilized in the experimental study conducted by Green et al. [13]. Instead, the displacement of the grips of the tensile test machine was recorded. Therefore, the load-displacement curves obtained by FEA in Chapter 6 were not superimposed on the experimental load-displacement curves of the laminates exhibiting brittle and delamination failure since the displacement data may include the compliance of the tensile test machine. Extensometer was placed on the laminate exhibiting pull-out failure such that the center of the hole is in the middle of the gage section whose length is 75 mm . The laminates from the experimental study conducted by Green et al. [13] has width-to-diameter ratio of 5, and length-to-diameter ratio of 20, while the laminate exhibiting pull-out failure has width-to-diameter ratio of 5, as specified by the ASTM Standard Test Method for Open-Hole Tensile Strength of Polymer Matrix Composite Laminates [4]. Grip length of the laminate exhibiting pull-out failure is 60 mm , whereas grip lengths of the laminates exhibiting brittle and delamination failure were not specified in the experimental study conducted by Green et al. [12]. Dimensions, materials, lay-up, and ultimate load carried by the specimens are provided in Table 4-1.

Table 4-1 Benchmark coupons where the coupons exhibiting brittle and delamination failure are taken from [12] and the laminate exhibiting pull-out failure is tested in scope of the thesis

	Brittle (Laminate1)	Delamination (Laminate 2)	Pull-out (Laminate 3)
Lay-up	[45/90/-45/0] _{4S}	[45 ₄ /90 ₄ /-45 ₄ /0 ₄] _S	[45/0/-45/90] _{2S}
Material	IM7/8552 Carbon/Epoxy	IM7/8552 Carbon/Epoxy	S2/MTM49L S2 glass/Epoxy
<i>l</i> (mm)	254	63.5	160
<i>w</i> (mm)	63.5	15.88	38
<i>d</i> (mm)	12.7	3.175	6.35
<i>t</i> (mm)	4	4	3.75
Ultimate Load (kN)	95.00	17.46	48.70
Coefficient of Variation	%1.01	%5.56	%2.22
Loading Rate (mm/min)	2	0.5	2

4.2.1. Coupon Exhibiting Brittle Failure

Brittle failure experienced by the laminate with lay-up [45/90/-45/0]_{4S} is dominated by fiber failure in 0°, 45°, and -45° layers with little split in off-axis plies, little delamination around the hole and matrix cracking in 90° layers. As shown in Figure 4-2, load-displacement curve of the specimen is linear until the ultimate load and load drops instantaneous to zero after ultimate load and it is evident from the fracture surface of the laminate that all the off-axis plies except 90° experienced fiber failure.

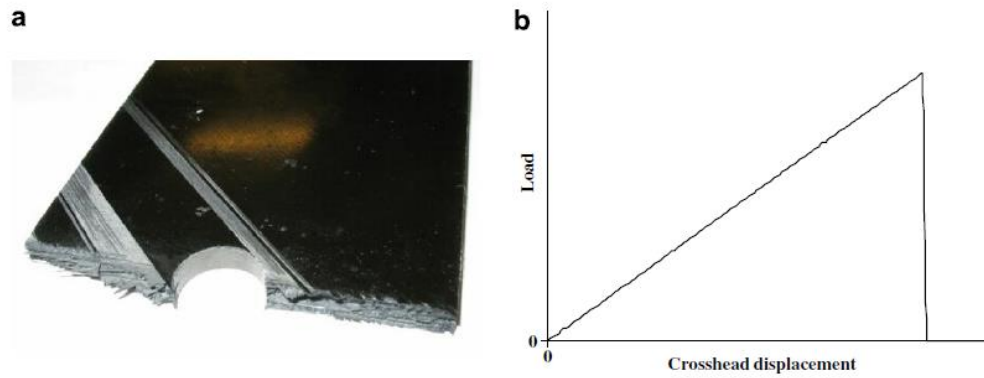


Figure 4-2 (a) Fracture surface of the laminate (b) Load-displacement curve of the laminate [13]

4.2.2. Coupon Exhibiting Delamination Failure

Delamination failure experienced by the laminate with lay-up $[45_4/90_4/-45_4/0_4]_S$ is dominated by extensive delamination at $-45^\circ/0^\circ$ interface, delamination at other interfaces and splits in off-axis plies as shown in Figure 1-4. Load-displacement curve of the laminate has two load drop regions. First load drop region has two load drops due to progressive delamination growth as shown in Figure 4-3 and the second load drop region is simply a single load drop due to fiber failure. Note that the second load drop region is not depicted in the figure. First load drop takes place following the delamination growth at $-45^\circ/0^\circ$ interfaces. As a result of the delamination, 0° layers split longitudinally where split lines are tangential to the hole. Splits and delaminated $-45^\circ/0^\circ$ interfaces can be observed in Figure 4-4 that shows x-ray image of the laminate after the first load drop. ZnI_2 was applied to the specimen before taking its x-ray image in order to increase the density of the regions with intralaminar and delamination damage so that those regions would seem darker in the x-ray image. When the x-ray image is combined with the picture of the free edge, it can be deduced that the blurred regions in the x-ray image correspond to delamination at $-45^\circ/0^\circ$ interfaces. Although the picture of the free edge in Figure 4-4 does not show the full length of the laminate, it is stated in the study conducted by Green et al. [12] that the delamination at $-45^\circ/0^\circ$ interfaces extend towards the grips more than shown in the picture. It is seen in Figure 4-4 that asymmetric delamination covers only half of the hole

vicinity. Delamination of the other half of the interface results in another load drop. After this second load drop, regions of the laminate between the splits and free edges continue to carry load, leading to increase in load. Once 0° layers also fail, load drops to zero. Ultimate load in this specimen was taken to be the first load drop since delamination at $-45^\circ/0^\circ$ interface causes laminate to lose its integrity after the first load drop.

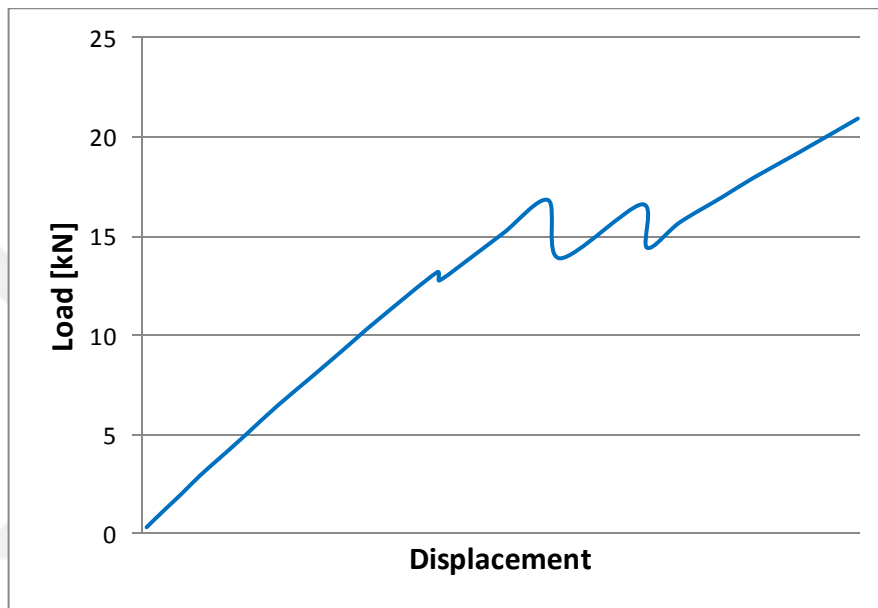


Figure 4-3 Load-displacement curve of the laminate exhibiting delamination failure

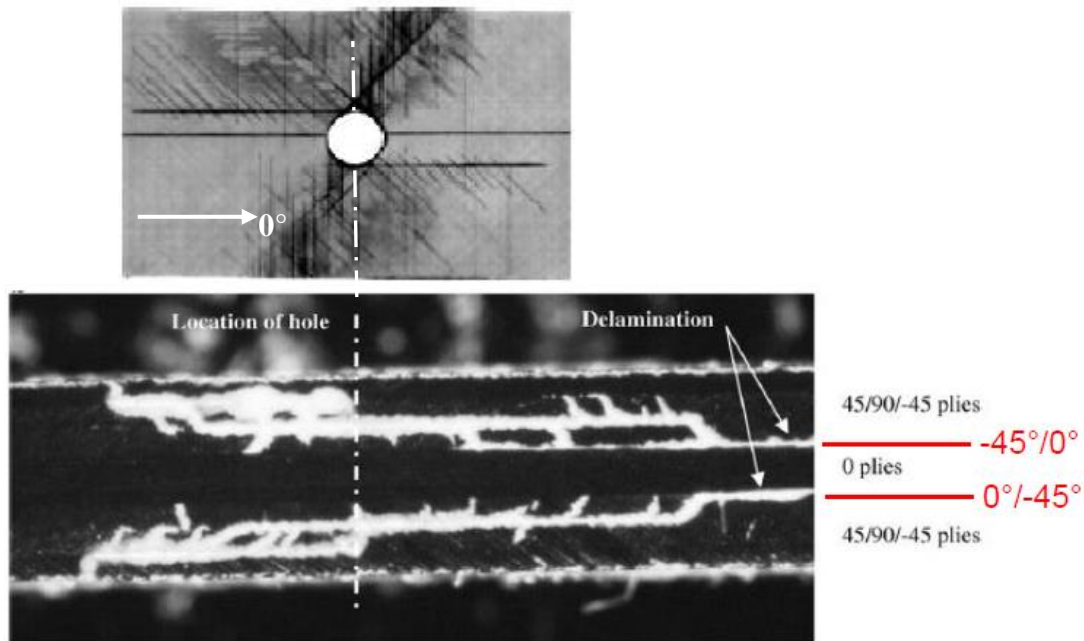


Figure 4-4 (top) X-ray image after the first load drop (bottom) picture of the free edge with dye penetrant applied after the first load drop (Adapted from [12])

4.2.3. Coupon Exhibiting Pull-out Failure

Pull-out failure experienced by the laminate with lay-up $[45/0/-45/90]_{2S}$ is dominated by fiber failure in 0° plies, matrix failure in off-axis plies and moderate delamination at interfaces around the hole. Unlike delamination failure, there is a single load drop in the pull-out failure. Delamination is limited to the vicinity of the hole in regions away from free edges, although the delamination at free edges extend towards the grips. Although this type of failure was defined for specimens made of IM7/8552 carbon/epoxy in the experimental study conducted by Green et al. [13], the term “pull-out failure” was used also for the failure pattern of the laminate made of S2 glass/MTM49L since the failure patterns observed in both cases were similar with insignificant differences. One of the differences between pull-out failure observed in the test of laminate made of S2 glass/MTM49L with lay-up $[45_4/90_4/-45_4/0_4]_S$ and the experimental study conducted by Green et al. [13] is that delamination does not extend up to grips at free edges in the study of Green et al. [13].

Tensile testing of the specimens with lay-up $[45/0/-45/90]_{2S}$ was carried out according to ASTM D5766/D5766M, which is “Standard Test Method for Open-Hole Tensile Strength of Polymer Matrix Composite Laminates” [4]. In order to investigate damage progression during the tension test, light was pointed on the specimens as shown in Figure 4-5, taking advantage of their translucency.

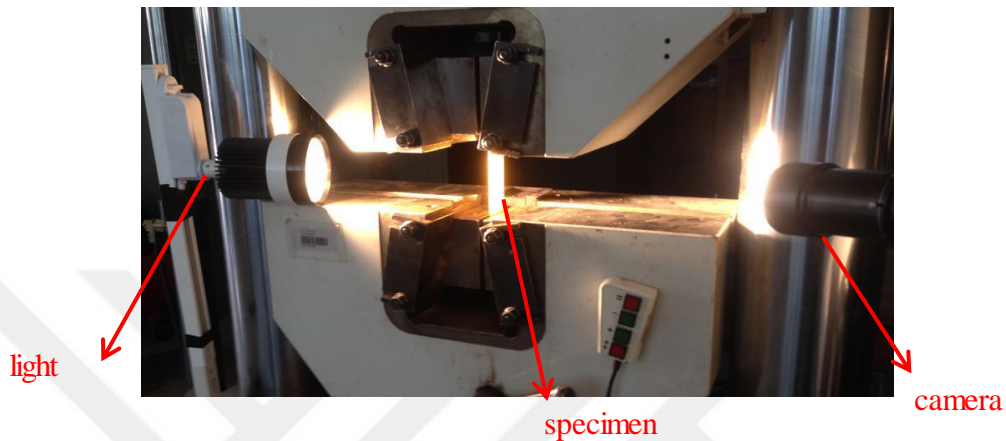


Figure 4-5 Orientation of the light, specimen, and camera for open-hole tension test of the laminate exhibiting pull-out failure

Damaged regions seemed darker under the light due to reflection of the light back from the newly formed surfaces, which was useful for tracking damage progression. Figure 4-6 shows damage states at four load levels. Note that black color at the bottom-left region of the hole in the Figure 4-6-a is paint and therefore it is not an indicator of any kind of damage. It is observed in the Figure 4-6-a that there are no split lines in the off-axis plies and delamination at interfaces at 67% ultimate load. Split lines in the off-axis plies indicating matrix failure can be observed at 90% ultimate load. When the load increases to 98% ultimate load, delamination starts to grow around the hole. It is thought that black delamination region at 98% ultimate load is a result of fiber failure at 0° plies, leading to delamination at the adjacent interfaces. As the load increases further, delamination area grows as in Figure 4-6-d and the load drops instantaneously to zero just after the ultimate load as in the Figure 4-7 which contains typical load-displacement curve and the image of the specimen after failure. Examination of the specimen

after failure showed that all the 45° , -45° and 90° layers failed by matrix failure and all the 0° layers failed by fiber failure.

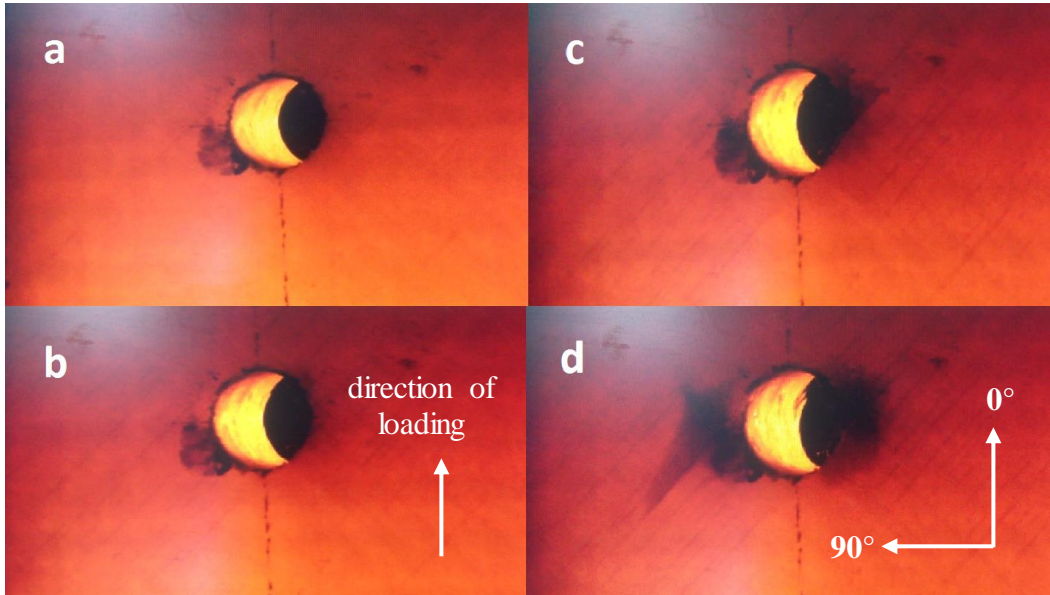


Figure 4-6 Damage state at (a) 67% (b) 90% (c) 98% (d) 99.7% of the ultimate load

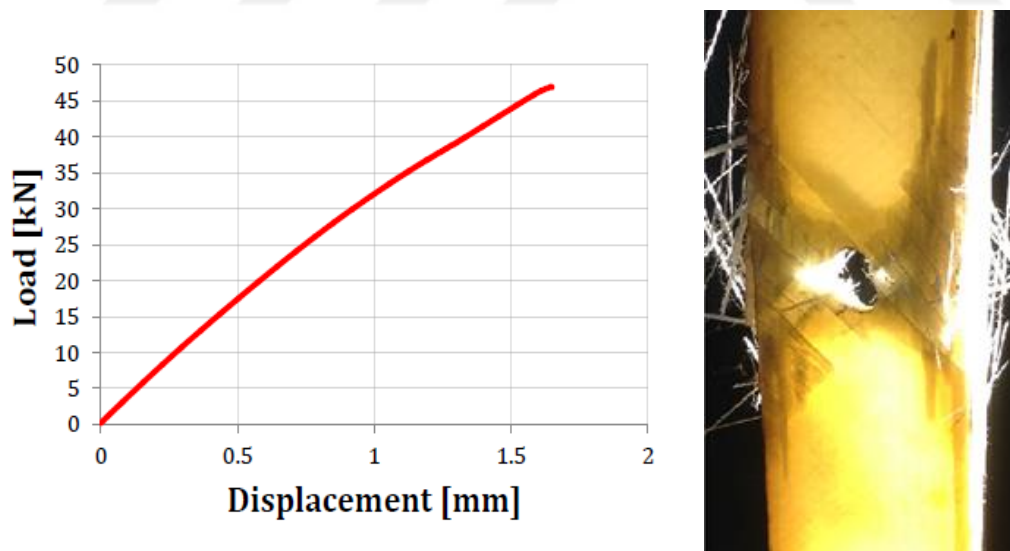


Figure 4-7 (left) Typical load-displacement curve (right) laminate after failure

CHAPTER 5

FINITE ELEMENT ANALYSIS

The aim of this chapter is to explain and suggest finite element analysis strategies to simulate the progressive failure in open-hole tension laminates. Software utilized for the analyses is Abaqus®. First, a brief discussion of the numerical methods and analysis techniques inherent in the software is presented. Then, finite element model is discussed by describing every step of the modeling process and emphasizing modeling strategies that are critical for the specific case of progressive failure analysis of open-hole tension laminates.

5.1. Finite Element Method

Analyses in structural mechanics are either linear or non-linear. In linear analyses, there is a linear relationship between the load applied and the response of the system and the stiffness of the system does not change as the load is applied. For instance, the simple tension analysis of a tensile test specimen made of steel is linear up to the yield point. If the load applied on the specimen is doubled, elongation of the specimen is also doubled since the stiffness of the specimen, in this case the modulus of elasticity, is constant. In non-linear analyses, however, relation between the load applied and the response of the system is not linear anymore. In other words, stiffness of the system is a function of displacement in this case. Stiffness of the system may change due to several factors such as material, boundary, and geometry-related non-linearities [51]. Material non-linearity is due to the material's own non-linear stress-strain behavior. The progressive failure analysis of composites includes extensive material non-linearities. This is because the stiffness of material points needs to be decreased according to a damage evolution law after the damage initiation takes place.

Figure 4-4 and Figure 4-7 show non-linear load-displacement curves of the benchmark coupons that exhibit delamination and pull-out type of failures, respectively. Boundary non-linearity is the change in boundary conditions as the load is applied and geometric non-linearity is present when the magnitude of deflections affect the stiffness of the structure by causing change in the geometry.

There are two common methods to deal with non-linear structural analyses, namely implicit and explicit finite element methods. In the implicit method, state at time $t + \Delta t$ is solved based on states at times t and $t + \Delta t$. Since the solution of the next step ($t + \Delta t$) requires iterations to be made utilizing the state at $t + \Delta t$, the method is called implicit. In this method, total load is applied incrementally and each increment requires many iterations to obtain the state at $t + \Delta t$. Every iteration requires linear equation $u = K^{-1}F$ to be solved for every integration point, where K , F , and u denote stiffness, net force, and displacement at a node, respectively. Therefore, inverse of global stiffness matrix needs to be found for every increment, making this procedure costly.

It is suggested to utilize explicit procedure when the analysis includes material degradation and failure since implicit method faces severe convergence difficulties in these cases [51]. In the explicit procedure, the state at $t + \Delta t$ is solved by utilizing the known state variables at t . Thus, since the next state is based on a known state, the procedure is called “explicit”. Explicit method does not use iterations to obtain the solution for the next state, which make computations affordable. The software utilizes central difference method to integrate equations of motion in time. According to the dynamic equilibrium, nodal accelerations (\ddot{u}) times the nodal mass matrix (M) is equal to the net nodal forces, where net nodal forces are obtained by subtracting internal forces (I) from the external forces (P) at the nodes.

$$M\ddot{u} = P - I \quad (5-1)$$

$$\ddot{u}_{(t)} = M^{-1}(P_{(t)} - I_{(t)}) \quad (5-2)$$

where subscripts denote the times at which variables are calculated. Nodal velocities at $t + \Delta t/2$ are calculated as follows:

$$\dot{u}_{(t+\frac{\Delta t}{2})} = \dot{u}_{(t-\frac{\Delta t}{2})} + \left(\frac{\Delta t_{(t+\Delta t)} + \Delta t_{(t)}}{2}\right)\ddot{u}_{(t)} \quad (5-3)$$

Nodal velocities at $t + \Delta t/2$ are used to calculate nodal displacements at $t + \Delta t$:

$$u_{(t+\Delta t)} = u_{(t)} + \Delta t_{(t+\Delta t)}\dot{u}_{(t+\frac{\Delta t}{2})} \quad (5-4)$$

Once displacements are obtained as shown above, strain increments are calculated. Stresses are then calculated with the help of constitutive equations and nodal internal forces (I) at $t + \Delta t$ are found. Since the external load at $t + \Delta t$ is already known, the process above is repeated for the following increments [51]. In this procedure, the damage check is performed once the stresses are calculated at material points. If the intralaminar failure criterion is satisfied at a material point, stiffness of that material point is degraded according to the damage evolution law.

Since the analyses include both composite and cohesive layers that have damage evolution laws associated with them, the progressive failure analyses of the laminates are quite non-linear. This leads to severe convergence problems in implicit analyses; therefore, the explicit method is utilized in this study for all specimen types.

5.2. Description of the Model

Taking advantage of symmetry, half of the laminates are modeled in the thickness direction. However, symmetry about other planes (yz -plane and xz -plane) was not considered since it would imply discontinuity in fiber direction for 45° and -45° plies at symmetry planes. Although modeling strategy is similar for all three types of laminates, some differences still exist. Unless it is mentioned that the procedure applied is specific to one type of laminate, it should be understood that the procedure is valid for all types of laminates.

The laminates are partitioned both in longitudinal and transverse directions as shown in Figure 5-1 to have a symmetric mesh orientation around the hole as displayed in Figure 5-2. Grip regions shown in Figure 4-1 are not included in the analysis, instead, one end of the laminate is fixed and displacement was applied to the other end. Boundary conditions applied at the fixed end ($x = 0$) are shown in Figure 5-3, where U_i and R_i denote displacements along and rotations about x , y , and z axes. One of the nodes at the other end ($x = l$) is chosen as the load node and the displacement is directly applied to the load node. All the other nodes at $x = l$ are connected to the load node by an “equation constraint” so that all the nodes at $x = l$ move at the same time when the load node moves due to applied displacement.

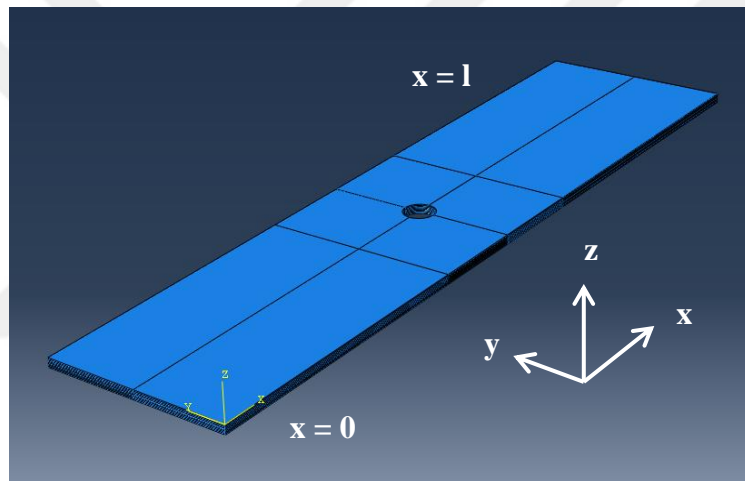


Figure 5-1 Isometric view of Laminate 3

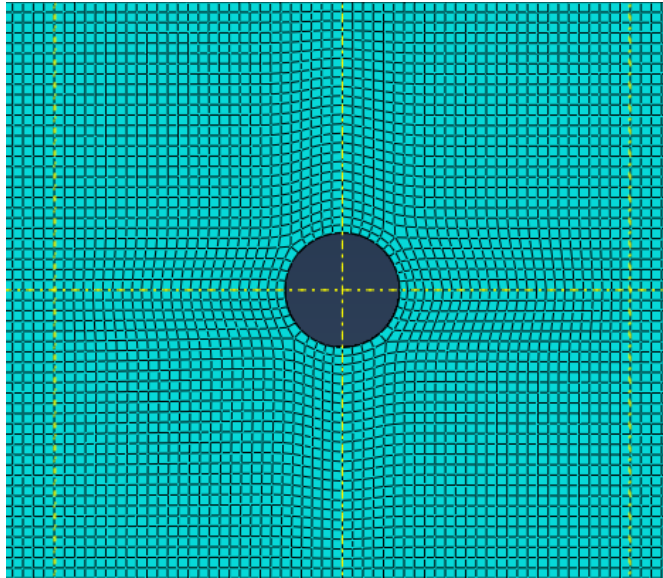


Figure 5-2 Mesh pattern around the hole

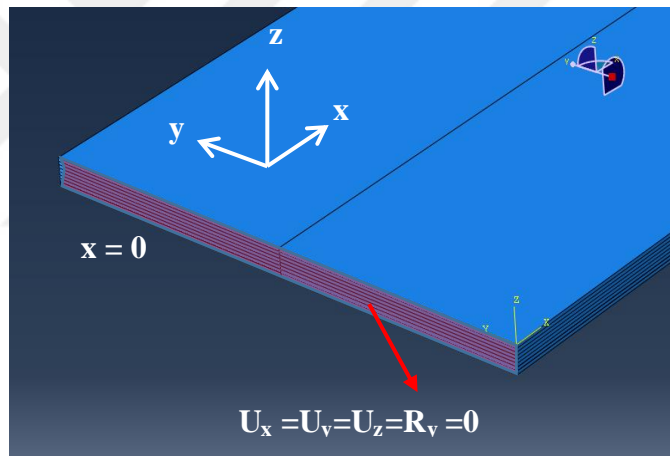


Figure 5-3 Boundary conditions at $x = 0$

In the explicit solver of the software, an energy balance criterion needs to be satisfied in order to get dependable simulation results. The explicit solver is usually used for high-speed dynamic problems; however, highly non-linear quasi-static problems and problems including materials with degradation and failure can also be simulated with the explicit solver if the energy criterion is satisfied. In order for the explicit analysis to yield appropriate results for such cases, kinetic energy of the model should be a small fraction (5%-10%) of the strain energy of

the system [51]. Therefore, the total displacement is applied in a time interval that ensures that dynamic effects are negligible for all laminates. Figure 5-4 shows the variation of kinetic and strain energy values in Laminate 3 as the load increases where the kinetic energy is much lower than the strain energy. The other laminates are observed to have similar energy curves.

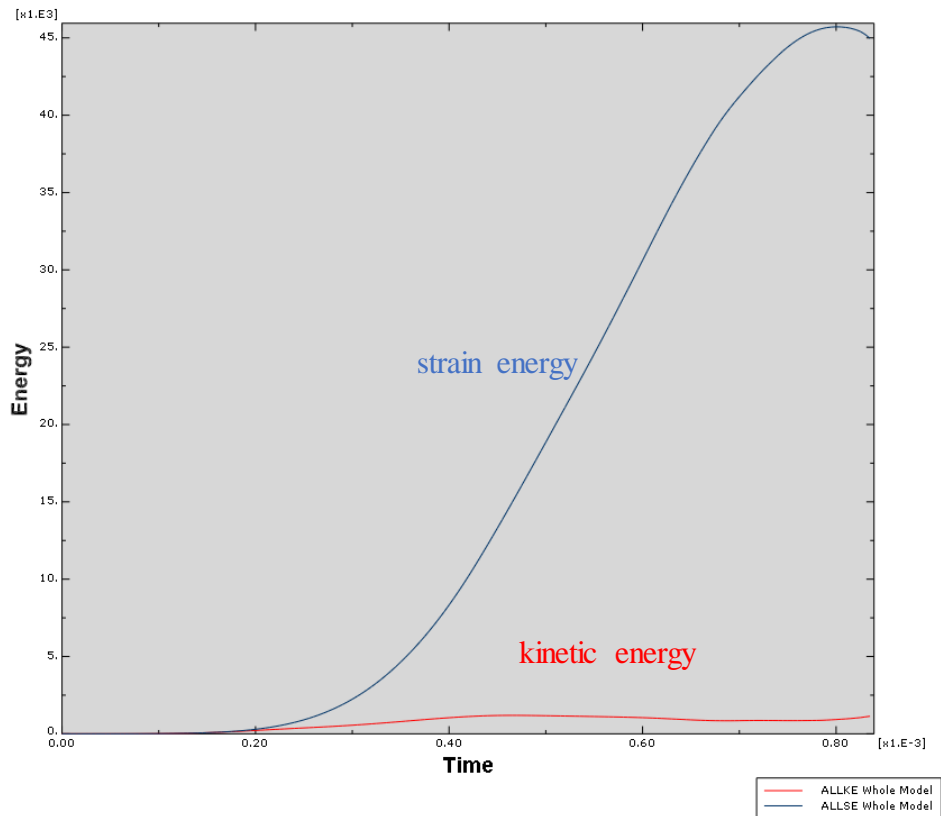


Figure 5-4 Kinetic and strain energy change with time for laminate 3

The laminates are also partitioned in thickness direction in order to simulate delamination by inserting cohesive layers between plies. In the model of Laminate 3, cohesive layers are inserted between every two consecutive plies. Noting that there are more interfaces in laminate 1 than in laminate 3, finite element analysis of Laminate 1 becomes too complicated when cohesive layers are placed at every interface, which causes analysis to last too long and even the solution to diverge. This problem is overcome by inserting cohesive layers to the interfaces with the highest possibility of delamination. Interlaminar stresses causing delamination are

high when there is mismatch of Poisson's ratios and extension-shear coupling coefficients in neighboring plies; therefore, determining the variation of Poisson's ratio and extension-shear coupling coefficient with respect to ply angle is important in determining interfaces with the highest possibility of delamination. Equations for change of Poisson's ratio and extension-shear coupling coefficient with fiber angle, which are dependent on elastic constants of the lamina, are provided below [62]:

$$v_{xy} = E_x \left[\frac{\nu_{12}}{E_{11}} (\sin^4 \theta + \cos^4 \theta) - \left[\frac{1}{E_{11}} + \frac{1}{E_{22}} - \frac{1}{G_{12}} \right] \sin^2 \theta \cos^2 \theta \right] \quad (5-5)$$

$$m_x = E_x \left[\left[\frac{2}{E_{11}} + \frac{2\nu_{12}}{E_{11}} - \frac{1}{G_{12}} \right] \sin \theta \cos^3 \theta - \left[\frac{2}{E_{22}} + \frac{2\nu_{12}}{E_{11}} - \frac{1}{G_{12}} \right] \sin^3 \theta \cos \theta \right] \quad (5-6)$$

where

$$\frac{1}{E_x} = \frac{1}{E_{11}} \cos^4 \theta + \left(\frac{1}{G_{12}} - \frac{2\nu_{12}}{E_{11}} \right) \sin^2 \theta \cos^2 \theta + \frac{1}{E_{22}} \sin^4 \theta \quad (5-7)$$

In Eq. (5-5) – (5-7) v_{xy} denotes the Poisson's ratio, m_x denotes the extension-shear coupling, and E_x denotes the Young's modulus in x direction for a lamina loaded in non-principal $x - y$ coordinates. Inserting material data of IM7/8552 into the equations, the change of Poisson's ratio and extension-shear coupling coefficient with fiber angle are plotted in Figure 5-5 and Figure 5-6 for an individual lamina made of IM7/8552 carbon/epoxy.

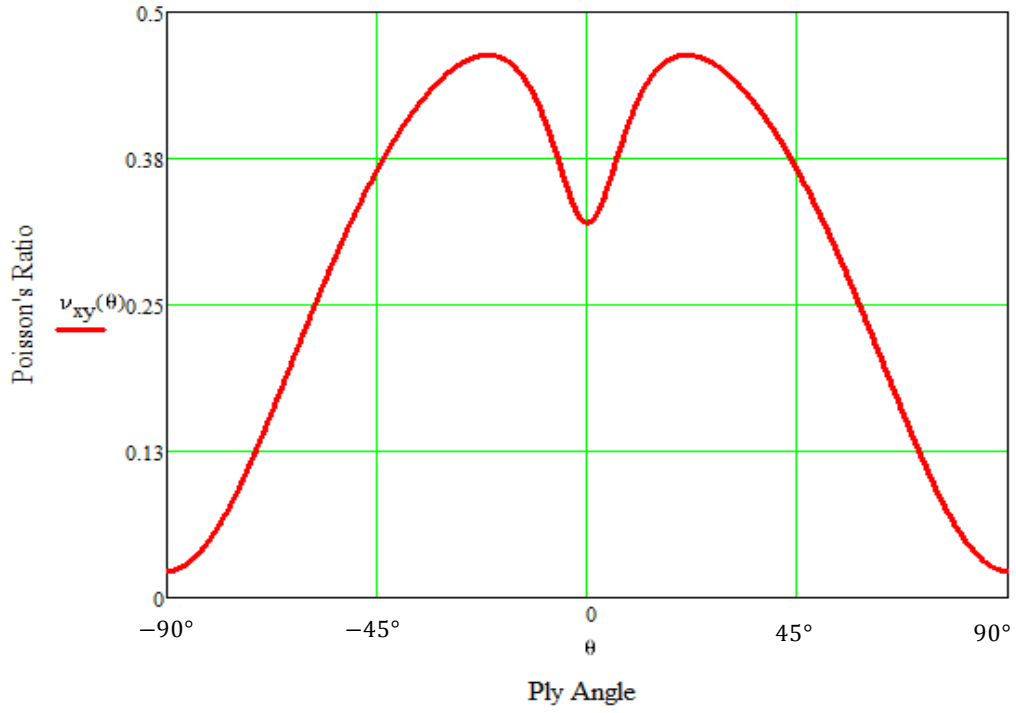


Figure 5-5 Change of Poisson's ratio with fiber angle for a lamina made of IM7/8552

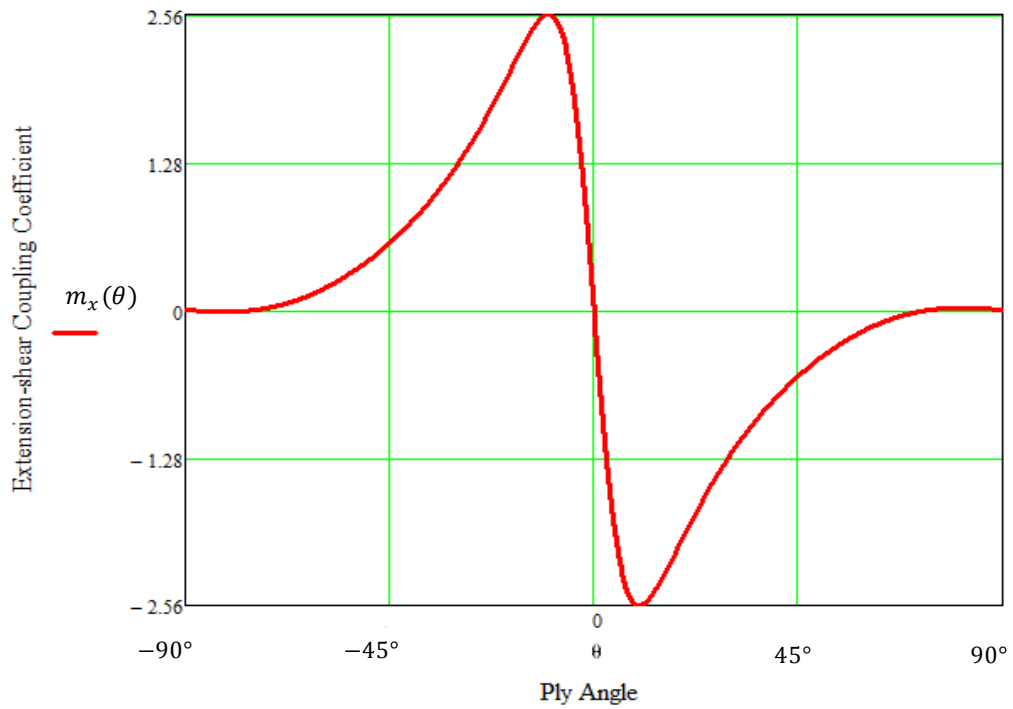


Figure 5-6 Change of extension-shear coupling coefficient with fiber angle for a lamina made of IM7/8552

It can be observed in Figure 5-5 and Figure 5-6 that the difference in both Poisson's ratios and extension-shear coupling coefficients are largest for $45^\circ/90^\circ$ and $-45^\circ/90^\circ$ interfaces. Therefore, laminate 1 is modeled such that cohesive layers are inserted only at $45^\circ/90^\circ$ and $-45^\circ/90^\circ$ interfaces.

Laminate 2 is a ply-level scaled laminate, meaning that it has same-angle ply clusters. In this case, interfaces between the plies with the same fiber angle do not experience mismatch of Poisson's ratio and the extension-shear coupling coefficient. Thus, for the model of laminate 2, cohesive layers are placed at interfaces where neighboring plies have different fiber angles, i.e., between the same-angle ply clusters. Through-the-thickness details of the laminates can be seen in Figure 5-7.

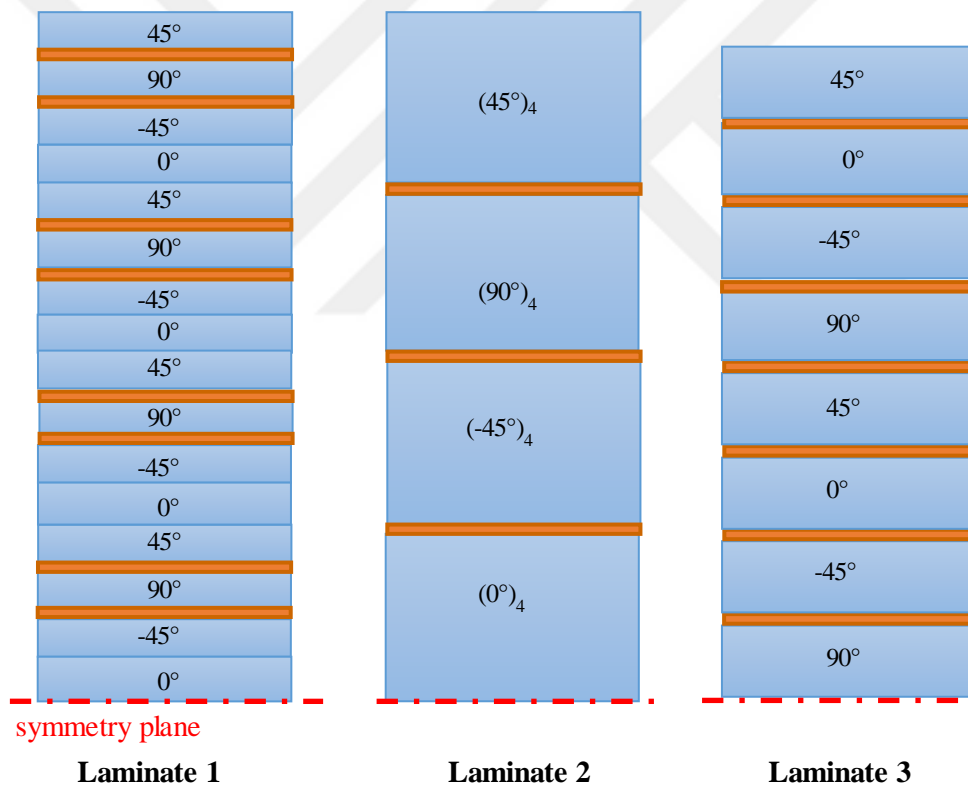


Figure 5-7 Through-the-thickness layup of the laminates where orange cohesive layers are in orange color

5.2.1. Elements used in analyses

In the software, layered composites can be modeled by conventional shell elements, continuum shell elements or solid elements. Conventional shell elements do not have geometric thickness, but the thickness is defined as a section property. Continuum shells, however, have geometric thickness like solid elements. They look like solid elements although their kinematic and constitutive behavior is similar to conventional shells [51]. The user interface does not have a built-in capability to implement composite damage initiation and damage evolution criteria for solid elements. If solid elements are utilized, subroutines need to be written in order to implement the criteria. For this study, conventional shell elements are utilized for composite layers. The reasons for choosing continuum shell elements over conventional shell and solid elements are that they have a better through-the-thickness discretization compared to conventional shell elements and they can be used with built-in Hashin's failure criterion. Moreover, it is stated in the user manual [51] that solid elements do not usually provide a more accurate solution than conventional shell elements, which also serves as a reason for choosing continuum shell for the analyses.

First order SC8R continuum shell element is used for composite layers. SC8R is an 8-node, hexagonal, first-order interpolation element with reduced integration. It has only displacement degrees of freedom at its nodes. A general view of a tetragonal continuum shell is provided in Figure 5-8. SC8R continuum shell elements used have three integration points that are located at the top, middle and bottom of the element in the thickness direction as shown in Figure 5-9. However, the number of through-the-thickness integration points was increased to five for ply-blocked laminates to better discretize the thickness. Only one element is placed per ply or same angle ply-block in the thickness direction. The Simpson's Rule is used for through-the-thickness integration.

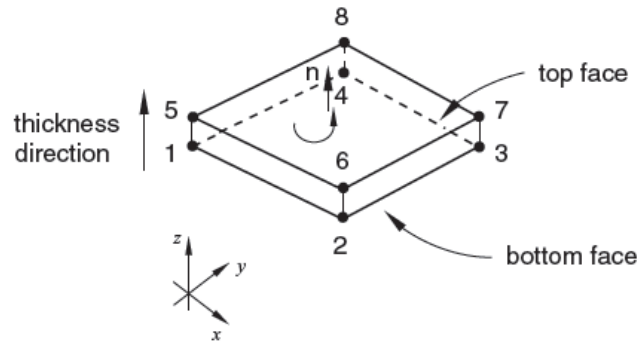


Figure 5-8 8-node continuum shell element [51]

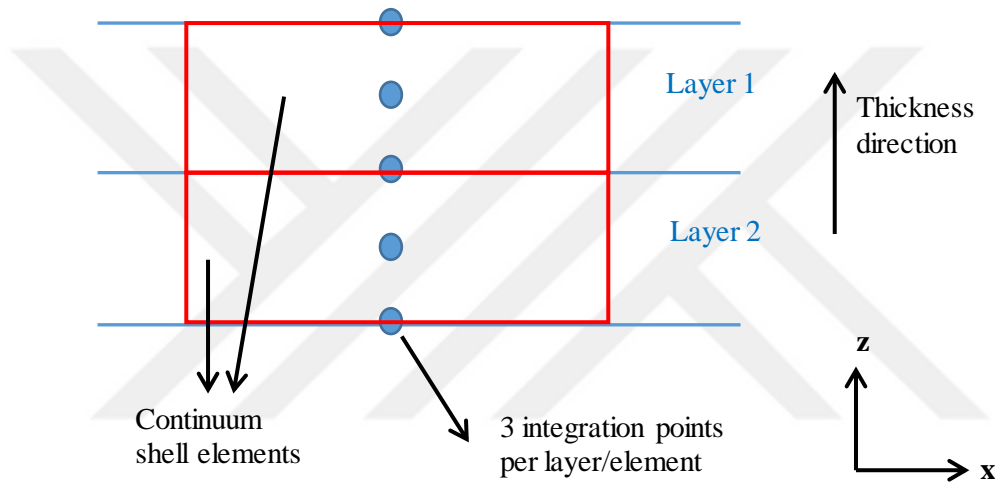


Figure 5-9 Integration points in the thickness direction of the laminate without ply-blocking (cohesive layer is not shown)

For the cohesive layers, 8-node COH3D8 elements are used. These elements look similar to the element shown in Figure 5-8. Cohesive elements share nodes with the adjacent composite layers; so a constraint between composite and cohesive layers is not needed. Cohesive layers are modeled with one element in the thickness direction. Cohesive layer thickness is 0.001 mm for all laminates so that the cohesive layers do not affect the overall elastic modulus of the laminate. Since the cohesive elements and continuum shell elements share nodes, the mesh pattern is the same for both composite and cohesive layers. The in-plane mesh size of the

models is determined by the constraints on element minimum cohesive zone length to simulate delamination.

5.2.2. Material Properties

Material properties of S2 glass/epoxy are obtained by coupon tests conducted at Mechanical Engineering Department of METU in scope of the SANTEZ project called “Design Methodology for Advanced Thick Composite Structures”. I participated in Double Cantilever Beam (DCB), End Notch Flexure (ENF) and Mixed-Mode Bending (MMB) tests conducted in scope of the project. Tests were conducted according to ASTM and EN standards. The tests conducted and the properties obtained from the corresponding tests are provided in Table 5-1. Material properties of the two materials used are provided in Table 5-2.

Table 5-1 Lamina level coupon tests and properties measured

Test	Properties Measured
Longitudinal Tension Test	Longitudinal modulus of elasticity, longitudinal tensile strength, Poisson’s ratio
Longitudinal Compression Test	Longitudinal compressive strength
Transverse Tension Test	Transverse modulus of elasticity, transverse tensile strength
Transverse Compression Test	Transverse compressive strength
In-plane Shear Test	In-plane shear strength
Double Cantilever Beam Test	Mode-I fracture toughness
End Notch Flexure Test	Mode-II fracture toughness
Mixed-Mode Bending Test	Mixed-mode fracture toughness

Table 5-2 Material properties [13,63,64]

	IM7/8552	S2 Glass/MTM49L
E_{11} [GPa]	161	48.6
E_{22} [GPa]	11.4	10.3
G_{12} [GPa]	5.17	3.96
X_T [MPa]	2326	1764
X_C [MPa]	1200	1046
Y_T [MPa]	60	53
Y_C [MPa]	275	187
S_L [MPa]	90	90.2
ν_{12}	0.32	0.29
G_{Ic} [N/mm]	0.224	0.3
G_{IIc} [N/mm]	0.911	0.47
α, η	1	1

It was shown that tensile and in-plane shear strengths of a unidirectional lamina increase when the lamina is constrained by plies with different angles, which is called “in-situ” effect [65]. In-situ strength of a lamina changes with respect to thickness of the lamina and its position in the laminate. Constrained plies have higher in-situ strengths than unconstrained plies regardless of their thickness and position. Outer plies that are constrained from only one surface have lower in-situ strengths compared to embedded plies constrained from two surfaces. The formulae suggested for prediction of in-situ strengths is provided in Eq. (5-8) – (5-13) [33,65]. The formulae assume that fiber angles of neighboring plies do not affect the in-situ strength, for simplicity.

Thin inner ply:

$$Y_T^{is} = \sqrt{\frac{8G_{Ic}}{\pi t \Lambda_{22}^0}} \quad (5-8)$$

$$S_L^{is} = \sqrt{\frac{8G_{IIc} G_{12}}{\pi t}} \quad (5-9)$$

Thin outer ply:

$$Y_T^{is} = 1.79 \sqrt{\frac{G_{Ic}}{\pi t \Lambda_{22}^0}} \quad (5-10)$$

$$S_L^{is} = 2 \sqrt{\frac{G_{IIc} G_{12}}{\pi t}} \quad (5-11)$$

Thick inner ply:

$$Y_T^{is} = 1.12\sqrt{2}Y_T \quad (5-12)$$

$$S_L^{is} = \sqrt{2}S_L \quad (5-13)$$

where

$$\Lambda_{22}^0 = 2 \left(\frac{1}{E_{22}} - \frac{\nu_{21}^2}{E_{11}} \right) \quad (5-14)$$

The superscript “*is*” is used as an abbreviation for “in-situ”. Formulae for thin plies are utilized for single plies, while formulae for thick plies are used for stacked ply-blocks in the finite element models. In-situ transverse tensile strengths for Laminates 1 and 3 are calculated using Eq. (5-8) and Eq. (5-10). Camanho et al. [65] showed that in-situ shear strength predictions with a linear shear behavior is far greater than the in-situ shear strength prediction with a non-linear shear behavior for very thin plies. Therefore, the in-situ shear strengths for Laminate 1 and the in-situ shear strength of inner plies of Laminate 3 are taken to be equal to in-situ shear strengths of thick plies to be on the safe side. In-situ strengths for

Laminate 2 are taken from [42]. In-situ strengths utilized in the study are provided in Table 5-3.

Table 5-3 In-situ strengths

	$Y_T^{is} [MPa]$		$S_L^{is} [MPa]$	
	inner ply	outer ply	inner ply	outer ply
Laminate 1	161.3	102	114.5	92.7
Laminate 2	98.7	81.7	114.5	92.7
Laminate 3	132.3	83.7	127	102.6

5.2.3. Cohesive Layer Parameters

Proper selection of cohesive layer parameters is important in order to model delamination accurately. The parameters that are to be determined are the interface stiffness, cohesive zone length, element size and interface strength. Interface stiffness (K) is determined ensuring that effective elastic modulus of the laminate composed of cohesive and composite layers does not deviate considerably from original Young's modulus of the composite. K can be determined by the following equation:

$$K = \frac{\alpha E_3}{t} \quad (5-15)$$

where E_3 is the Young's modulus in thickness direction, t is the sublaminar or ply thickness. It has been shown that loss of stiffness due to presence of cohesive layers is below 2% when $\alpha \geq 50$ [66]. α is chosen as 50 in this study. In the calculation of interface stiffness, t was taken as the thickness of one ply for Laminate 1 and Laminate 3, and as the sublaminar thickness of four plies for Laminate 2. Stiffness of the interface in shear directions is assumed to be equal to stiffness in thickness direction.

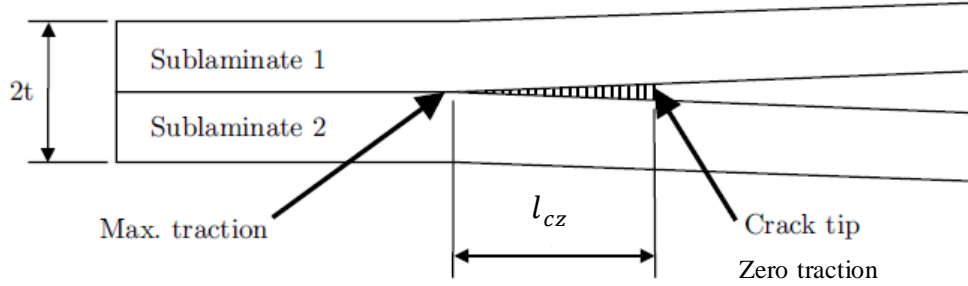


Figure 5-10 Cohesive zone length (Adapted from [66])

One of the most critical properties is the cohesive zone length since it directly affects the number of elements, thus, the element size in the mesh. Cohesive zone length is the distance from the cohesive crack tip where tractions are zero to the geometric crack tip where the tractions are maximum as shown in Figure 5-10. Turon et al. [66] state that cohesive zone length is a material and structural property. The equations proposed to predict cohesive zone length (l_{cz}) have the form:

$$l_{cz} = ME \frac{G_c}{(\tau_0)^2} \quad (5-16)$$

where E is the Young's modulus of the interface in the thickness direction, G_c is the fracture toughness, τ_0 is the strength of the interface, and M is a parameter. In this study, M is taken as 1, as proposed by Hillerborg et al. [67]. Eq. (5-16) can be used for both mode-I and mode-II loadings by inserting the corresponding G_c and τ_0 of the mode. The smaller of the different cohesive lengths obtained for mode I and mode II loading should be used. According to Eq. (5-16), cohesive zone length is 0.71 mm for IM7/8552 and 0.6 mm for S2 glass/MTM49L. There is not a well-established rule that determines the minimum number of elements required in the cohesive zone [18]. Turon et al. [18] showed that minimum two elements are needed in cohesive zone to simulate delamination, while use of minimum three elements were suggested by Davila and Camanho [68]. In this study, cohesive zone length for the laminates are selected such that there are two to three

elements in the cohesive zone. It is clear from Eq. (5-16) that cohesive zone length will not change as the laminate in-plane dimensions get larger. Thus, larger laminates will be computationally costly if the cohesive zone length and element size are small. In order to decrease the computation time, a larger cohesive zone length can be assumed for larger laminates by lowering the interface stiffnesses so that Eq. (5-16) is still satisfied [18]. In this study, cohesive zone lengths of Laminates 1 and 3 are artificially increased to 1.15 mm and 1.5 mm, respectively. Turon et al. [69] suggested that for accurate simulation of mixed-mode delamination, transverse tensile and shear strengths of the interface should be related to each other by an equation dependent on mode-I and mode-II fracture toughnesses. In the light of these, stiffness, cohesive zone length, number of elements in the cohesive zone, and interface strengths are determined for the laminates and are provided in Table 5-4.

Table 5-4 Cohesive layer parameters

	Laminate 1	Laminate 2	Laminate 3
Stiffness, $K [N/mm^3]$	$4.6 \cdot 10^6$	$1.1 \cdot 10^6$	$2.3 \cdot 10^6$
Cohesive zone length, $l_{cz} [mm]$	3	0.71	1.50
Element side length, $l_e [mm]$	1.15	0.3	0.5
Normal strength, $t_n^0 [MPa]$	29	60	45
Shear strength, $t_s^0 [MPa]$	58	90	57

In the analyses, damage initiation criterion based on quadratic nominal stresses and energy-based linear damage evolution with BK criterion are used for interlaminar damage. Normal and shear strengths listed in Table 5-4 are utilized in quadratic stress criterion, and mode-I and mode-II fracture toughness are utilized in the power law as fracture energies. For damage initiation, shear strengths in the first and second direction are assumed to be equal. Likewise, fracture energies in the first and second shear directions are assumed to be equal.

5.2.4. In-plane parameters

Literature survey showed that the Hashin's failure criterion is able to predict failure with good accuracy under longitudinal and transverse tensile loads. Therefore, in this study, Hashin's 2-D failure criterion [32] is used for in-plane damage initiation along with linear gradual damage evolution. The strength and stiffness data shown in Table 5-2 are directly utilized in Hashin's failure criterion. However, in order to accomplish damage evolution, energies dissipated during damage for fiber tension, fiber compression, matrix tension, and matrix compression failure modes should be input to the software. These energies can be based on experimentally determined values; however, experimental data about failure energies of material systems are quite scarce in the literature and the methods utilized to measure failure energies has not been standardized yet. Luckily, failure energies for longitudinal and transverse failure in tension are available in the literature [43] for IM7/8552 carbon fiber/epoxy, which is one of the material systems utilized in the study. Failure energy of matrix tension failure mode is determined by DCB, for fiber tension mode is determined by compact tension tests [43]. Although DCB yields the interlaminar critical energy release rate in mode I, Pinho et al. [45] stated that this value can be used also for intralaminar mode I critical energy release rate since their values were observed to be close to each other. Therefore, in this study, failure energy in matrix tension failure mode for S2 glass/epoxy is taken from DCB test. Compact tension test is not conducted for S2 glass/epoxy and there is no data in the literature about failure energy of S2 glass/epoxy in fiber tension failure mode. Therefore, failure energy of S2 glass/epoxy in fiber tension failure mode is taken as 52 N/mm , which is determined in [70] for fiberglass/epoxy. Experimental failure energies are shown in Table 5-5.

Table 5-5 Experimental failure energies

	$G_{ft} [N/mm]$	$G_{mt} [N/mm]$
IM7/8552	81 [43]	0.224 [43]
S2 glass/MTM49L	52 [70]	0.3

To illustrate the concepts of damage evolution and failure energy, let us imagine that a lamina is longitudinally loaded in tension. Elements in the lamina will start to fail in fiber tension mode once the applied stress is equal to longitudinal yield strength of the lamina (X_L). This point is shown as the point of “damage initiation” in Figure 5-11. Note that σ_{eq}^{ft} and δ_{eq}^{ft} refer to equivalent stress and equivalent strain in fiber tension mode. If damage evolution is not defined, the elements will continue to bear higher loads than X_L . If damage evolution is defined by specifying the failure energy of the longitudinal tension mode (G_{ft}), damage in the elements will grow such that the area under the equivalent stress vs. equivalent displacement graph equals the failure energy specified. Specifying a low failure energy will cause the degradation to be more instantaneous as shown in Figure 5-11-b. Likewise, a high failure energy will yield a more gradual degradation as in Figure 5-11-c. Thus, it is possible to control how gradual the degradation is by changing the specified failure energy.

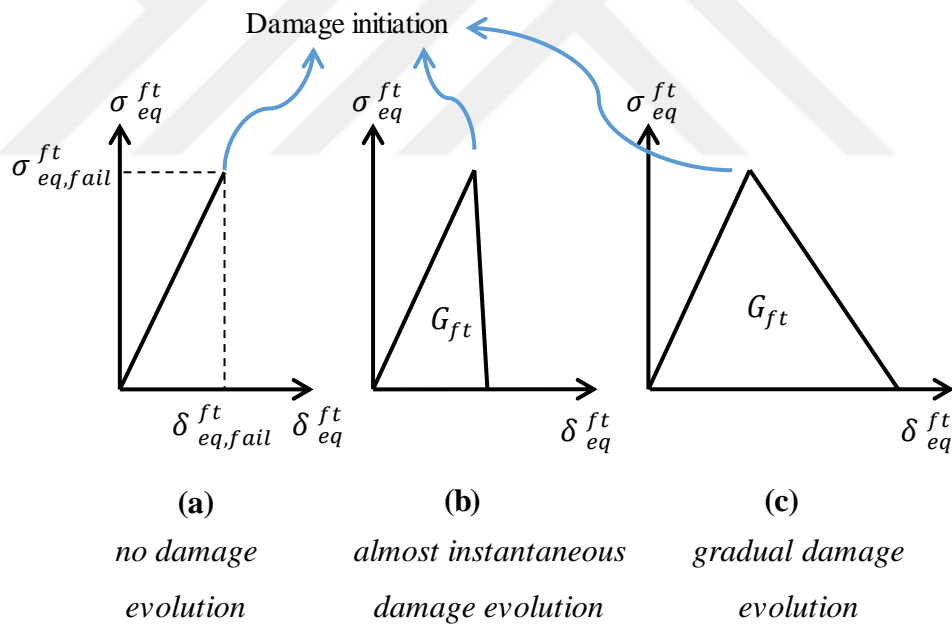


Figure 5-11 Failure energies in fiber tension failure mode

In this study, experimental failure energies and almost instantaneous failure energies calculated are used in order to investigate the effect of degradation trend on damage. Experimental failure energies yield gradual damage evolution as

shown in Figure 5-11-c. Almost instantaneous damage evolution is called as “instantaneous damage evolution“ and damage evolution based on experimental failure energies is called as “gradual damage evolution” in the text for simplicity.

Instantaneous failure energies are determined by assuming that total strain in the damage evolution region will be 10% of the strain elements experience until the damage initiation point. Failure energies of the fiber failure modes are determined by assuming a lamina loaded longitudinally in tension or compression and Failure energies of the matrix failure modes were determined by assuming a lamina loaded in transverse direction in tension or compression. Equivalent stresses and displacements in these failure modes are given in Eq. (3-16) – (3.13). For the fiber tension, fiber compression, matrix tension and matrix compression modes equivalent stress at damage initiation is simply equal to X_T , X_C , Y_T , and Y_C , respectively. Equivalent strain at damage initiation can be obtained by dividing equivalent stress by the modulus of elasticity. Equivalent displacement equals to the equivalent strain multiplied by characteristic length of the element, which is defined as the square root of the element’s face area for continuum shell elements [51]. Failure energies calculated by this methodology are provided in Table 5-6.

Table 5-6 Failure energies for instantaneous degradation

	G_{ft} [N/mm]	G_{mt} [N/mm]
Laminate 1	21.3	0.20
Laminate 2	5.5	0.052
Laminate 3	17.6	0.075

After determining the failure energies by analytical calculations, two finite element analyses are performed to check whether the failure energies input yielded an expected damage evolution behavior or not. In the analyses, two laminae made of S2 glass/epoxy with dimensions 3 mm x 6 mm x 0.225 mm and ply angles 0° and 90° are loaded in longitudinal and transverse tension as shown in Figure 5-12. Mesh size is 0.5 mm, which is equal to mesh size of Laminate 3. A failed element is selected from the lamina to plot equivalent stress vs. equivalent strain at one of its nodes. Equivalent stress vs. equivalent displacement

curves of damage evolution in fiber tension and matrix tension mode are provided in Figure 5-13 and Figure 5-14.

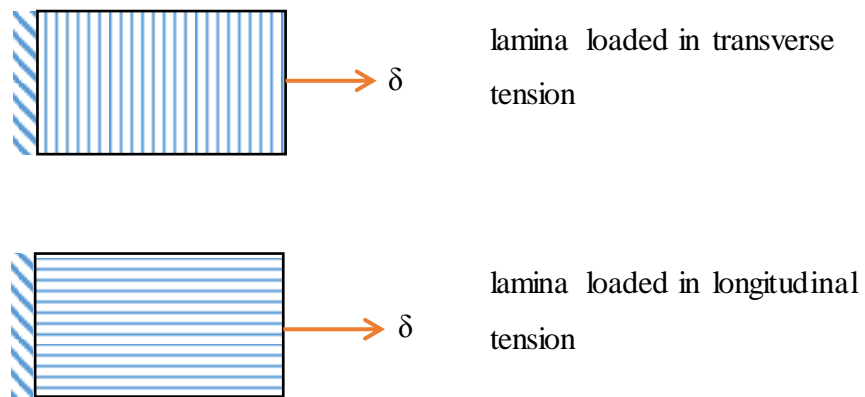


Figure 5-12 Laminae loaded in longitudinal and transverse tension

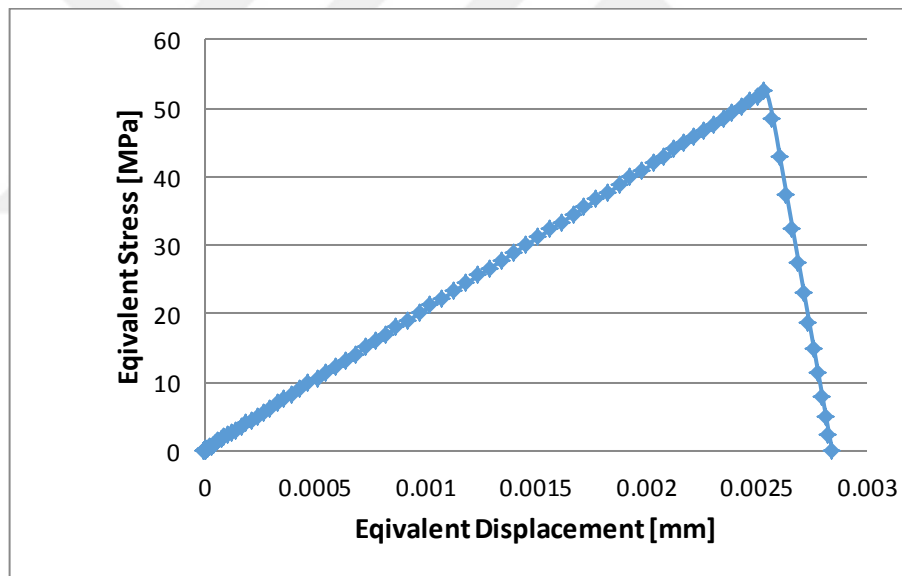


Figure 5-13 Equivalent stress vs. equivalent strain for a S2 glass/epoxy lamina in transverse tension

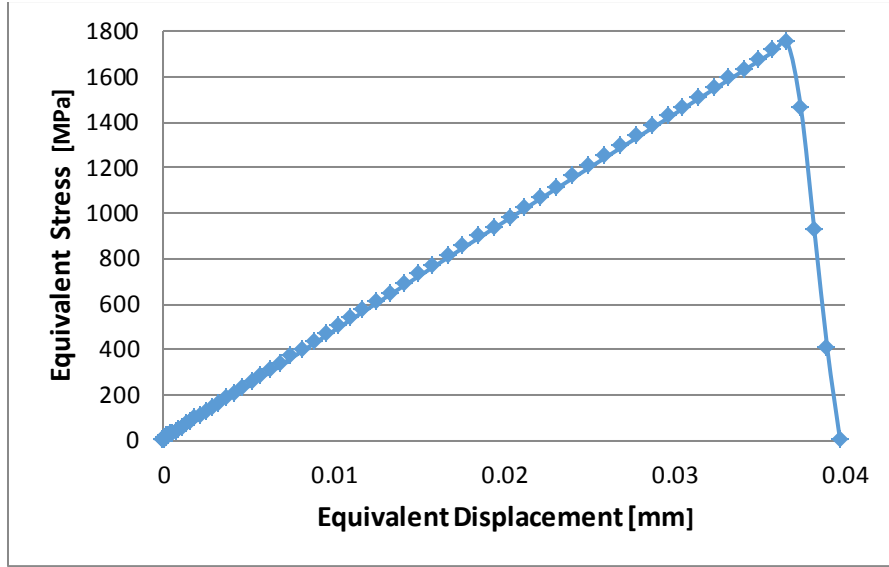


Figure 5-14 Equivalent stress vs. equivalent strain for a S2 glass/epoxy lamina in longitudinal tension

As seen from the figures, elements have failed in such a way that the slope of degradation line is high and equivalent displacements at total failure are the same as those calculated, which is expected according to the failure energies specified.

Another method to control the degradation trend is introducing damage stabilization into damage evolution. Damage stabilization in the software slows down the rate of increase of damage according to the equation

$$\dot{d}_v = \frac{1}{\eta} (d - d_v) \quad (5-17)$$

where d is inviscid damage variable, η is the viscous regularization coefficient responsible for damage stabilization, and \dot{d}_v is the viscous damage calculated after damage stabilization [51]. The extent of the stabilization, i.e. how gradual damage will evolve, depends on the value the viscosity parameter η . The larger the viscosity parameter, the slower is the rate of increase of damage. Therefore, combining a predetermined failure energy resulting in instantaneous degradation by itself with a sufficiently large viscosity parameter may yield gradual damage evolution.

In this study, viscosity parameter is utilized to investigate the effect of gradual degradation on damage behavior of the laminate 2 since experimental failure energy for fiber tension mode, which would yield gradual degradation, was not available in the literature for the laminate.

5.2.5. Additional Measures

One of the important steps in the modeling process is about the precision. Explicit analyses require high number of increments. Therefore, round-off errors may accumulate and lead to divergence and wrong results if the number of increments is too high when single precision solver is utilized. It is recommended by the software to use double precision solver when the number of increments is more than 300000. Analyses of the laminates 1 and 3 require more than 300000 increments, while analysis of laminate 2 require around 45000 increments. However, double precision solver is utilized for all types of laminate.

Lastly, while using reduced integration elements, hourglass modes of the elements should be considered. Reduced integration continuum shell elements have only one integration point in the planes perpendicular to their thickness direction. Thus, they show low resistance in some types of loadings, which requires extra stiffness to be defined to increase their resistance to these loadings. In this study, built-in “enhanced” hourglass control is used. An example of matrix damage in 0° layer of laminate 2 with and without hourglass control is shown in Figure 5-15. Blue color in the figure indicates no matrix damage and red color indicates full matrix damage. As seen in the figure, the laminate shown on the right side experiences a deformation in the form zig-zags. Zig-zag deformation pattern causes elements to experience shear strain, causing them to fail in matrix tension mode. In-plane shear strains in zig-zag regions is measured to be around 20 times of shear strains before the zig-zag formation, which is not typical in a real test where strains increase gradually.

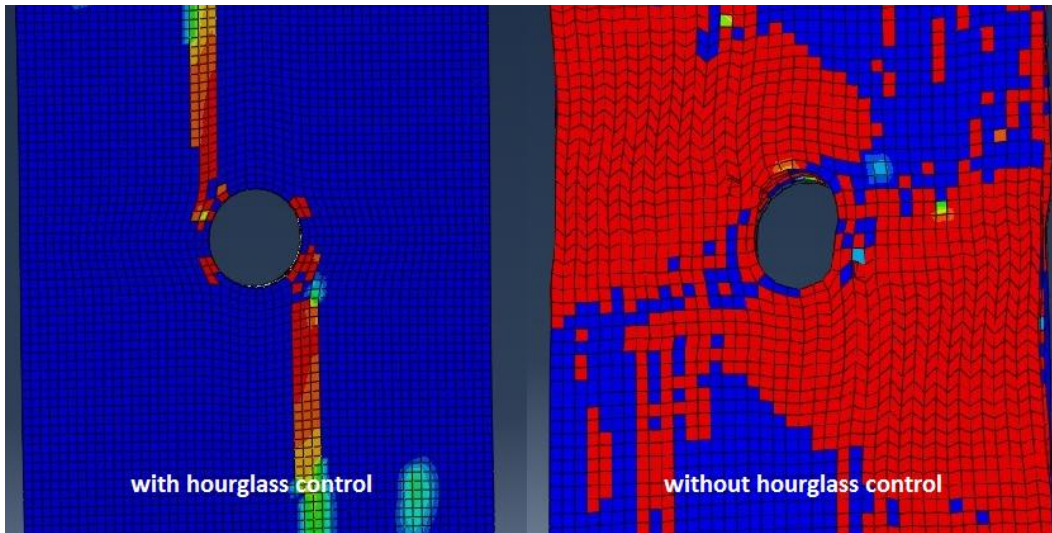


Figure 5-15 Effect of hourglass control on matrix damage

In order to have a realistic simulation, artificial strain energy resulting from hourglass control and viscous dissipation energy resulting from viscous regularization should be a small fraction of the strain energy of the part analyzed. By changing the displacement rate, viscous energy and artificial energy resulting from suppression of hourglass modes increase. Thus, displacements are applied in sufficiently long durations so that energy resulting from the mentioned effects remains low compared to strain energy.

CHAPTER 6

RESULTS

In this chapter, finite element analysis results will be presented and analysis results will be compared to the experimental results. Trend of load-displacement curve, ultimate load carried by the specimen, damage progression observed during the loading history, and damage pattern after failure are utilized as criteria for comparison between analysis and experimental results. The analyses are run with both nominal unidirectional lamina and in-situ strengths to investigate the effect of in-situ strength on the ultimate load. Instantaneous and gradual damage evolutions based on experimental failure energies are utilized to investigate the effect of degradation trend on damage. Effect of delamination on the damage of laminates is also discussed by removing cohesive layers from the finite element models.

The damage progression in the laminates is presented by damage parameter maps of plies and interfaces as in Figure 6-1. Colors in Figure 6-1 indicate the value of the damage parameter attained in a specific failure mode. Damage parameters can assume values between 0 and 1. The value “0” indicates that damage evolution has not taken place; i.e., stiffness of the material point has not been degraded yet. The value “1” indicates that the integration point is totally degraded, so the integration point is assumed to carry no more stress. Values between “0” and “1” indicate partial degradation. Figure 6-1 shows color code of the damage parameter.

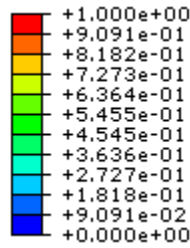


Figure 6-1 Color code for damage evolution parameters

6.1. Laminate 1 (Laminate Exhibiting Brittle Failure)

6.1.1. Analysis with Cohesive Layers

Finite element models with and without in-situ strengths are utilized for progressive failure analysis. Figure 6-2 shows load-displacement curves obtained by the FEA with instantaneous degradation. It can be interpreted from the figure that models yield similar load-displacement curves that are in agreement with the trend of experimental curve shown in Figure 4-2. Similar curves yield similar damage progression patterns for the models. In both models, the fiber and matrix damages initiate and propagate simultaneously. There is no damage induced in the laminate from the beginning of the loading to point *a*. At point *a*, fiber failure initiates around the hole at layers with fiber angles 0° , 45° , and -45° . Fiber failure is accompanied by matrix failure at all layers. As the load increases, fiber and matrix failures in the aforementioned plies propagate simultaneously. Load drops instantaneously to zero after the ultimate load. Damage pattern after failure, which is shown in Figure 6-3, is characterized by fiber fracture at all layers except 90° plies which, on the other hand, fail through matrix failure. The delamination is quite small in size, confined to very vicinity of the hole. Damage pattern obtained agrees with the experimental damage pattern shown in Figure 4-2. Damaged element tags in Figure 6-3 show that the fracture surface in Figure 4-2 is simulated well by the analysis.

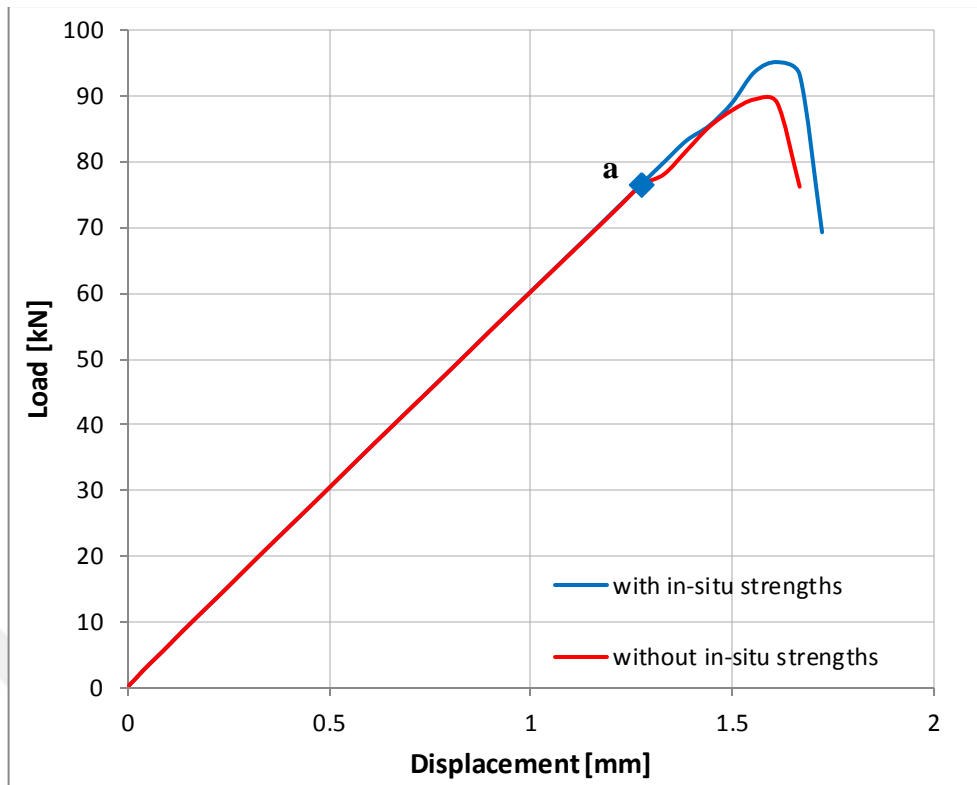
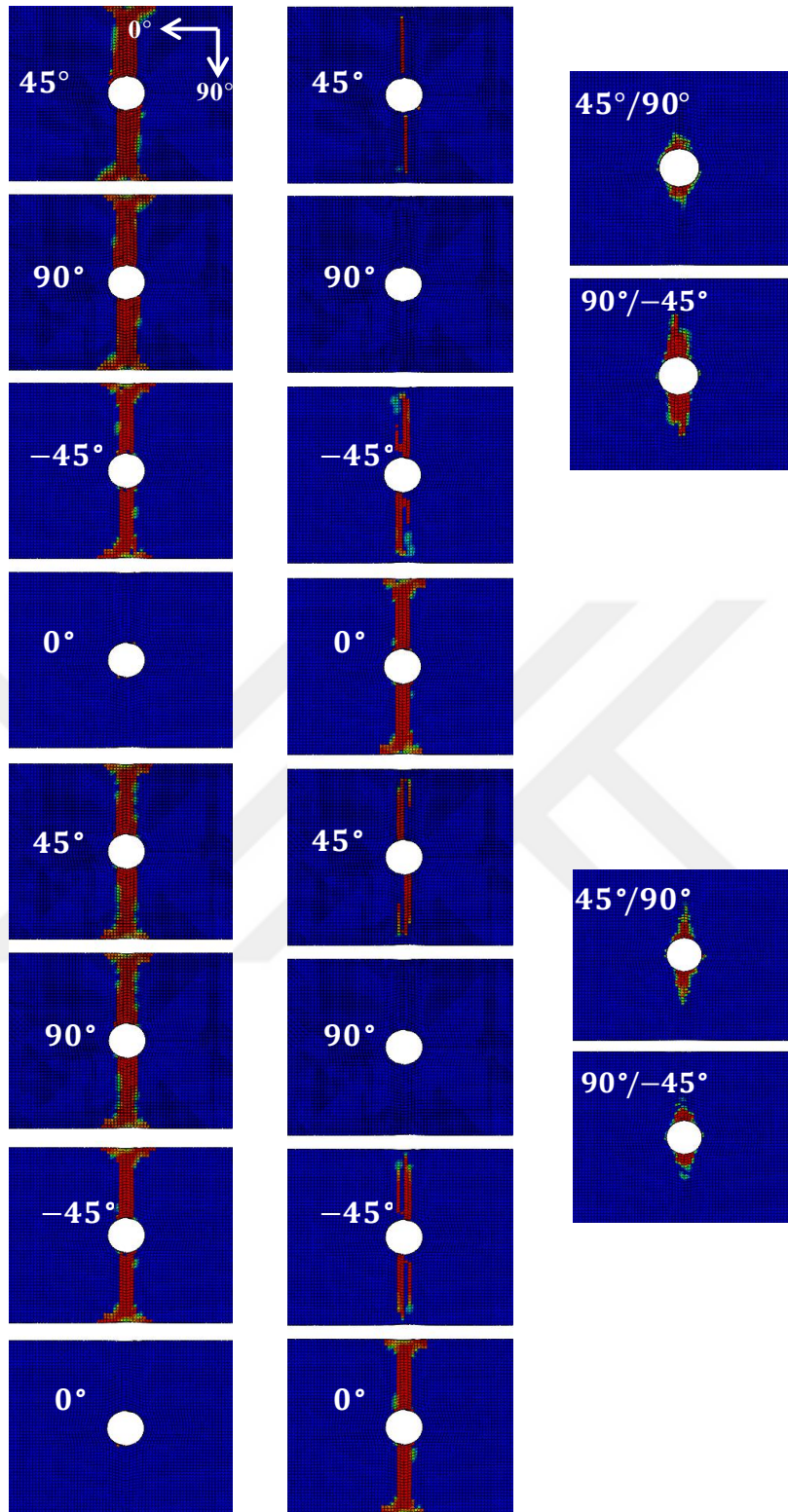


Figure 6-2 Load-displacement curve from FEA of Laminate 1 with instantaneous degradation

In reality, fiber fracture causes matrix around the fibers to crack as well. However, built-in damage scheme of the software does not force matrix damage when fiber failure occurs at a material point. This is assumed to be the reason why 0° plies in Figure 6-3 seem undamaged in matrix tension mode.



matrix tension damage fiber tension damage delamination damage

Figure 6-3 Damage at Laminate 1 after failure (gradual degradation)

When gradual degradation is utilized, the damage pattern of the laminate is quite similar to that obtained with instantaneous degradation. Damage initiation takes place around the same load levels observed with instantaneous degradation; however, load continues to increase for a long time since the degradation rate is slow. Load-displacement curves obtained with the gradual degradation are shown in Figure 6-4.

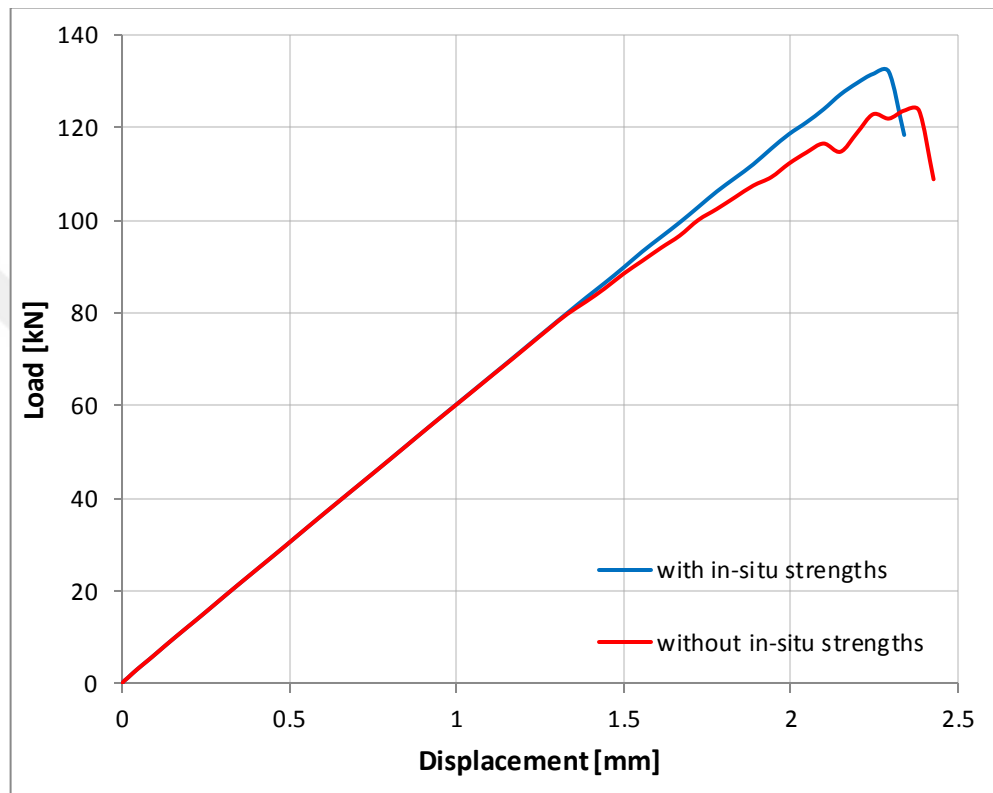


Figure 6-4 Load-displacement curve from FEA of Laminate 1 with gradual degradation

In addition to the trend of load-displacement curve and damage progression pattern, ultimate loads predicted with the instantaneous degradation are also in agreement with the experimental ultimate as shown in Table 6-1. Ultimate loads obtained differ extensively depending on the model. The models with the instantaneous degradation underestimate the ultimate load, while those with gradual degradation overestimate. The discrepancy between the experimental ultimate load and analysis results are less for the models with the instantaneous degradation as shown in Table 6-1.

Table 6-1 Comparison of the ultimate loads for Laminate 1

		Ultimate Load [kN]	Experimental Ultimate Load [kN]
Instantaneous	with in-situ	95.1	95.0
	without in-situ	89.5	
Gradual	with in-situ	132.0	
	without in-situ	123.6	

6.1.2. Analysis without Cohesive Layers

Removing cohesive layers from the finite element model does not cause a significant difference in the damage progression pattern of the laminae since delamination is not a dominant failure mechanism in the laminate. Change in the ultimate load is negligible as shown in Figure 6-5 as the energy dissipated by delaminated elements is too low.

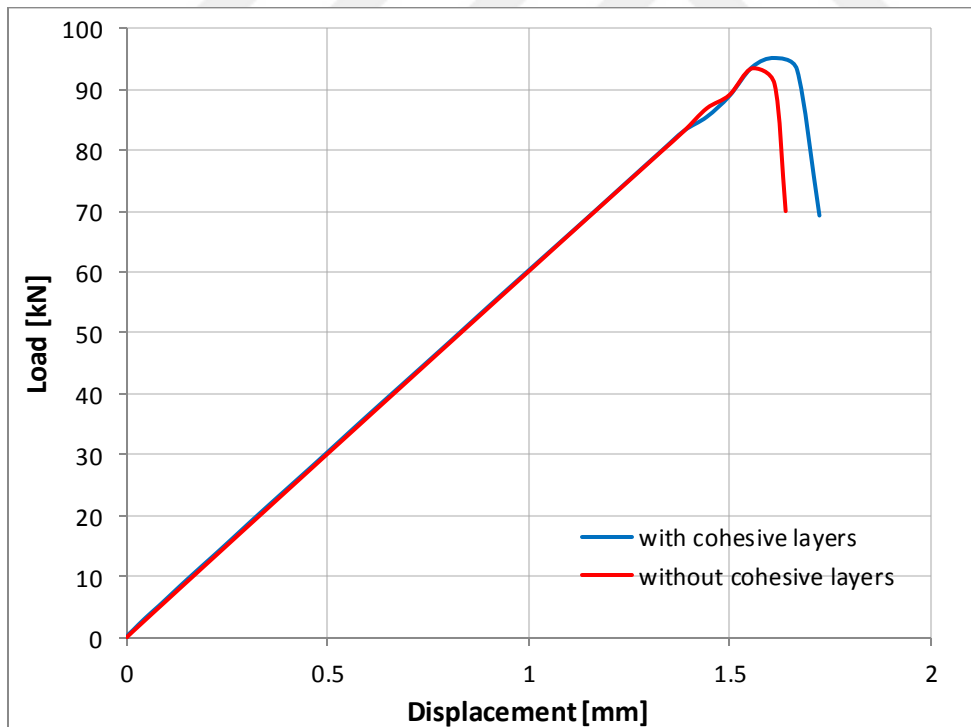


Figure 6-5 Load-displacement curve from FEA of Laminate 1 with and without cohesive layers (instantaneous degradation)

6.2. Laminate 2 (Laminate Exhibiting Delamination Failure)

6.2.1. Analysis with Cohesive Layers

Finite element analysis of Laminate 2 was the most challenging one since the delamination caused mesh distortion, which affects the load re-distribution as the damage grows. Effect of in-situ strengths and damage evolution is discussed before investigating damage progression in detail.

Considering in-situ strengths increases the ultimate load carried by the laminate considerably. This trend can be attributed to the observation that the first load drop of the laminate starts with failure of 45° and 90° plies in tension. Since the transverse tensile and in-plane shear strengths of the laminae is increased by using in-situ strengths, 45° and 90° plies bear higher loads when in-situ strengths are used.

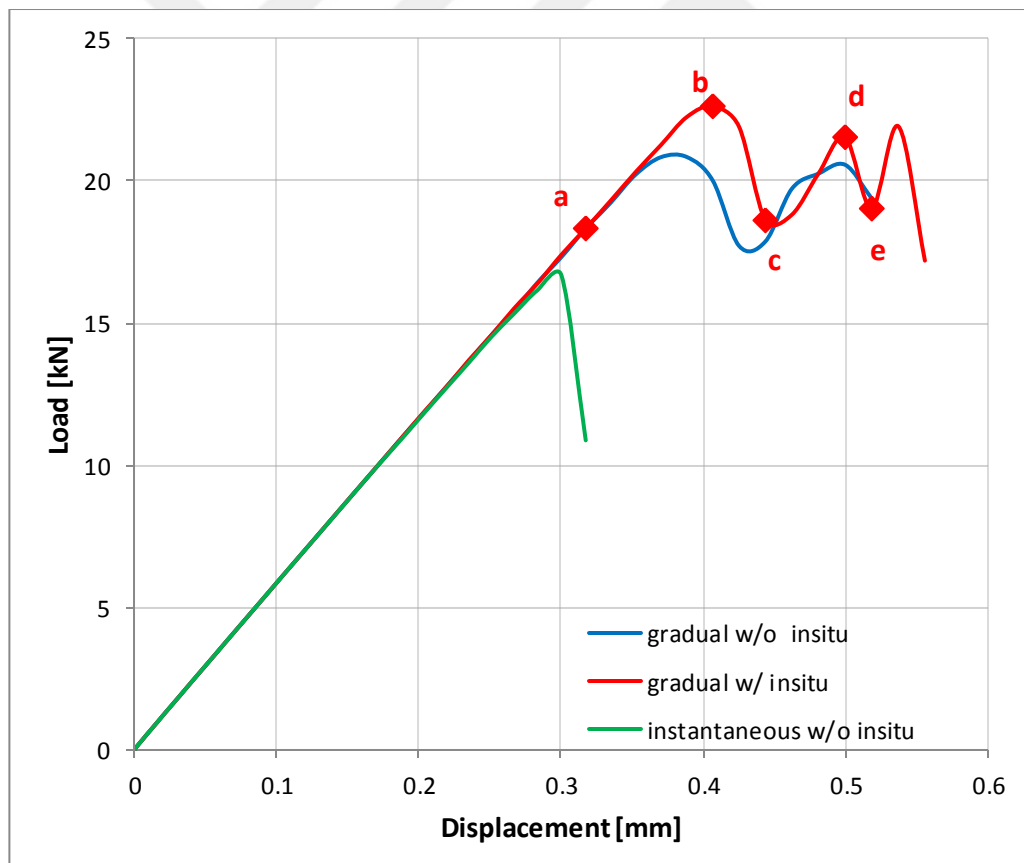


Figure 6-6 Load-displacement curve from FEA of the Laminate 2 by FEA

Figure 6-6 shows load-displacement curves obtained with instantaneous and gradual damage evolution. The load-displacement curve shows that instantaneous degradation results in a single load drop contrary to the experimental results where two load drops are observed due to delamination and 0° plies continued to carry load after the load drops due to delamination. Single load drop is caused by the high fiber tensile damage right after 45° and 0° plies fail and $-45^\circ/0^\circ$ interface delamination extends to the grips. High fiber damage in 0° plies causes undamaged fiber strips to be insufficient to bear higher loads; therefore, the load continues to drop after the delamination damage.

With the use of gradual degradation, fiber damage in 0° plies after delamination decreases compared to the previous analysis and undamaged strips in 0° plies are able to bear increasing loads. The two load drops due to delamination are simulated by gradual degradation successfully. Moreover, the model with both in-situ strengths and gradual degradation exhibits an increase in the load after the two load drops. The increase in the load results from undamaged 0° strips carrying load.

Important points in the load-displacement curve of the analysis with gradual degradation are marked by the letters *a*, *b*, *c*, *d*, and *e*. Point *a* is located at 90% ultimate load to make a comparison with experimental x-ray image. Point *b* denotes the ultimate load, point *c* is the point after the first load drop due to delamination, point *d* is the point where second load drop due to delamination starts, and point *e* is the point where delamination in $-45^\circ/0^\circ$ interface is completed and load starts to increase again due to undamaged 0° strips. Figure 6-8 shows the matrix tensile damage and x-ray image taken at 80% ultimate load, which is not as developed as the damage shown in the x-ray image shown in Figure 6-8. However, the damage pattern predicted at 90% ultimate load shown in Figure 6-8 is observed to be quite similar to the damage pattern shown by the x-ray image, which means that FEA yields hampered damage predictions.

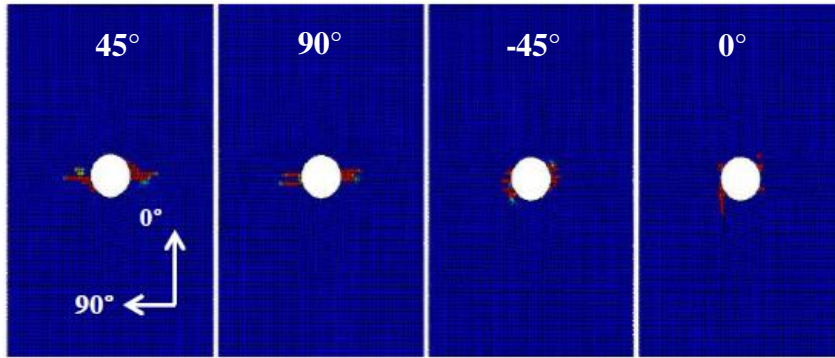


Figure 6-7 Matrix tension damage pattern for Laminate 2 at 80% ultimate load

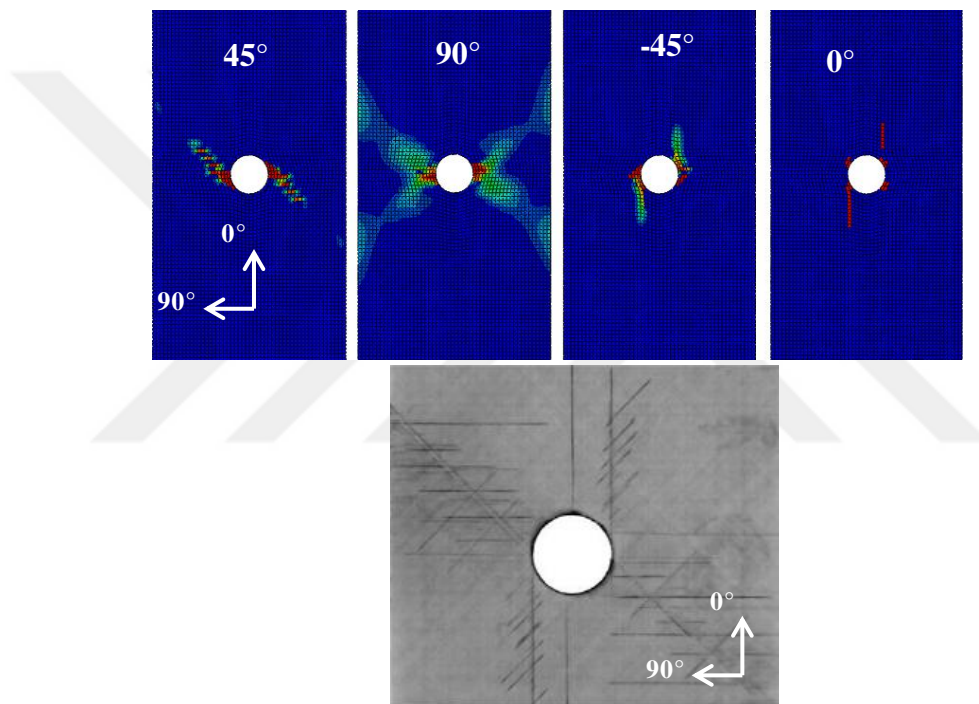


Figure 6-8 (Top) Matrix tension damage at 90% ultimate load for Laminate 2 (Bottom) X-ray image at 80% ultimate load [12]

At point *b*, matrix tension damage at 45° reaches the maximum value as shown in Figure 6-9 and the load starts to drop with increasing delamination at $-45^\circ/0^\circ$ interface.

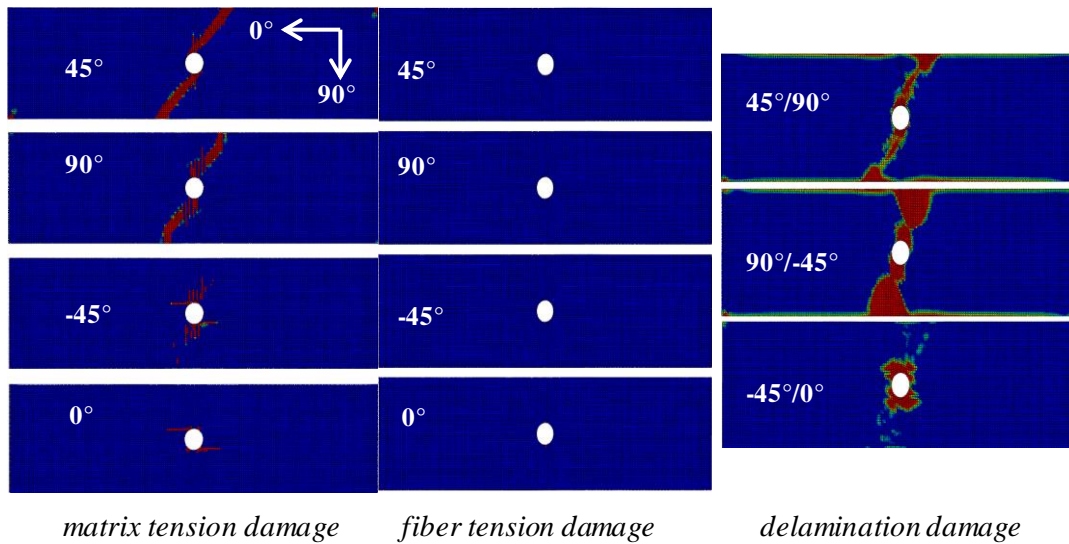


Figure 6-9 Damage at point b ($F = 22.6 \text{ kN}$, $U = 0.41 \text{ mm}$)

From point *b* to point *c*, delamination at $-45^\circ/0^\circ$ interface grows asymmetrically and delamination growth stops at point *c*, causing load to increase. Splits in the off-axis plies and delamination at interfaces shown in Figure 6-10 match the damage pattern shown by the x-ray image taken after first load drop, shown in Figure 4-4. Note that delamination at $-45^\circ/0^\circ$ interface is asymmetric, as observed in the x-ray image in Figure 4-4.

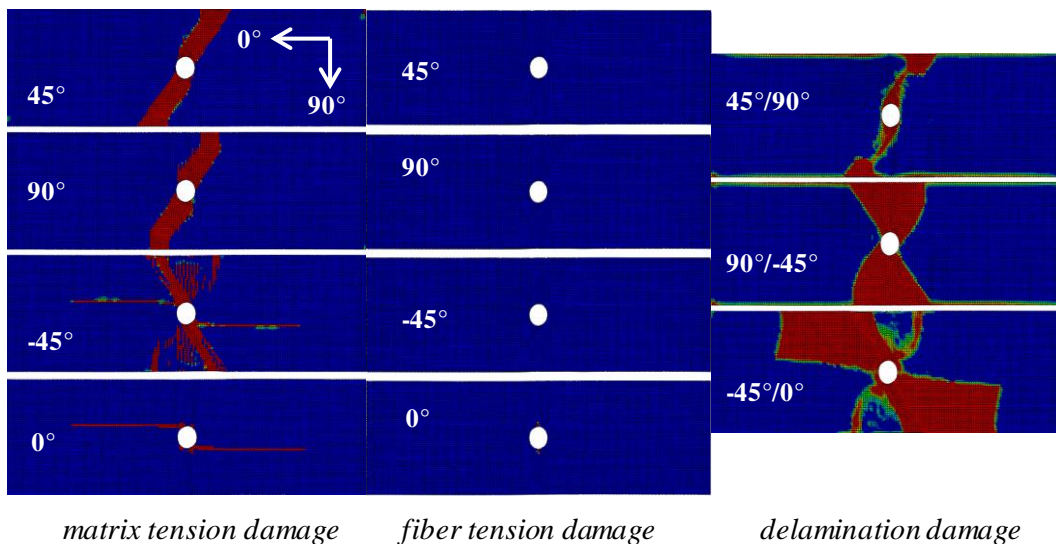


Figure 6-10 Damage at point c ($F = 18.6 \text{ kN}$, $U = 0.44 \text{ mm}$)

As the load increases from point *c* to *d*, asymmetric delamination and matrix split marks in 0° plies grow towards the grips. In the meantime, the load increases since 0° plies bear a considerable load. Finally, at point *d* ($F = 21.8 \text{ kN}$, $U = 0.59 \text{ mm}$), which is a local maximum point, delamination at $-45^\circ/0^\circ$ interface starts to grow again. This time, other asymmetric half of the interface experiences delamination. Damage state at point *d* is shown in Figure 6-11.

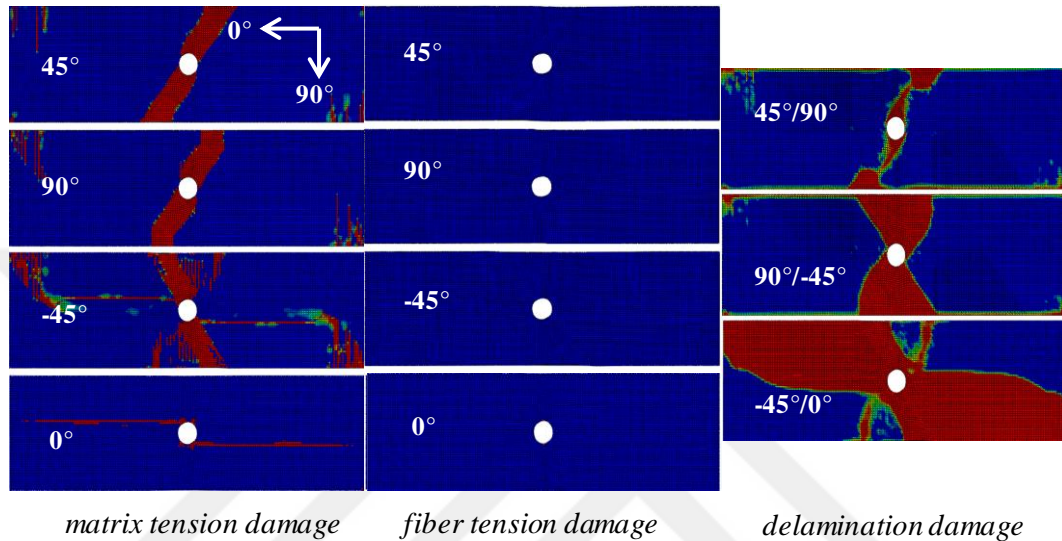


Figure 6-11 Damage at point *d* ($F = 21.5 \text{ kN}$, $U = 0.5 \text{ mm}$)

From point *d* to point *e*, load decreases due to delamination in the undamaged half of the $-45^\circ/0^\circ$ interface. At point *d*, $-45^\circ/0^\circ$ interface is subject to full delamination and undamaged strips in 0° plies carry load for some more time until load drops suddenly due to extensive mesh distortion. It can be inferred from the longitudinal stress state at 0° plies shown in Figure 6-12 that if the mesh distortion was prevented, load would increase as in the experiments as shown in Figure 4-4.

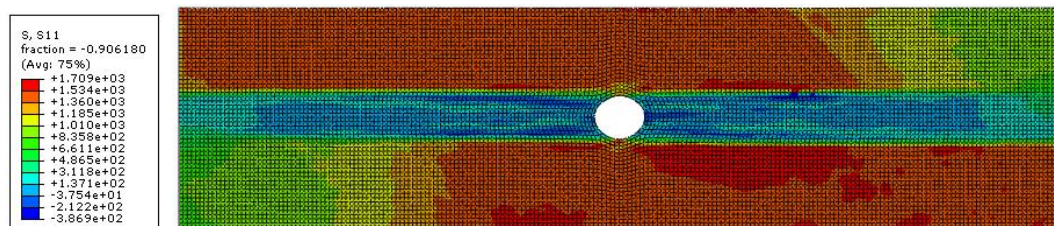


Figure 6-12 Longitudinal normal stress (σ_{11}) distribution in 0° plies at point *e*

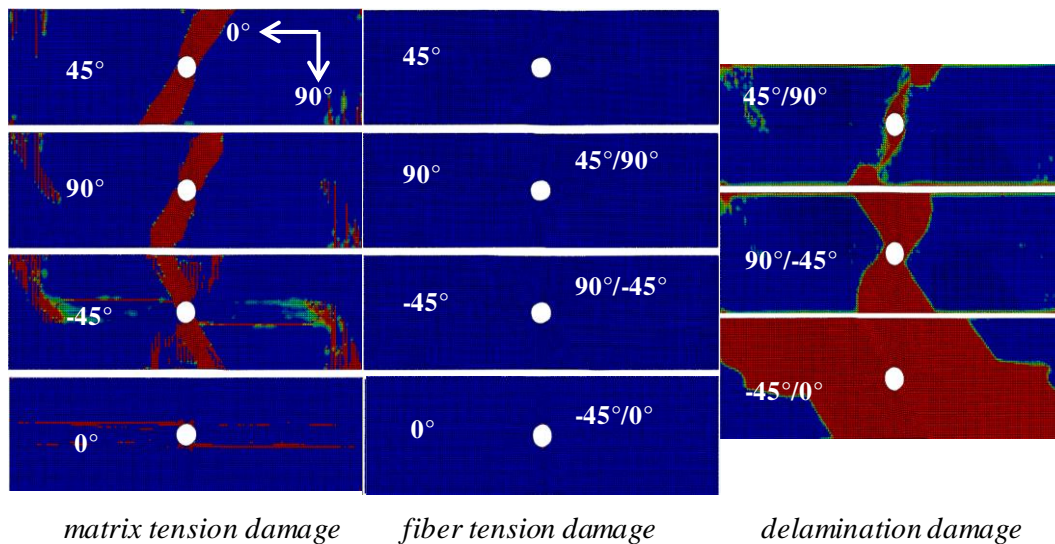


Figure 6-13 Damage at point *e* ($F = 19.0 \text{ kN}$, $U = 0.52 \text{ mm}$)

Failure of all the fibers in 0° plies cannot be simulated. This does not pose a problem because in the experimental study, ultimate load is taken as the load after which more than 5% load drop is observed. Since 5% load drop corresponds to first load drop due to delamination, finite element model is able to predict ultimate loads.

The model without gradual degradation is better in predicting damage pattern, although it yields high ultimate loads compared to experimental ultimate loads. Ultimate loads predicted by the analyses are given in Table 6-2.

Table 6-2 Comparison of the ultimate loads for Laminate 2

		Ultimate Load [kN]	Experimental Ultimate Load [kN]
Instantaneous	with in-situ	16.7	17.5
Gradual 1	with in-situ	22.6	
	without in-situ	20.8	

It is seen in Table 6-2 that ultimate loads are overpredicted with gradual damage evolution. While gradual damage evolution allows smooth stress re-distribution as the damage grows, it is responsible for high ultimate loads.

6.2.2. Analysis without Cohesive Layers

Removing the cohesive layers from the finite element model with gradual degradation and in-situ strengths, the analysis is re-run. Load-displacement curve of the model with and without cohesive layers are shown in Figure 6-14 for comparison.

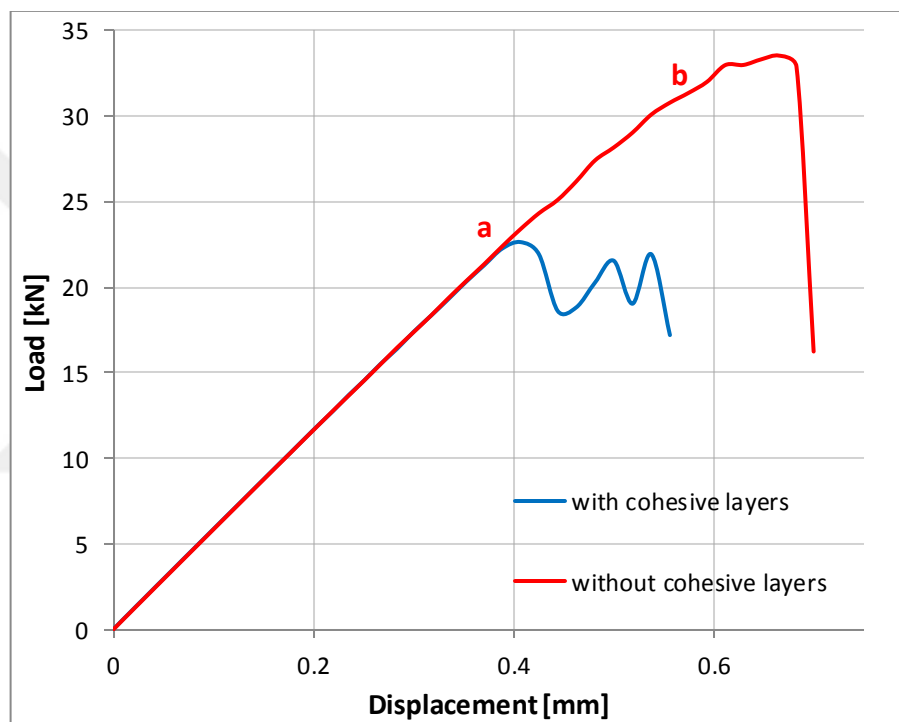


Figure 6-14 Load-displacement curve from FEA of Laminate 2 with and without cohesive layers (in-situ model with gradual degradation)

It can be seen in Figure 6-14 that by ignoring delamination the laminate experiences only one load drop. At point *a*, 45° plies fail in matrix tension and very short split lines form around the hole in 0° plies. As the load increases from point *a* to *b*, split lines do not grow in length considerably, unlike for the model with cohesive layers. As the load increases, fibers in the 0° plies fail gradually and at the peak load, load drops suddenly to zero. The final damage state of the

laminate after failure consists of matrix failure in all off-axis plies and fiber failure in 0° ply with very short split lines. In conclusion, the model without cohesive layers captures neither the damage state after failure nor the damage progression, accurately.

6.3. Laminate 3 (Laminate Exhibiting Pull-out Failure)

6.3.1. Analysis with Cohesive Layers

For Laminate 3, several analyses are conducted to investigate the effect of damage evolution trend on the damage characteristics. Although fiber tensile failure energy for fiberglass/epoxy laminates is found from literature and matrix tensile failure energy is obtained by the DCB test, another gradual degradation case is simulated by utilizing a high viscosity parameter of $\eta = 10^{-4}$ in combination with instantaneous degradation failure energies. The cases that are simulated considering in-situ strengths are tabulated in Table 6-3.

Table 6-3 Cases for FEA of Laminate 3 with in-situ strengths

	G_{ft} [N/mm]	G_{mt} [N/mm]	η
Instantaneous	17.6	0.075	-
Gradual 1	17.6	0.075	10^{-4}
Gradual 2	52	0.3	-

Load-displacement curves of the three cases tabulated in Table 6-3 are provided in Figure 6-15.

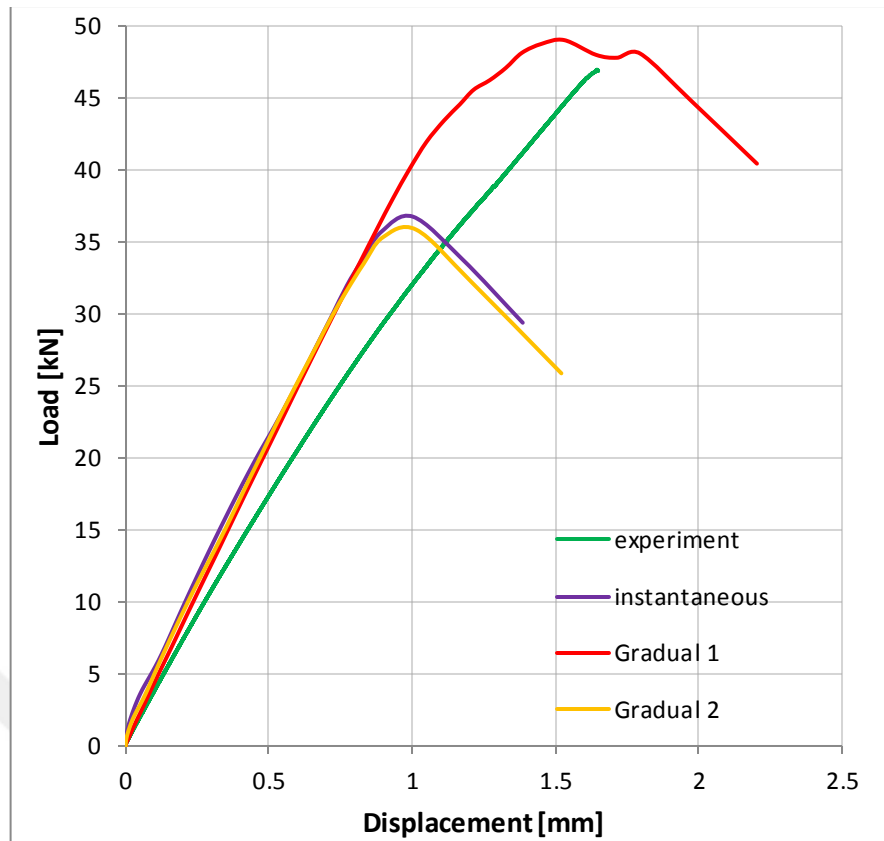


Figure 6-15 Load-displacement curves obtained with different degradation trends for Laminate 3 (with in-situ strengths)

It is seen in Figure 6-15 that degradation trend has a significant effect on the ultimate loads attained. Although pull-out failure is observed in all of the analyses, progression of damage is different since the instantaneous degradation did not allow gradual stress redistribution. The models “instantaneous” and “gradual 2” exhibited sudden fiber damage growth in 0° layers, which caused failure at low ultimate loads. For these laminates, there is not a significant load difference between the time fiber damage starts and the time ultimate load is attained. Since the longitudinal failure energy utilized for the model “gradual 2” does not belong to S2 glass/epoxy, it may underrepresent the real failure energy of the material system, which causes instantaneous failure. On the other hand, in the model “gradual 1”, laminate continues to bear higher loads for a long time as the fiber damage in 0° plies propagated. Ultimate load obtained with the model “gradual 1” is in agreement with the experimental ultimate load value. In the

following discussion, only the model “gradual 1” will be investigated in detail for the damage progression.

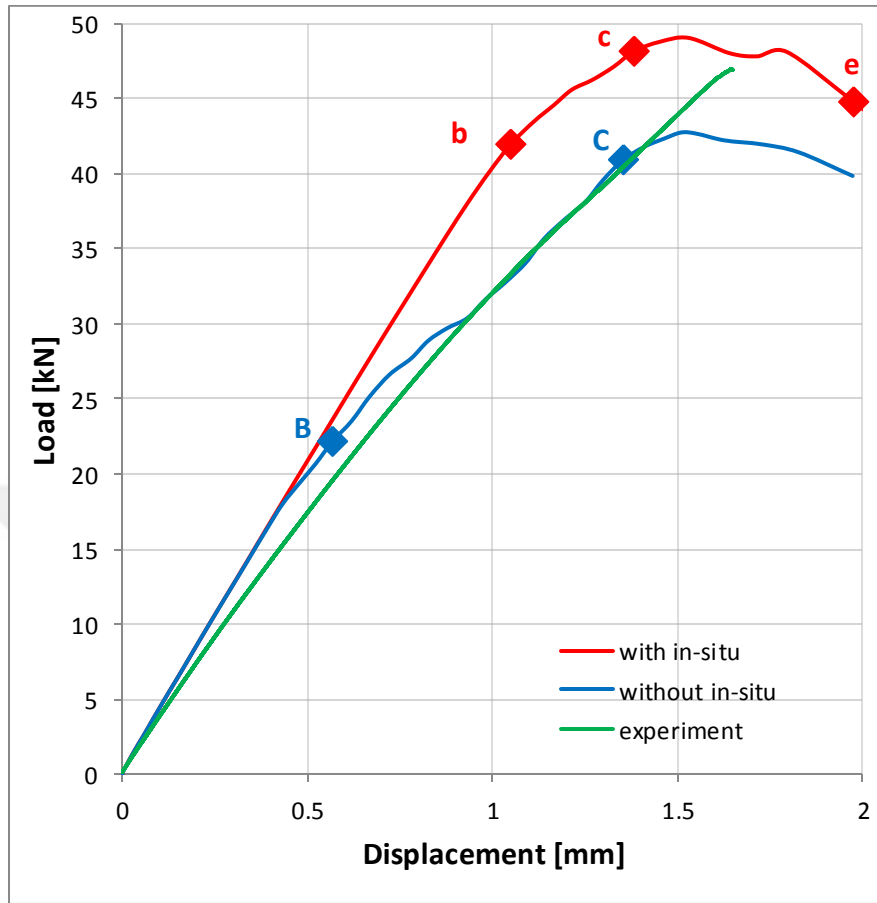


Figure 6-16 Load – displacement curve from FEA of Laminate 3

Figure 6-16 shows the predicted load-displacement curves of Laminate 3 considering two different models. The difference in the models is utilization of in-situ strengths for transverse tensile and shear strengths.

Important points on the curve of the model with in-situ strengths are marked by letters *b*, *c*, and *e*; and those on the curve of model without in-situ strengths are marked by letters *B* and *C*. Moreover, damage states *b* and *c* shown in Figure 4-6 roughly correspond to damage states at points *B* and *C* in Figure 6-16, respectively.

Points *b* and *B* indicate instants when some of the off-axis plies are subjected to an extensive damage causing slope of the load-displacement curve to decrease. In

the model without in-situ strengths, point *B* corresponds to the instant when 90° plies are damaged extensively. In the model with in-situ strengths, however, the damage pattern at the slope change is different. At point *b*, outer 45° and inner 90° plies are damaged. In the model without in-situ strength, 45° plies are damaged at a later instant, which is expected, since transverse tensile strength of all the layers are the same and transverse tensile stress in 90° layers are higher than in 45° layers. In the model with in-situ strengths, although transverse tensile stress in 90° layers are still higher than in 45° layers, failure in 45° starts earlier as the transverse tensile strength of thin outer plies are lower than that of thin inner plies. A slope change is also observed in the experimental load-displacement curve shown in Figure 4-7; however, the driving mechanism of this slope change is not known since the damage in the laminate could not be tracked in detail at that instant. Matrix tension and delamination damage at point *b* is shown in Figure 6-17. Fiber damage is not shown in the figure since the fiber damage starts at point *c* in the 0° layer. It can be noted from the figure that matrix damages of inner and outer 45° layers are different. Damage at point *B* will be similar to damage shown in Figure 6-17, except that matrix damage in outer 45° layers is similar to that of inner 45° layers at that instant.

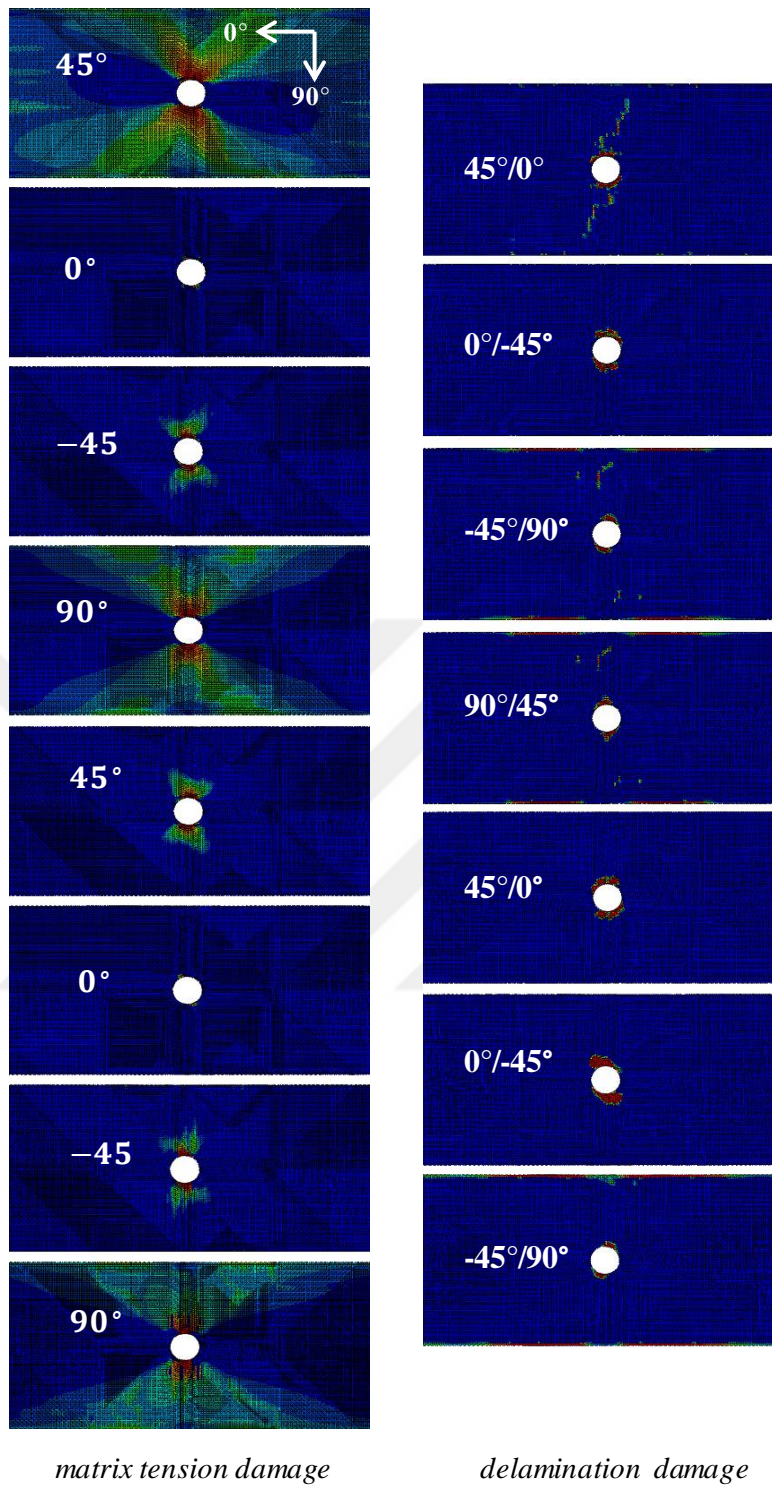


Figure 6-17 Damage at point b ($F = 42.4 \text{ kN}$, $U = 2.2 \text{ mm}$)

As the load increases from point b to point c , the matrix damage in the outer 45° and 90° layers expands towards the grips, and at point c these layers are highly

damaged. In the meantime, the damage in -45° and inner 45° layers grow, but not as much as the damage in the outer 45° and 90° layers. Damage in -45° and inner 45° layers remains confined to vicinity of the hole as shown in Figure 6-18. After point *c*, fiber failure in 0° layers and matrix damage in -45° and inner 45° layers propagate together and with the increase of damage in 0° layers, load starts to drop. Damage growth trend characterized by growth of matrix damage in off-axis plies along with fiber damage in 0° layers agree with the damage growth trend observed in the experiment.

In the case of model without in-situ strengths, all the off-axis plies are extensively damaged in matrix tension mode by the time fiber failure in 0° layers starts at point *C*. Damage progression after point *C* is similar to that of model with in-situ strengths.

Figure 6-19 shows the damage state of the model with in-situ strength at point *e* that is in the load-drop region. Since total load drop causes mesh distortion, point *e* is chosen to show the damage state after laminate fails. In the figure, it is seen that only 0° plies are damaged in fiber tension mode and all other plies are damaged in matrix tension mode. Aforementioned intralaminar damage is accompanied by a moderate delamination at the interfaces. This damage pattern is in agreement with the damage pattern observed in Figure 4-7, which shows the damage in the laminate after OHT experiment.

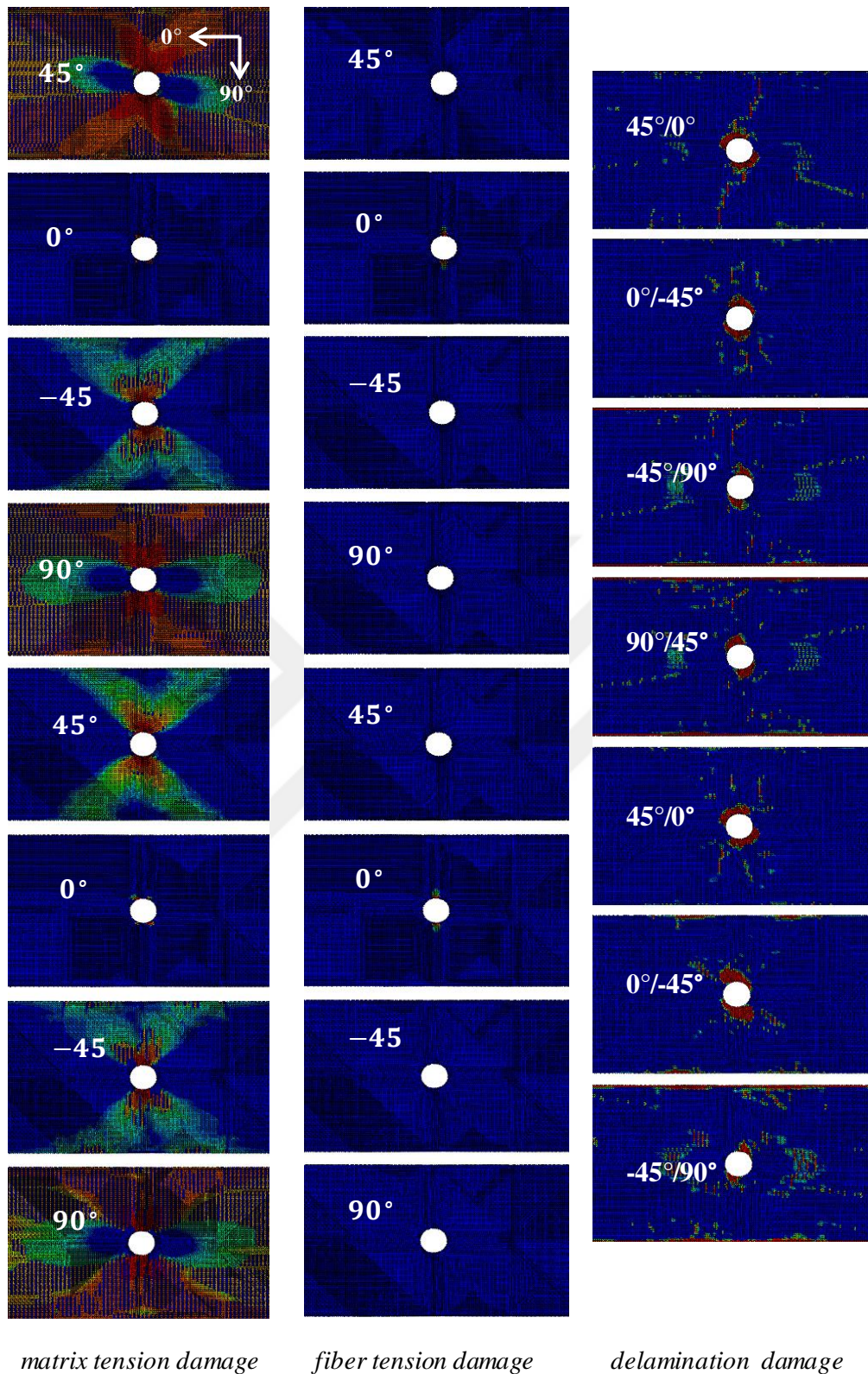


Figure 6-18 Damage at point *c* ($F = 48 \text{ kN}$, $U = 2.9 \text{ mm}$)

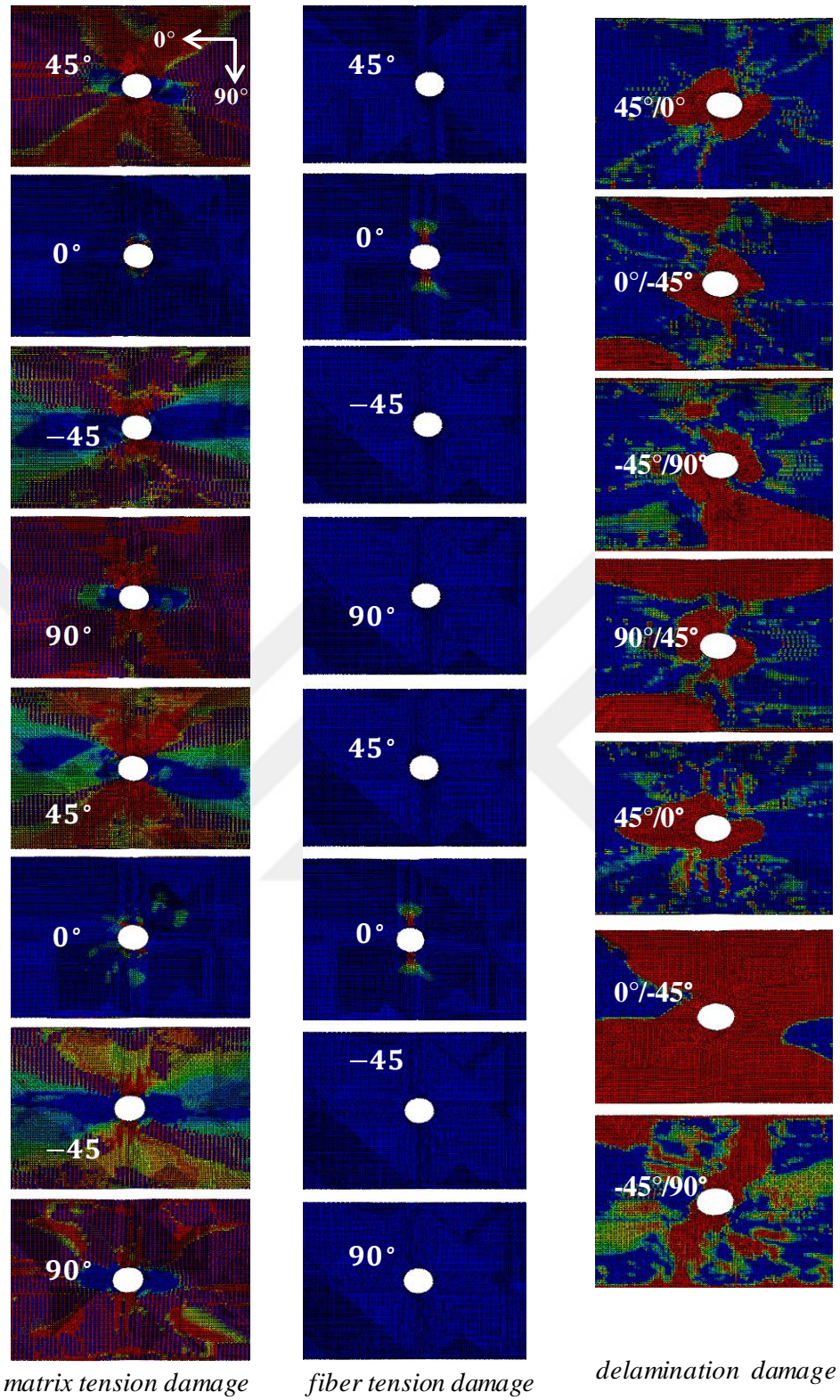


Figure 6-19 Damage at point e ($F = 46 \text{ kN}$, $U = 3.52 \text{ mm}$)

Ultimate loads obtained by the analyses with gradual degradation are in good agreement with experimental values as shown in Table 6-4, whereas instantaneous degradation causes underestimation of the ultimate load by 23% of the experimental value. Model with in-situ strengths yields a better estimation for the ultimate load.

Table 6-4 Comparison of the ultimate loads for Laminate 3

		Ultimate Load [kN]	Experimental Ultimate Load [kN]
Instantaneous	with in-situ	36.8	48.7
Gradual 1	with in-situ	48.8	
	without in-situ	45.1	

Utilization of a viscosity parameter to simulate gradual degradation arose from the observation that the fiber failure energy obtained from the literature and the matrix failure energy obtained by the DCB test resulted in an instantaneous-like failure. Since the fiber failure energy obtained from the literature [70] is not specific to S2 glass/epoxy, it may not represent the real failure energy of the material system. Therefore, a parametric study is conducted to observe the effect of fiber failure energy on the damage and ultimate load. When experimentally determined matrix energy is utilized and fiber failure energy is increased starting from 52 N/mm , ultimate load is observed to increase. However, a too high fiber failure energy of around 150 N/mm is seen to cause off-the axis plies to fail by matrix failure before the total failure, which yields a slight load drop before the ultimate load drop. When fiber failure energy of 100 N/mm is utilized along with a high matrix failure energy of 0.8 N/mm , load-displacement curve is seen to show high agreement with the experimental data. Therefore, it is concluded that utilization of higher fiber and matrix failure energies yields analysis results closer to experimental ones. While a high fiber failure energy of around 100 N/mm may be close to real fiber failure energy of S2 glass/epoxy material system, utilization of a matrix failure energy of around 0.8 N/mm is questionable. According to the DCB test results, the matrix failure energy gradually increases

from 0.3 N/mm when the crack starts to grow, to around 1 N/mm when the crack has propagated by 30 mm . Although it is seen from the DCB test that the propagation failure energy of 0.8 N/mm is a possible matrix failure energy for the material system, it is suggested to utilize initiation failure energy since increasing failure energies with increasing crack length is a result of fiber bridging [56]. It is claimed that the fiber bridging is a phenomenon encountered in the DCB tests where specimens are unidirectional; thus, propagation energies, which are higher than initiation energy, would overestimate the failure energy for delamination damage. This is because delamination usually takes place between the plies with different fiber orientations and fiber bridging is not a problem at such interfaces [56]. However, the matrix failure energy obtained by the DCB test is utilized for intra-ply failure in the analyses where fiber bridging might still matter during crack growth, which might justify utilization of higher matrix failure energy than initiation failure energy.

6.3.2. Analysis without Cohesive Layers

In this section, only the model with in-situ strengths is considered. The model with in-situ strengths is re-constructed by removing cohesive layers from the model. Load-displacement curves of the models with and without cohesive layers are provided in Figure 6-20.

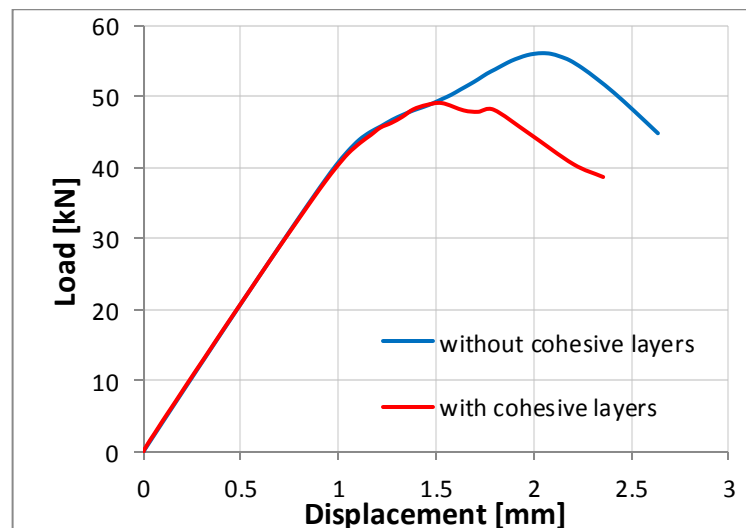


Figure 6-20 Load-displacement curve from FEA of laminate 3 with and without cohesive layers

As seen in Figure 6-20, ignoring delamination causes ultimate load obtained by FEA to increase by around 14%.

Removing cohesive elements from the finite element model also caused failure pattern to change to brittle failure. According to the FEA of Laminate 3 without cohesive layers, 45° , -45° , and 0° plies underwent fiber fracture, which contradicts the experimental failure pattern in which 45° and -45° plies were subject to matrix splitting.

It should be noted that load-displacement curves of the two analyses are coincident until the load starts to drop in the model with cohesive layers. This shows that delamination is only prevalent in the very last stages of the loading, which is in agreement with delamination progression observed in the experiments as shown in Figure 4-6.

CHAPTER 7

SUMMARY, DISCUSSION AND FUTURE WORK

7.1. Summary

A finite element modeling methodology is developed to simulate progressive failure of open-hole tension laminates. Using the model developed, finite element analysis of three open-hole tension laminates, each exhibiting one of the brittle, pull-out, and delamination failure modes, is conducted. Results from the FEA of laminate exhibiting pull-out failure are compared to results of open-hole tension experiments conducted in scope of the SANTEZ project called “Design Methodology for Thick Composite Laminates. Results of the FEA of laminates exhibiting brittle and delamination damage are compared to experimental data from the literature [12,13].

Built-in features of the FEA software are utilized for the finite element analyses. Hashin’s failure criterion is used along with gradual linear damage evolution for intralaminar damage characterization. Gradual linear degradation is modeled ensuring that strain at damaged material point from damage initiation to total failure is 10% of the strain at damage initiation. Cohesive Zone Method (CZM) is utilized to model interlaminar damage. Bilinear traction-separation law that takes both damage detection and damage evolution is implemented into cohesive elements. Both power law and BK criterion are utilized to establish dependence of total fracture energy on mode-mixture.

8-noded 3-D continuum shell and cohesive elements are utilized for the plies and interfaces, respectively. Cohesive elements are placed at interfaces where neighboring plies have fibers with different orientations. Same-angle plies are blocked together to decrease the analysis time. Only in laminate exhibiting brittle

failure are some of the cohesive layers removed from the model in order to improve convergence. For this laminate, cohesive layers are placed at interfaces with highest possibility of delamination. Mismatch of Poisson's ratio and coefficient of mutual influence is the highest at these interfaces.

Mesh size and interface strengths are chosen in accordance with each other in order to have enough number of cohesive elements in the cohesive zone to accurately simulate delamination.

Lastly, analyses results are compared with the experimental results. Trend of load-displacement curve, ultimate load attained in the tension test, damage pattern after failure, and damage progression are utilized as criteria for comparison between experimental and numerical results. Effect of damage evolution trend, in-situ strengths, and delamination on damage is discussed.

7.2. Discussion

Results obtained by the proposed FEM correlate well with the experimental data. The model is able to simulate brittle, pull-out, and delamination failures observed in different laminates. The following discussions arise from the study:

- Damage progression in S2 glass/epoxy laminate cannot be tracked experimentally in detail due to insufficiency of experimental facilities. However, pointing light on the translucent laminate made of fiberglass/epoxy and observation of the laminate after failure provides some insight into damage evolution.
- Explicit analysis handles non-linear material behavior observed in composite laminates' damage progression effectively as long as dynamic effects are kept at low levels by applying the displacement in sufficiently long time intervals.
- Longitudinal failure energy for S2 glass/epoxy, which is obtained from the literature, may not represent the real behavior of the material system as the value found in the literature was for fiberglass/epoxy, not specific to S2 glass/epoxy.

- Ultimate load predictions increase with utilization of in-situ strengths in general. When gradual damage evolution is utilized, the use of in-situ strengths for carbon/epoxy laminate made the difference between ultimate loads obtained from the experiments and analyses larger. On the contrary, utilization of in-situ strengths yields ultimate load values very close to experimental value for the laminate made of fiberglass/epoxy.
- Formulae used to obtain in-situ strengths do not take the angle of neighboring plies into account, which may cause wrong in-situ strength predictions and affect the damage progression in the laminate. To exemplify, since in-situ strength of the outer 45° ply is different than that of inner plies, outer 45° plies fail far earlier than other off-axis plies in the laminate exhibiting pull-out failure. On the other hand, inner and outer plies are observed to fail simultaneously when in-situ strengths are not utilized. Thus, a wrong in-situ strength value for the outer ply would change the damage progression pattern.
- Experimentally determined in-situ strengths can be utilized to have more dependable in-situ strength values.
- Brittle, pull-out, and delamination failure patterns observed in three different laminates are successfully predicted. However, in the laminate exhibiting delamination, load increase due to undamaged 0° ligaments could not be simulated due to extensive mesh distortion. This problem can be overcome by utilizing full-integration elements that do not have hourglass modes causing mesh distortion.
- Load-displacement curves with and without cohesive layers for the laminates exhibiting pull-out and delamination failure are observed to be coincident until extensive delamination occurs. For the laminate exhibiting brittle failure, the curves are mostly coincident since very little delamination is present. This proves that cohesive layers do not affect the stiffness of the laminate in the loading direction.
- Neglecting delamination in finite element models yields damage patterns inconsistent with experimental observations. Removing cohesive layers from the FEM of the laminate exhibiting delamination causes pull-out

failure to be observed. Moreover, laminate exhibiting pull-out failure shows brittle failure when delamination is neglected. Damage pattern of brittle laminate does not change when cohesive layers are removed since delamination is not a prevalent failure mode in the brittle laminate. Therefore, it is essential to consider delamination in FEA of open-hole composite laminates.

- Change in failure patterns by neglecting delamination is reflected on load-displacement curves of the laminates. Naturally, FEM without cohesive layers could not predict the load drops due to delamination in the laminate exhibiting delamination failure. Ultimate load obtained by the FEA increased by around 14% for the laminate exhibiting pull-out failure when delamination is ignored. Change in ultimate load predictions for the brittle laminate was negligible since energy dissipated by delamination is quite low.
- Instantaneous degradation causes only one total load drop in the FEA of the laminate exhibiting delamination failure, which contradicts the experimental results. Gradual degradation, however, allows accurate damage predictions due to delamination although it results in overprediction of ultimate loads. In fact, the finite element analyses tend to overpredict ultimate loads for the other laminate made of carbon/epoxy as well when gradual degradation is utilized.
- Shear nonlinearity is not considered in the study. The slope difference between the load-displacement graphs obtained by experiments and analyses might be due to assuming linear shear stress-shear strain behavior.
- Although energy-based degradation alleviates mesh dependence, it does not completely eliminate the problem [44]. Therefore, the results may include slight dependence on mesh density.

7.3. Future Work

In this study, built-in features of the FEA software are utilized. The software utilizes Hashin's failure criterion for intralaminar damage initiation. Although the

model developed yields satisfactory results for the damage simulation in open-hole tension composite laminates, it is observed in Chapter 2 that it is not a global failure criterion that can simulate damage progression accurately for all kinds of loadings and laminates. For instance, open-hole compression laminates are subjected to combined shear and compression loads, which cannot be accurately predicted by Hashin's criterion. Therefore, in order to have a finite element model that is applicable to various types of composite laminates with holes, a more global failure criterion, such as Larc04, can be implemented in a VUMAT subroutine. VUMAT subroutine can also be used for implementation of non-linear shear behavior, which would improve the accuracy of the damage prediction.





REFERENCES

- [1] D. Kumar and S. B. Singh, "Effects of Boundary Conditions on Postbuckling Strengths of Composite Laminate with Various Shaped Cutouts under In-Plane Shear," *Open J. Compos. Mater.*, vol. 3, no. April, pp. 38–50, 2013.
- [2] M. K. A. M. Ariffin, M. I. M. Ali, S. M. Sapuan, and N. Ismail, "An optimise drilling process for an aircraft composite structure using design of experiments," *October*, vol. 4, no. October, pp. 1109–1116, 2009.
- [3] "Open-hole compression testing: CompositesWorld." [Online]. Available: <http://www.compositesworld.com/articles/open-hole-compression-testing>. [Accessed: 19-Jun-2015].
- [4] "Standard Test Method for Open-Hole Tensile Strength of Polymer Matrix Composite Laminates," *ASTM Stand. D5766/D5766M – 11*, 2013.
- [5] "Standard Test Method for Open-Hole Compressive Strength of Polymer Matrix Composite Laminates," *ASTM Stand. D6484/D6484M – 14*, 2014.
- [6] "Standard Practice for Filled-Hole Tension and Compression Testing of Polymer Matrix Composite Laminates 1," *ASTM Stand. D6742/D6742M – 12*, 2011.
- [7] "ASTM SN Composites Tech News." [Online]. Available: http://www.astm.org/SNEWS/MAY_2002/comp_may02.html. [Accessed: 15-Dec-2015].
- [8] J. Lee and C. Soutis, "Measuring the notched compressive strength of composite laminates: Specimen size effects," *Compos. Sci. Technol.*, vol. 68, no. 12, pp. 2359–2366, 2008.
- [9] "Virtual testing of composites: Beyond make & break : CompositesWorld." [Online]. Available: <http://www.compositesworld.com/articles/virtual-testing-of-composites-beyond-make-break>. [Accessed: 15-Dec-2015].
- [10] D. Albiol, "Buckling analyses of composite laminated panels with delamination," 2010.
- [11] P. K. Mallick, "Mechanics," in *Fiber-Reinforced Composites: Materials, Manufacturing, and Design*, 3rd ed., 2007.
- [12] S. R. Hallett, B. G. Green, W. G. Jiang, and M. R. Wisnom, "An experimental and numerical investigation into the damage mechanisms in

- notched composites,” *Compos. Part A Appl. Sci. Manuf.*, vol. 40, no. 5, pp. 613–624, 2009.
- [13] B. G. Green, M. R. Wisnom, and S. R. Hallett, “An experimental investigation into the tensile strength scaling of notched composites,” *Compos. Part A Appl. Sci. Manuf.*, vol. 38, no. 3, pp. 867–878, 2007.
- [14] R. M. O’Higgins, M. a. McCarthy, and C. T. McCarthy, “Comparison of open hole tension characteristics of high strength glass and carbon fibre-reinforced composite materials,” *Compos. Sci. Technol.*, vol. 68, no. 13, pp. 2770–2778, 2008.
- [15] A. C. Hansen, D. J. Kenik, and E. E. Nelson, “Multicontinuum failure analysis of composites,” pp. 1–10, 2009.
- [16] R. Cuntze, “The World-Wide-Failure-Exercises -I and - II for UD-materials - valuable attempts to validate failure theories on basis of more or less applicable test data sets -,” 2014.
- [17] A. S. Kaddour, M. J. Hinton, P. A. Smith, and S. Li, “The background to the third world-wide failure exercise,” *J. Compos. Mater.*, vol. 47, no. 20–21, pp. 2417–2426, 2013.
- [18] A. Turon, C. G. Dávila, P. P. Camanho, and J. Costa, “An engineering solution for mesh size effects in the simulation of delamination using cohesive zone models,” *Eng. Fract. Mech.*, vol. 74, no. 10, pp. 1665–1682, 2007.
- [19] C. S. Shirley Kalamis Garcia-Castillo, Sonia Sanchez-Saez and and E. B. Carlos Navarro, “Perforation of Composite Laminate Subjected to Dynamic Loads,” vol. 192, 2013.
- [20] P. P. Camanho, P. Maimí, and C. G. Dávila, “Prediction of size effects in notched laminates using continuum damage mechanics,” *Compos. Sci. Technol.*, vol. 67, no. 13, pp. 2715–2727, 2007.
- [21] M. Patricio and R. M. M. Mattheij, “Crack propagation analysis,” *CASA Rep.*, 2007.
- [22] E. J. Barbero, *Finite Element Analysis of Composite Materials Using Abaqus*, 1st ed. Taylor & Francis Group, 2013.
- [23] S. R. Hallett, W. G. Jiang, B. Khan, and M. R. Wisnom, “Modelling the interaction between matrix cracks and delamination damage in scaled quasi-isotropic specimens,” *Compos. Sci. Technol.*, vol. 68, no. 1, pp. 80–89, 2008.

- [24] R. Krueger, "Virtual crack closure technique: History, approach, and applications," vol. 57, no. 2, pp. 109–143, 2004.
- [25] Q. Yang and B. Cox, "Cohesive models for damage evolution in laminated composites," *Int. J. Fract.*, vol. 133, no. 2, pp. 107–137, 2005.
- [26] B. Göztlüklü, "Delamination Analysis by Using Cohesive Interface Elements in Laminated Composite," 2009.
- [27] P. W. Harper and S. R. Hallett, "Cohesive zone length in numerical simulations of composite delamination," *Eng. Fract. Mech.*, vol. 75, no. 16, pp. 4774–4792, 2008.
- [28] P. D. Soden, A. S. Kaddour, and M. J. Hinton, "Recommendations for designers and researchers resulting from the world-wide failure exercise," *Compos. Sci. Technol.*, vol. 64, no. 3–4, pp. 589–604, 2004.
- [29] M. R. Garnich and V. M. K. Akula, "Review of Degradation Models for Progressive Failure Analysis of Fiber Reinforced Polymer Composites," *Appl. Mech. Rev.*, vol. 62, no. 1, p. 010801, 2009.
- [30] J. Hol and V. Antonelli, "Progressive Damage Modelling of FML's. Implementation in a UMAT subroutine," *Aerospace*, no. Figure 1, pp. 1–11.
- [31] Z. Hashin and A. Rotem, "A Fatigue Failure Criterion for Fiber Reinforced Materials," 1973.
- [32] Z. Hashin, "Fatigue Failure Criteria for Unidirectional Fiber Composites," *J. Appl. Mech.*, vol. 48, no. 4, p. 846, 1981.
- [33] C. G. Davila, N. Jaunky, and S. Goswami, "Failure Criteria for FRP Laminates in Plane Stress," vol. 39, no. 4, 2003.
- [34] C. T. Sun, B. J. Quinn, J. Tao, D. W. Oplinger, and W. J. Hughes, "Comparative Evaluation of Failure Analysis Methods for Composite Laminates," no. May, 1996.
- [35] A. Puck and H. Schürmann, "Failure Analysis of FRP Laminates by Means of Physically Based Phenomenological Models.pdf," pp. 264–297, 2004.
- [36] M. J. Hinton, A. S. Kaddour, and P. D. Soden, "The world-wide failure exercise: Its origin, concept and content," pp. 2–28, 2004.
- [37] P. D. Soden, M. J. Hinton, and a. S. Kaddour, "Lamina properties, lay-up configurations and loading conditions for a range of fibre-reinforced

- composite laminates,” *Compos. Sci. Technol.*, vol. 58, no. 7, pp. 1011–1022, 1998.
- [38] A. S. Kaddour and M. J. Hinton, *Benchmarking of triaxial failure criteria for composite laminates: Comparison between models of “Part (A)” of “WWFE-II,”* vol. 46, no. 19–20. 2012.
- [39] A. Kaddour, M. Hinton, P. Smith, and S. Li, “A comparison between the predictive capability of matrix cracking, damage and failure criteria for fibre reinforced composite laminates: Part A of the third world-wide failure exercise,” *J. Compos. Mater.*, vol. 47, no. 20–21, pp. 2749–2779, 2013.
- [40] S. T. Pinho, C. G. Davilla, P. P. Camanho, L. Iannucci, and P. Robinson, “Failure Models and Criteria for FRP Under In-Plane or Three-Dimensional Stress States Including Shear Non-Linearity,” no. February, 2005.
- [41] M. R. Wisnom, S. R. Hallett, and C. Soutis, “Scaling Effects in Notched Composites,” *J. Compos. Mater.*, vol. 44, no. 2, pp. 195–210, 2010.
- [42] A. Satyanarayana and A. Przekop, “Predicting Failure Progression and Failure Loads in Composite Open-Hole Tension Coupons,” no. May, 2010.
- [43] P. P. Camanho, P. Maimí, and C. G. Dávila, “Prediction of size effects in notched laminates using continuum damage mechanics,” *Compos. Sci. Technol.*, vol. 67, no. 13, pp. 2715–2727, 2007.
- [44] I. Lapczyk and J. A. Hurtado, “Progressive damage modeling in fiber-reinforced materials,” *Compos. Part A Appl. Sci. Manuf.*, vol. 38, no. 11, pp. 2333–2341, 2007.
- [45] S. T. Pinho, P. Robinson, and L. Iannucci, “Fracture toughness of the tensile and compressive fibre failure modes in laminated composites,” *Compos. Sci. Technol.*, vol. 66, no. 13, pp. 2069–2079, 2006.
- [46] K. Song, Y. Li, and C. A. Rose, “Continuum Damage Mechanics Models for the Analysis of Progressive Failure in Open-Hole Tension Laminates,” pp. 1–18, 2011.
- [47] Y. Nikishkov, A. Makeev, and G. Seon, “Simulation of Damage in Composites Based on Solid Finite Elements,” *J. Am. Helicopter Soc.*, vol. 55, no. 4, p. 042009, 2010.
- [48] M. Ridha, C. H. Wang, B. Y. Chen, and T. E. Tay, “Modelling complex progressive failure in notched composite laminates with varying sizes and stacking sequences,” *Compos. Part A Appl. Sci. Manuf.*, vol. 58, pp. 16–23, 2014.

- [49] F. Dharmawan, C. H. Wang, and A. Rider, "Computational analysis of the Influence Material Orthotropy on the Residual Strength of Laminated Composites," *Proc. 6th Australas. Congr. Appl. Mech.*, p. 1422, 2010.
- [50] Z. C. Su, T. E. Tay, M. Ridha, and B. Y. Chen, "Progressive damage modeling of open-hole composite laminates under compression," *Compos. Struct.*, vol. 122, pp. 507–517, 2015.
- [51] "Abaqus/CAE V6.14 User's Manual." .
- [52] T. L. Anderson, *Fracture Mechanics Fundamentals and Applications*, 3rd ed. Taylor & Francis, 2005.
- [53] C. T. Sun and Z. H. Jin, "Modeling of composite fracture using cohesive zone and bridging models," *Compos. Sci. Technol.*, vol. 66, no. 10, pp. 1297–1302, 2006.
- [54] M. F. S. F. de Moura, R. D. S. G. Campilho, a. M. Amaro, and P. N. B. Reis, "Interlaminar and intralaminar fracture characterization of composites under mode I loading," *Compos. Struct.*, vol. 92, no. 1, pp. 144–149, 2010.
- [55] M. L. Benzeggagh and M. Kenane, "Measurement of mixed-mode delamination fracture toughness of unidirectional glass/epoxy composites with mixed-mode bending apparatus," *Compos. Sci. Technol.*, vol. 56, no. 4, pp. 439–449, 1996.
- [56] "Standard Test Method for Mode I Interlaminar Fracture Toughness of Unidirectional Fiber-Reinforced Polymer Matrix Composites," *ASTM Stand. D5528 – 13*, 2014.
- [57] "Standard Test Method for Determination of the Mode II Interlaminar Fracture Toughness of Unidirectional Fiber-Reinforced Polymer Matrix Composites," *ASTM Stand. D7905/D7905M – 14*, 2015.
- [58] "Standard Test Method for Mixed Mode I-Mode II Interlaminar Fracture Toughness of Unidirectional Fiber Reinforced Polymer Matrix Composites," *ASTM Stand. D6671/D6671M – 13*, 2013.
- [59] C. G. Dávila and P. P. Camanho, "Skin / Stiffener Debonding Using Decohesion Elements," *Test*, no. April, pp. 1–9, 2003.
- [60] A. B. de Morais and A. B. Pereira, "Mixed mode I + II interlaminar fracture of glass/epoxy multidirectional laminates - Part 1: Analysis," *Compos. Sci. Technol.*, vol. 66, no. 13, pp. 1889–1895, 2006.
- [61] B. G. Green, M. R. Wisnom, and S. R. Hallett, "An experimental investigation into the tensile strength scaling of notched composites," *Compos. Part A Appl. Sci. Manuf.*, vol. 38, no. 3, pp. 867–878, 2007.

- [62] R. M. Jones, *Mechanics of Composite Materials*, 2nd ed. Taylor & Francis, 1999.
- [63] R. G. Cuntze and A. Freund, “The predictive capability of failure mode concept-based strength criteria for multidirectional laminates,” *Compos. Sci. Technol.*, vol. 64, no. 3–4, pp. 343–377, 2004.
- [64] M. J. Swindeman, E. V. Iarve, R. A. Brockman, D. H. Mollenhauer, and S. R. Hallett, “Strength Prediction in Open Hole Composite Laminates by Using Discrete Damage Modeling,” *AIAA J.*, vol. 51, no. 4, pp. 936–945, 2013.
- [65] P. P. Camanho, C. G. Dávila, S. T. Pinho, L. Iannucci, and P. Robinson, “Prediction of in situ strengths and matrix cracking in composites under transverse tension and in-plane shear,” *Compos. Part A Appl. Sci. Manuf.*, vol. 37, no. 2, pp. 165–176, 2006.
- [66] A. Turon, C. G. Davila, P. P. Camanho, and J. Costa, “An Engineering Solution for Using Coarse Meshes in the Simulation of Delamination with Cohesive Zone Models,” no. March, 2005.
- [67] “Analysis of crack formation and crack growth in concrete by means of fracture mechanics and finite elements Hillerborg 1976.pdf” .
- [68] P. P. Camanho and C. G. Davila, “Mixed-Mode Decohesion Finite Elements for the Simulation of Delamination in Composite Materials,” no. June, 2002.
- [69] A. Turon, P. P. Camanho, J. Costa, and J. Renart, “Accurate simulation of delamination growth under mixed-mode loading using cohesive elements: Definition of interlaminar strengths and elastic stiffness,” *Compos. Struct.*, vol. 92, no. 8, pp. 1857–1864, 2010.
- [70] Y. Mohammed, M. K. Hassan, A. E. H, and a M. Hashem, “Fracture Properties of Glass Fiber Composite Laminates and Size Effect,” vol. 1, no. 1, pp. 13–26, 2013.

APPENDIX: EFFECT OF MESH SIZE ON THE ULTIMATE LOAD

Finite element analyses exhibit mesh dependence when the material incorporates strain-softening behavior. The total energy dissipated by the failed elements may change as the mesh is refined, which results in different damage patterns and ultimate loads with the use of different mesh densities. The software utilized in the study introduces a “characteristic length” into damage evolution formulation by expressing the constitutive law as a stress-displacement relationship in order to alleviate the mesh dependence by considering the finite element discretization. According to this approach, the stress-displacement relationship is the same regardless of the mesh size; however, the failure strain changes with the mesh size. Area under the equivalent stress - equivalent displacement graph is equal to failure energy per unit cross sectional area of the corresponding failure mode and is determined by the experiments. What changes in this formulation is the failure strain, which is adjusted to the mesh size. As the mesh size increases, the failure strain decreases to ensure constant failure energy. The above methodology is applied in the study for the gradual failure based on failure energy. In the instantaneous failure, however, failure energy per unit cross section area of the specimen changes with the mesh size. In this case, failure strain is constant regardless of the mesh size, but displacement at failure changes with the mesh refinement as shown in Figure A-1.

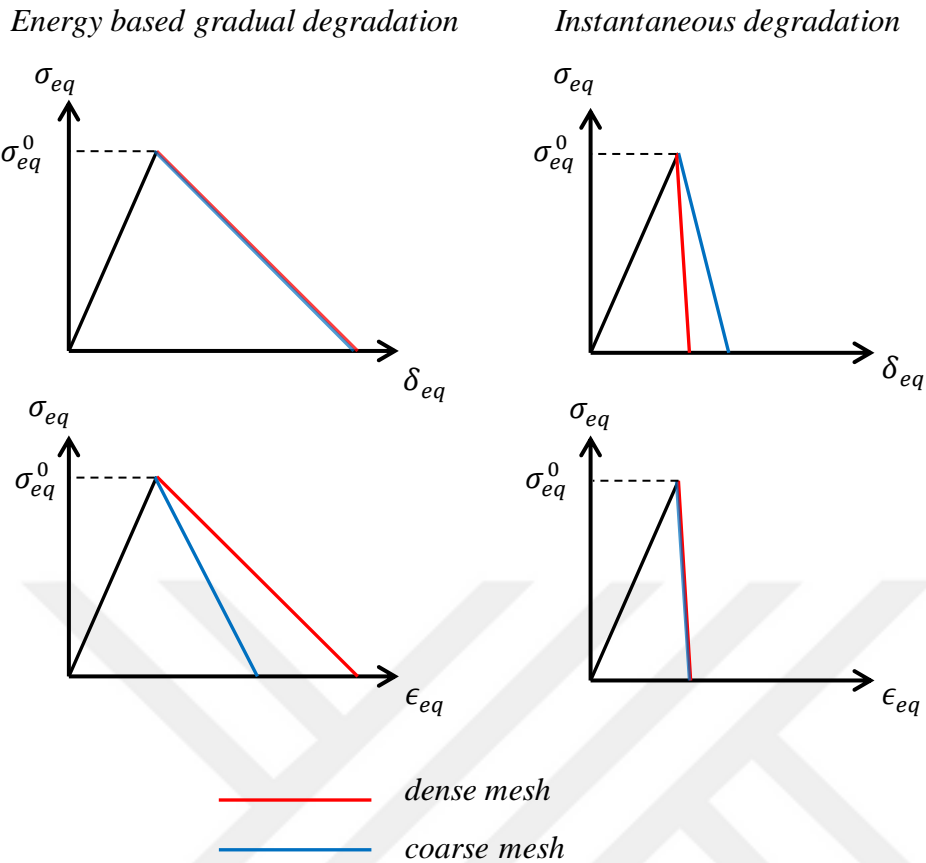


Figure A-1 Representative equivalent stress vs. equivalent displacement and equivalent stress vs. equivalent strain graphs for energy based and instantaneous degradation

In this chapter, the laminate exhibiting brittle failure is examined to investigate the effect of mesh density on the damage and the ultimate load. Three different element sizes are utilized where the elements always had an in-plane shape of square. The elements have side lengths of 0.8 mm , 1.15 mm , and 1.5 mm . Element deletion is implemented such that the elements whose damage variable reach the value 0.99 are removed from the mesh.

The analyses show that regardless of the element size and degradation trend, the fiber damage is localized in a strip of one element thickness as shown in Figure A-2. This trend causes the volume of the damaged region to decrease the mesh density increases. Since the failure energy per unit cross sectional area decreases as the element size gets smaller in the instantaneous degradation, with the cross

sectional area of the fracture plane constant, total energy dissipated by the failed elements decrease as well when the element size gets smaller. This results in lower ultimate loads with decreasing element sizes as shown in Fig A-3.

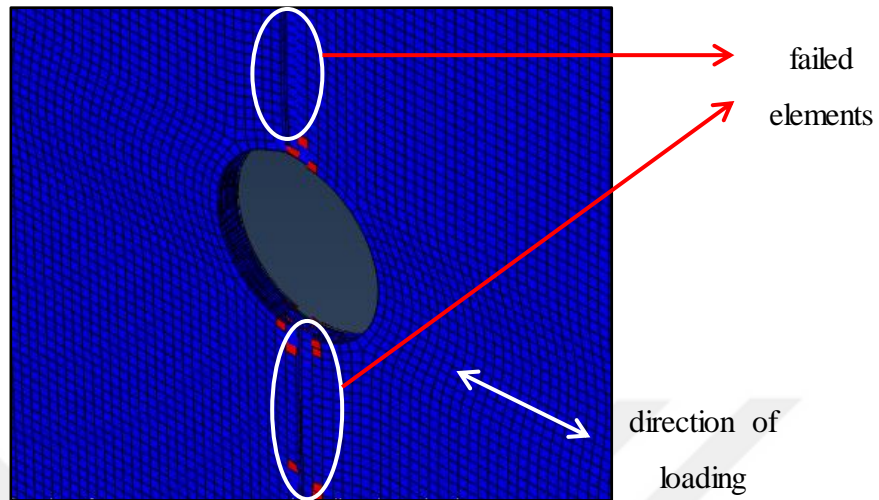


Figure A-2 Strip of failed elements in 0° layer in the model with element side length of 0.8 mm

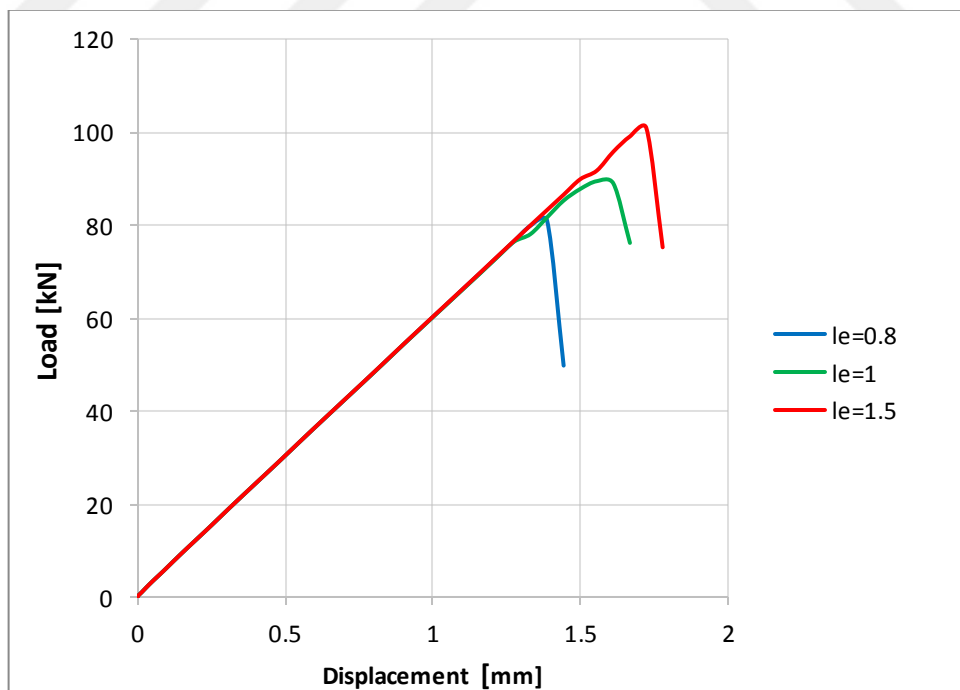


Figure A-3 Load-displacement curves obtained with instantaneous degradation for different mesh sizes

Contrary to instantaneous degradation, energy based gradual degradation causes ultimate loads to decrease as the element size gets larger as shown in Fig A-4. The energy dissipated by the failed strip does not change as the element size changes in the energy based gradual degradation; however, decrease in the size of the high stressed regions neighboring the fracture plane might cause the drop in the ultimate loads as the element size increases. It should be noted, however, that energy based gradual degradation alleviates the mesh dependence. While the predicted ultimate load decreases by 9.2% with the energy based gradual degradation, it increases by around 25% with instantaneous degradation as the element size increases from 0.8 mm to 1.5 mm.

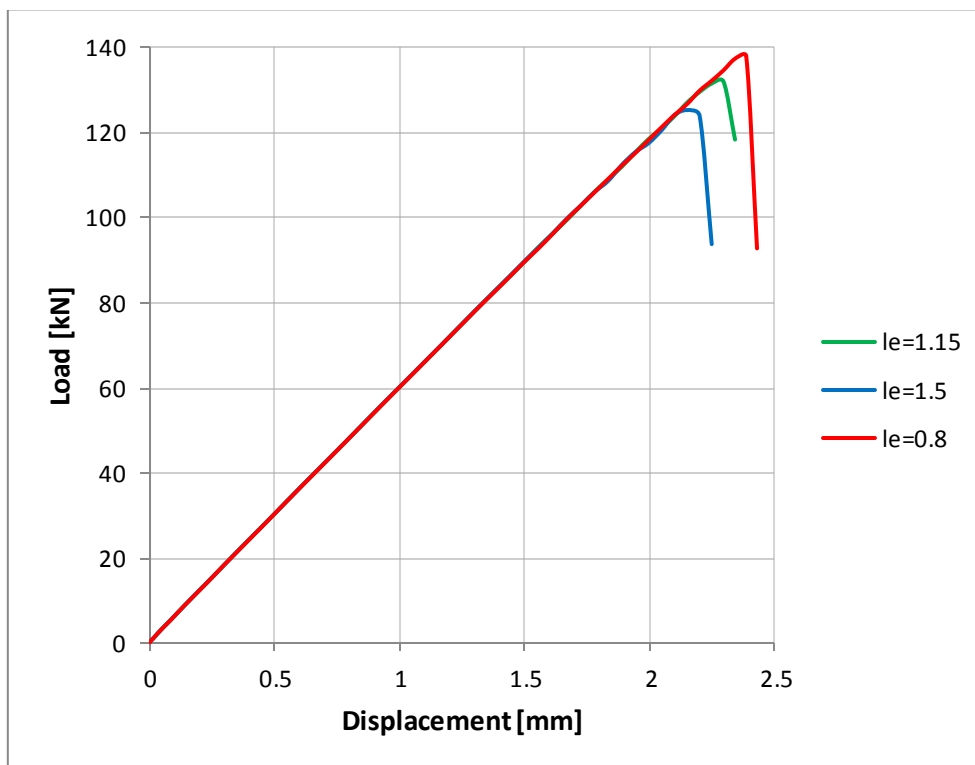


Figure A-4 Load-displacement curves obtained with gradual degradation for different mesh sizes

The mesh size does not affect the way damage develops. Damage progression is similar for different mesh sizes.